8-2013

Green Manufacturing of Nanoparticles for Biomedical Applications

Sijia Yi
syi2@utk.edu

To the Graduate Council:

I am submitting herewith a dissertation written by Sijia Yi entitled "Green Manufacturing of Nanoparticles for Biomedical Applications." I have examined the final electronic copy of this dissertation for form and content and recommend that it be accepted in partial fulfillment of the requirements for the degree of Doctor of Philosophy, with a major in Biomedical Engineering.

Mingjun Zhang, Major Professor

We have read this dissertation and recommend its acceptance:

William R. Hamel, Qiang He, Zhili Zhang

Accepted for the Council:
Dixie L. Thompson

Vice Provost and Dean of the Graduate School

(Original signatures are on file with official student records.)

Green Manufacturing of Nanoparticles for Biomedical Applications

A Dissertation Presented for the
Doctor of Philosophy
Degree
The University of Tennessee, Knoxville

Sijia Yi
August 2013

DEDICATION

To my dearest parents and Yongqiang Gou,

for their constant support and infinite love to my pursuit of dreams and happiness.

ACKNOWLEDGEMENTS

Tremendous thanks go to the many people who helped and encouraged me in the past three years. First, I would like to express heartfelt gratitude to my supervisor, Dr. Mingjun Zhang, who offered me the valuable opportunity to become a part of his team at UT. He provided me with research independence and support in my PhD studies. I deeply appreciate his advice, help and encouragement.

I would like to thank the professors on my doctoral committee, Dr. William R. Hamel, Dr. Qiang He, and Dr. Zhili Zhang for their thorough and scientific advice concerning my research. Their comments and suggestions have been very valuable in the completion of this thesis.

I would like to express my deepest appreciation to all lab members at UT for their constant help and support during my PhD studies. A special expression of gratitude goes to scientists Dr. Yongzhong Wang, Dr. Scott C. Lenaghan and Dr. Lijin Xia. I am grateful for their guidance and support, and the lengthy discussions which I believe I learned the most from. I thank Leming Sun, who always helped resolve AFM and SEM related issues.

I am grateful for the assistance I received from people outside my research group. Jun Yan taught me the techniques of HPLC for my project, Xinyuan Chong and DJ Simmons helped me with the SERS issues, and Zhiqian Sun offered critical support and help on XRD technology. I thank Dr. John Dunlap for training on SEM and TEM. I am also grateful for the kind assistance from Dr. Wei He and her group.

Additionally, thanks to Dr. Stephen A. Kania, Dr. Becky Penrose Wilkes, Dianne Trent and Mary Lozano who provided help, support and encouragement.

To all my friends, I thank you always for your generosity and friendship.

Last, I wish to thank my parents and Yongqiang Gou for their endless love, support and encouragement. I will be grateful forever for your love.

ABSTRACT

The vast majority of nanomaterials are chemically synthesized, a costly process, that is environmentally risky, and the produced nanoparticles are potentially toxic to patients. Nature-based nanomaterials, however, are proving to be much more biocompatible with lower environmental toxicity. Even though a variety of natural nanomaterials have been designed, fabrication technologies for the desired natural nanoparticles with reproducible quality, high productivity and low cost remain a challenge. My objective has been to establish strategies for the isolation, purification and characterization of nanoparticles using a production system based on green tea and fungus (*Arthrobotrys oligospora*) and also to develop new approaches for sustainable “green manufacture” of gold nanoparticles for biomedical applications. First, an infusion-dialysis procedure to isolate of the tea nanoparticles (TNPs) from a green tea infusion was developed and validated. The TNPs are spherical with a diameter of 100-300 nm, and have a zeta potential of -26.52 mV at pH 7.0. The TNPs enhance secretion of the cytokines and the chemokines from mouse macrophages, suggesting a potential immunostimulatory effect. As a natural nanocarrier, the TNPs are able to form complexes with doxorubicin (DOX). The DOX-loaded TNPs increase cellular DOX uptake, leading to higher cytotoxicity in cancer cells. Second, a new isolation procedure was established to purify the fungal nanoparticles (FNPs) from *A. oligospora*, giving two purified FNP fractions. Both purified FNPs had a reduced diameter of 100-200 nm, with glycosaminoglycan as the main

constituent. The purified FNPs cause mild cytotoxicity by inducing apoptosis and regulating the cell cycle in multiple tumor cell lines and have an immunostimulatory effect. Additionally, the FNPs have an immunochemotherapeutic effect upon complexing with DOX against tumor cells. Third, a sustainable system for green manufacturing of gold nanoparticles was developed by using actively growing English ivy. The efficient uptake of the synthesized gold nanoparticles in mammalian cells provides the potential for biomedical applications. Finally, a simple one-step approach using dopamine, a monoamine neurotransmitter appearing naturally in the human brain, to synthesize highly branched gold nanoflowers (AuNFs) was developed. These AuNFs are highly biocompatible and provide high surface enhanced Roman scattering (SERS) performance.

TABLE OF CONTENTS

LIST OF TABLES

LIST OF FIGURES

CHAPTER I
INTRODUCTION

Personalized medication and treatment are the optimal goals for disease treatment. This is particularly true for cancer therapy, due to the heterogeneity of cancer and its diverse causes. Individualized treatment could be achieved by developing an effective theranostic, defined as material that combines the modalities of the therapeutic medication and diagnostic imaging capability. [1] One huge advantage of theranostic is the avoidance of an adverse reaction between the diagnostics and the selectivity of the drug utilized in the treatment. Nanomaterials, which combine the imaging agents and the therapeutic drugs into molecules have the potential to be developed as the next generation of theranostics.

The next generation drug delivery system: Nanoparticles

Conventional therapeutic agents are distributed nonspecifically in the body where they affect both cancerous and normal cells. Thus the limiting dosage may not be optimal for treatment due to the excessive toxicities. Nanoparticles, loaded with therapeutic drugs and modified for the tissue, cell and organelle targeting motifs, are able to target cancer cells using the unique pathophysiology of tumors, including cancerous cellular markers, organelle localization signals, and the enhanced permeability and retention effect of the tumor microenvironment. Additionally, nanoparticle carriers are able to improve the delivery of poorly

water-soluble drugs and enhance the circulation time of the drug in vivo to further reduce the dosage needed for treatment.

Targeting: necessity or luxury?

Current clinically approved nano-products are relative simple and lack of targeting motif. In fact, nearly 30 years after the first targeted l targeted liposomes is constructed. [2] Unfortunately, thus far this technology had a limited impact on human health. The reasons are complex and comprehensive. Targeted delivery of a therapeutic drug is a complicated procedure, involving the stability of the delivery particles, the mode of action of the drug and the efficiency of the site-specific delivery. In some cases, it is believed that targeting can cause anchoring of the delivery systems, reducing the efficiency of diffusion and tissue penetration. [3] However, dramatic molecular biology advances over the last 30 years have expanded our understanding of the mechanisms involved, providing the means to develop new approaches to the design of drug delivery systems. The identification of specific molecular markers in different types of cancer cells provides new therapeutic targets, making it increasingly feasible to engineer a muti-functional and specific drug delivery system for therapeutic applications. This system is already being actively employed. Recently the phase I trial has been completed for CALAA-01[4], a transferrin-targeted particle delivering siRNA to reduce the expression of the M2 subunit of the ribonucleotide reductase (R2) for solid tumor therapy.

Polymer-based Nanoparticles as drug delivery systems

Several types of nanoparticles can be utilized in the design of a delivery system, including polymer-based drug carriers, polymeric nanoparticles, polymeric micelles, dendrimers, liposomes, viral nanoparticles, carbon nanotubes. Polymer-based nanoparticles are derived from polymers such as albumin, chitosan, and heparin. They can be naturally used as material to deliver oligonucleotides, DNA, proteins and therapeutic drugs, including paclitaxel and doxorubicin. Doxorubicin, an anticancer drug, inhibits DNA topoisomerase II, an enzyme that is in both mitochondria and nucleus. DOX has been used in several studies as a therapeutic drug delivered into cancer cells. DOX has been successfully encapsulated into human serum albumin nanoparticles to treat anoikis-resistant breast cancer cells. The DOX-conjugated nanoparticles have proven to be significantly more cytotoxic to the breast cancer cells than free DOX. The conjugated nanoparticles have been delivered into the cells much more efficiently than the free DOX by avoiding the drug efflux pump system. [5] DOX has also been delivered by folate-conjugated P(NIPAAm- co -DMAAm- co -UA)- g -cholesterol nanoparticles, which target the folate receptor of the cancerous cells enabling a more rapid entry into the nucleus. Based on this model, this study defines a mechanism for faster nuclear entry using folate as a cell specific targeting factor and undecenoic acid as a PH sensitive component which mediates a more efficient drug release and nucleus entry. [6]

The production of gold nanoparticles for biomedical applications

Gold nanoparticles are of great interest in fields as diverse as electronics, coatings, photonics, surface-enhanced Raman scattering (SERS) and biotechnology. This is due to their unique properties, including size- and shape-based optical and electronic characteristics, their high surface area to volume ratio and their ability to be easily modified with ligands containing functional groups such as thiols and amines. [7] Additionally, gold nanoparticles are able to traverse through the vasculature, be localized in targeted areas, and can be attached to single strands of DNA nondestructively. [8] The use of gold nanoparticles to date suggests that they may be potentially useful in many biomedical applications. Considering their broad potential, the production of gold nanoparticles on a large-scale and in a controlled manner depending on the size, shape and crystallization has drawn significant attention in recent years.

It is well known that the production of nanoparticles can be achieved by various methods. Although several chemical and physical strategies have been utilized to successfully produce pure and well-defined gold nanoparticles, these methods are toxic, expensive and/or potentially dangerous to the environment. A biologically synthesis of gold nanoparticles could be easily prove to be superior to the chemical and physical processes, due to the low cost, high efficacy, suitability for large-scale synthesis and low environmental impact. [9, 10] A variety of plants, fungus, and bacteria have been successfully used for rapid biological synthesis for gold nanoparticles. Plant extracts, such as lemongrass

(*Cymbopogon flexuosus*) [11], Aloe vera [12], geranium (*Pelargonium graveolens*) [13], tamarind (*Tamarindus indica*) [14], and English ivy [15] have been shown to have the ability to reduce Au(III) ions to Au(0). Microorganisms like bacteria, yeast and a number of species of fungus have also been employed, such as *Fusarium oxysporum* [16], *Colletotrichum sp.*[13], *Rhodopseudomonas capsulate* [17], and *Trichothecium sp.* [18]. The use of different plants and systems resulting in gold nanoparticlces with various shapes and sizes has led to the discovery of the role of reductases and reducing agents involved in the synthesis. Nitrate reductase from a fungus (*Fusarium oxysporum*) has been demonstrated to utilize NADPH as a reducing agent. [9] A variety of proteins, polyphenols and carbohydrates are involved in the synthesis of gold nanoparticles with different sizes and shapes. [9] These constituents present in plants and microorganisms may be useful in the synthesis of individualized nanoparticles. The involvement of these constituents in the mechanism of the synthesis needs further experimental examination. [9]

Thesis Objectives

A great deal of research has led to the development of chemically synthesized nanomaterials; however, a variety of natural nanomaterials, including viruses [19], lipoproteins[20], diatoms nano-biosilica [21], ivy nanoparticles [22, 23], and fungal nanoparticles (*A. Oligospora*) [24], have recently drawn widespread attention. They have the advantages of being biocompatible, have low

environmental toxicity associated with production, and have promising medical applications. [22, 25, 26]

Tea, one of the most popular beverages in the world, has numerous therapeutic effects. It has been implicated as a players in lowering blood pressure [27], decreasing blood coagulation [28], treating HIV [29], repairing oxidative damage[30, 31], and cancer prevention and treatment. [32-35] Several studies have shown that the most active anticancer compounds in tea are polyphenols, such as (-)-epigallocatechin gallate (EGCG), (-)-epigallocatechin (EGC), and (+)-gallocatechin (GC). [36-38] These polyphenols exhibit anticancer effects by affecting various genes involved in the regulation of the cell cycle, apoptosis, invasion, metastasis, and angiogenesis. [39, 40] In addition to the polyphenols, natural polysaccharides from tea have also drawn researchers' attention due to their antitumor, immunostimulatory and antioxidant properties. [28, 41, 42] Interestingly, some naturally occurring nanoparticles with diameters of 200-300 nm in black tea were reported by Groning *et al* in 1995; [43] however, not enough nanoparticles were isolated from black tea for further component analysis and specific biomedical characterization. This thesis elucidates a novel efficient method for purifying the tea nanoparticles to utilize their potential therapeutic properties for cancer therapy.

Organic nanoparticles have shown promise in cancer treatment, due to their biocompatibility, biodegradation and multifunctional capacities. [44] Most reports

on natural organic nanoparticles are focusing on development in higher organisms, especially marine species and plants. Considering the rich biological diversity of the earth, natural organic nanoparticles may be produced in different forms and with different functions from unique origin. Investigation of nanoparticles in natural systems will not only help us to understand the roles of the nanoparticles in biological systems, but also provide us opportunities to develop these nanoparticles for specific biomedical applications. The discovery of new natural nanoparticles from *A. Oligospora* and the exploration of "scalable green manufacturing" nanoparticles for cancer therapy is a step in this process.

Gold nanoparticles have been utilized for many purposes. They have been proved to be especially effective for Surface Enhanced Raman Spectroscopy (SERS) [45], cancer diagnostics [46] and thermal therapy [47]. Several chemical and physical processes have been design in attempts to synthesize different sizes and shapes of gold nanoparticles. In order to reduce the use of toxic chemicals used in typical AuNP synthesis, active investigation for alternative synthesis methods are being employed using biological materials (proteins, polysaccharides, polyphenol, etc.) for green-synthesis of gold nanoparticles. While the use of plant extracts to synthesize AuNPs has been proposed, it has some serious drawbacks. Harvesting AuNPs from plant tissue introduces additional complexions due to the limited amount of AuNPs relative to the large plant biomass [48, 49], resulting in increased costs, and production delays. This

work offers a rapid and sustainable English ivy-based production system developed to synthesize gold nanoparticles for biomedical applications.

Gold nanoflowers are specialized gold nanoparticles with multiple highly branched tips, which give the overall appearance of a flower. The nanomorphology of the highly tipped and branched often leads to the formation of sharp peaks and valleys, which are potential “hot spots” for localized near-field enhancements. [45, 50, 51] The highly branched nanostructures can dramatically increase the ratio of total surface to volume. These factors lead to the enhancement of the Raman scattering on the highly branched gold nanostructures. [52, 53] Compared to smooth surfaces, highly branched surfaces (such as dendrites, multi-pods, and nanoflowers) have a greater potential for SERS based bioimaging and biosensing. While their potential usefulness has stimulated further research, the controllable synthesis of these unique nanostructures at a low cost remains a challenge. This thesis proposes a novel, one-step synthesis method to produce gold nanoflowers, using dopamine to insure a high SERS performance.

CHAPTER II
TEA NANOPARTICLES FOR IMMUNOSTIMULATION AND CHEMO-DRUG DELIVERY IN CANCER TREATMENT

Introduction

Much research has contributed to the development of chemically synthesized nanomaterials; however, a variety of natural nanomaterials, such as viruses [19], lipoproteins [20], diatoms nano-biosilica [21], ivy nanoparticles [22, 23], and fungal nanoparticles (*A. Oligospora*) [24], have recently drawn researchers' attention due to their promising biocompatibility, less environmental toxicity associated with their production, and their features desired in medicine. [22, 25, 26]

Tea is one of the most popular beverages in the world and has been linked to numerous therapeutic effects, including lowering blood pressure [27], decreasing blood coagulation [28], treating HIV [29], repairing oxidative damage[30, 31], and cancer prevention and treatment[32-35]. Several studies have shown that the most active anticancer compounds in tea are polyphenols, such as (-)-epigallocatechin gallate (EGCG), (-)-epigallocatechin (EGC), and (+)-gallocatechin (GC) [36-38]. These polyphenols exhibit anticancer effects by affecting various genes involved in the regulation of the cell cycle, apoptosis, invasion, metastasis, and angiogenesis. [39, 40] In addition to the polyphenols, natural polysaccharides from tea have also drawn researchers' attention due to their antitumor, immunostimulatory and antioxidant properties. [28, 41, 42] Interestingly, some natural nanoparticles with diameters of 200-300 nm in black tea were reported by Groning *et al* in 1995 [43]; however, they didn't isolate enough nanopartiles from black tea for further component analysis and specific biomedical applications. Considering the success of other natural-based

nanoparticles for cancer chemotherapy and immunotherapy [24], we hypothesized that tea is an ideal source of highly biocompatible nanomaterials for different biomedical applications, especially for cancer therapy. Due to the traditional role of tea as a cancer preventing beverage and good biocompatibility, we believe that the development of nanoparticles from tea as a biomaterial may open a new avenue for cancer therapy.

The goal of this study was to develop a fabrication method for isolation of natural nanoparticles from tea, and to explore their potential applications as a immunostimulatory agent and a nanocarrier for chemo-drug delivery in cancer therapy *in vitro*. For this purpose, an infusion-dialysis based procedure was developed to isolate spherical nanoparticles with diameters of 100-300 nm from green tea infusions (**Figure 1**). These TNPs were characterized by (atomic force microscopy) AFM, (scanning electron microscopy) SEM and (dynamic light scattering) DLS/ (electrophoretic light scattering) ELS. We have also conducted studies to quantitatively measure the concentration of protein, polysaccharide and other small molecules in the TNPs. The potential for the TNPs to be used as an immunostimulatory agent, and a natural drug nanocarrier for chemo-drug delivery to sensitive and resistant tumor cells was further evaluated through this study.

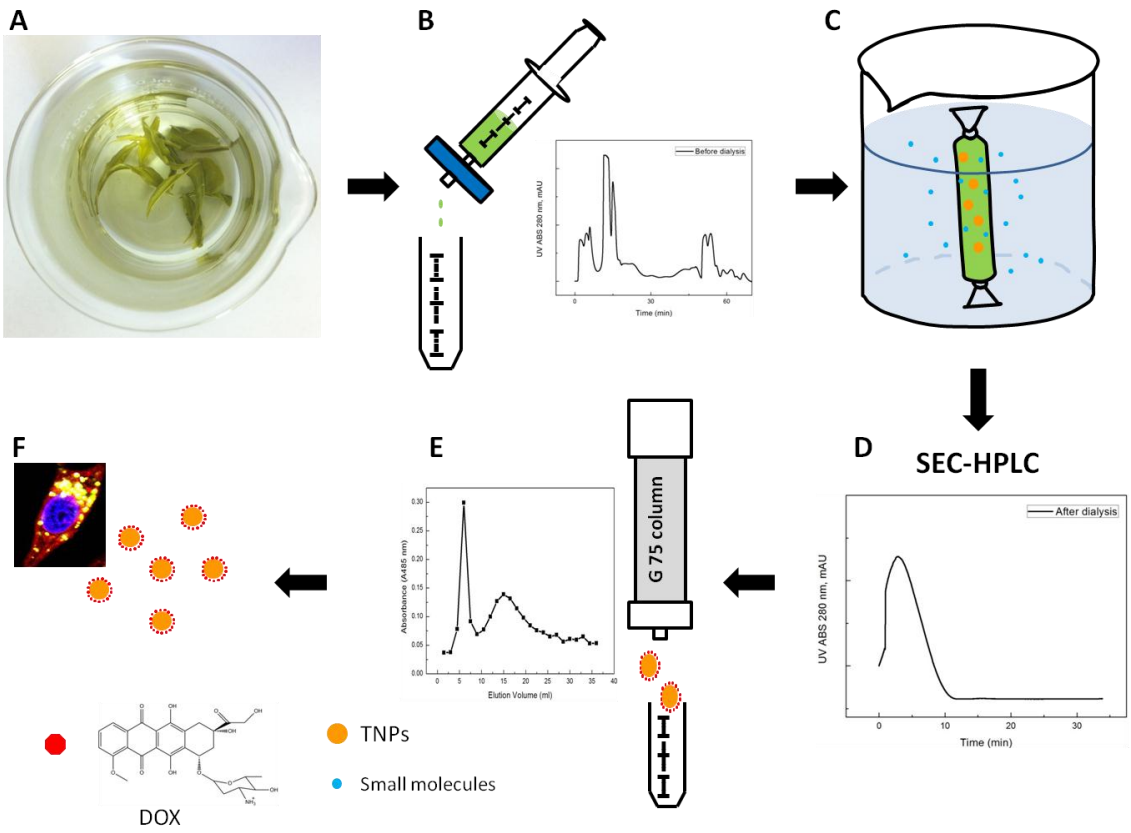

Figure 1 Schematic of the infusion-dialysis based procedure for isolating the TNPs from green tea leaves for drug delivery.

(A) Green tea infusion was prepared by hot DI water. (B) The syringe filter was used to remove big debris. (C) The dialysis tubing (MWCO=300KD) was used to remove small molecules in green tea infusion. (D) Isolation of the TNPs was determined by SEC-HPLC. (E) Sephadex G75 column was used to separate the DOX-loaded TNPs and free DOX. (F) Isolated DOX-loaded TNPs were used for drug delivery.

Materials and Methods

Materials

Laoshan® green tea was purchased from China. (-) Epigallocatechin gallate (EGCG), caffeine, theobromine, 1,9-dimethyl-methylene blue (DMMB), chondroitin sulfate (CS), doxorubicin hydrochloride (DOX), HEPES, Sephadex G75 and *phosphate buffered saline* (PBS) were purchased from Sigma-Aldrich (St. Louis, MO). LysoTracker Green DND-26 and Hoechst 33342 were obtained from Invitrogen Life Technologies (Grand Island, NY). Fetal bovine serum, DMEM medium and RPMI 1640 medium were purchased from Mediatech (Manassas, VA). Penicillin (10000 units/ml)-streptomycin (10000 µg/ml) solution was obtained from MP biomedicals (Solon, OH). RAW 264.7 murine macrophages (TIB-71) and human non-small-cell lung cancer A549 cells (CCL-185) were obtained from the American Type Culture Collection (Manassas, VA). The human breast tumor cell line MCF-7 and its resistant cell line MCF-7/ADR were obtained from the Frederick National Laboratory for Cancer Research (Frederick, MD).

Preparation of Tea Nanoparticles (TNPs)

Green tea infusions were made by steeping 15 g of dried green tea leaves in 200 ml of boiling deionized water (DI water) for 20 minutes. The resulting hot tea infusion was then centrifuged at 5000 rpm for 10 min, and the supernatant was filtered through a 1 µm filter (Whatman Inc., Florham Park, NJ). The filtered

solution was then sonicated in a water-bath sonicater (model 750D, VWR) at room temperature for 30 min. The free small molecules, such as alkaloids, and polyphenols, were removed by dialysis using 300KD MWCO tubing against DI water for 3 days at room temperature. Size-exclusion high-performance liquid chromatography (SEC-HPLC) was used to further isolate the nanoparticles after dialysis. 250 µl of the dialyzed solution was loaded onto a SEC-HPLC column (Phenomenex® BIOSEP-SEC-S4000), and eluted with distilled water at 1.0 ml/min of flow rate. The UV absorption at 280 nm was measured, and all fractions were collected.

Determination of Chemical Components of TNPs

The total amounts of polysaccharides were measured using the anthrone-sulfuric acid assay [54]. Briefly, the anthrone reagent was prepared freshly before analysis by dissolving 0.02 g of anthrone (0.2%) in 10 ml of concentrated sulfuric acid (98%). A standard glucose solution was prepared in PBS and serially diluted to 0, 15.625, 31.25, 62.5, 125, and 250 µg/ml. 0.2 ml of the glucose standards or tea nanoparticle solution (1mg/ml) was added to 0.5 ml of the freshly prepared 0.2% anthrone-sulfuric acid. The mixture was stirred immediately and incubated in boiling water for 15 min. All samples were then put on ice for 5 min to stop the reaction. After keeping 10 min at room temperature, samples were placed in a 96-well plate, and read at 620 nm in a microplate reader (Bio-Tek µQuant). The amount of proteins in the TNPs was determined using a bicinchoninic acid (BCA)

protein assay kit (Pierce) following the manufacturer's instructions. Small molecules present in the TNPs, i.e. EGCG, caffeine and theobromine, were determined by the RP-HPLC method as reported previously.[55] Briefly, HPLC analysis was conducted on a Agilent 1200 series HPLC system equipped with DAD detector. The DAD acquisition wavelength was set from 200 to 400 nm, with output channel A at wavelength 280 nm and output channel B at 360 nm. 1 mg of the freeze-dried TNP sample was dissolved in 70% methanol solution, then incubated at room temperature for three hours and filtered through 0.22 μm filters (Carrigtwohill, Co. Cork, Ireland). 10μl of the filtered samples were then analyzed on an Eclipse XDB-C18 (4.6 mm ×150 mm, 5 μm) column. Gradient elution was performed by varying the proportion of solvent A (water-acetic acid, 97:3 v/v) to solvent B (methanol), with the flow rate of 1 ml/min. The mobile phase composition started at 100% solvent A for 1 min, followed by a linear increase of solvent B to 63% in 27 min, and then go back to the initial conditions in 2 min for the next run.

Characterization of TNPs

10μl of the TNP solution was air-dried on a silicon substrate or glass cover slip for SEM and AFM analysis to characterize the particle size and morphology of the TNPs. The SEM analysis was performed using a high resolution FE-SEM system (LEO 1525, Germany). AFM analysis (MFP-3D, Asylum Research, Santa Barbara, CA) was operated based on the software Igor Pro from Wavemetrics in AC mode, and an ACTA Probe from AppNano (Santa Clara, CA) at room

temperature. The samples were further analyzed by dynamic light scattering (DLS) and electrophoretic light scattering (ELS), using a Zetasizer Nano (Malvern Instruments Ltd, Worcestershine, UK), to determine the size distribution and zeta potential of the TNPs in solution.

In Vitro Immunostimulatory Activity

The mouse macrophage cell line, RAW 264.7, was incubated for 24 h in DMEM culture medium supplemented with 10% FBS and 1% penicillin-streptomycin at 37°C in 5% CO_2. The cells were then plated in 12-well plates at a density of 5×10^6 cells/ml and cultured for 24 h. The TNP samples at the concentration of 50μg/ml were added in each well. After incubation for 24 h, the supernatants were collected for ELISArray analysis. Mouse common cytokines and chemokines multi-analyte ELISArray kits (SABiosciences Corporation, Frederick, MD) were used to determine various cytokines (IL-1A, IL-1B, IL-2, IL-4, IL-6, IL-10, IL-12, IL-17A, IFNγ, TNFα, G-CSF, and GM-CSF) and chemokines (RANTES, MCP-1, MIP-1a, MIP-1b, SDF-1, IP-10, MIG, Eotaxin, TARC, MDC, KC, and 6Ckine) in the supernatants following the manufacturer's instructions.

Preparation and Characterization of Doxorubicin (DOX)-loaded TNPs

The DOX-loaded TNPs were prepared by mixing DOX (0.3 mM) with the TNPs (1mg/ml) in HEPES buffer (20mM, pH=7.0) at room temperature for 3 hours. The DOX loaded into the TNPs were isolated from the free DOX in the solution by a

Sephadex G75 column method as previously reported.[56] The concentration of DOX loaded into the TNPs was determined by the DOX characteristic peak at 480 nm. The absorbance was measured by a microplate reader (Bio-Tek μQuant). In order to evaluate the effect of pH on drug loading to the TNPs, the DOX-loaded TNPs were prepared under different pH conditions (20mM HEPES buffer, pH=7.0, 5.5 and 3.5). After incubation at room temperature for 3 hours, samples were applied to the Sephadex G75 column, and eluted with 20 mM HEPES buffer under the corresponding pH values. Elution profiles of the DOX-loaded TNPs (λ=480 nm) were plotted versus elution volumes. In order to characterize the hydrophobic interactions between DOX and the TNPs, the ultraviolet and visible (UV-Vis) spectra of the blank TNP solution, the DOX-loaded TNP solution, and free DOX solution (with the same DOX concentration) were measured using a Thermo Scientific Evolution 600 UV-Visible spectrophotometer. Fluorescence spectra of the DOX-loaded TNPs and free DOX were then measured by using a spectrofluorimetry (LS-50B, Perkin Elmer) at the wavelength of 480nm (excitation). Fourier-transform infrared spectroscopy (FTIR) was finally performed to determine the possible binding effect of DOX and the TNPs. The DOX-loaded TNPs, and the blank TNPs were freeze-dried prior to FTIR analysis. Dry powders were mixed with potassium bromide, and transmission spectra were acquired with a Bruker Vertex 70 FT-IR spectrometer (Bruker Optics Inc, Billerica MA), equipped with a deuterated triglycine sulfate detector and controlled by the OPUS 6.5 software package.

In Vitro Release of DOX from TNPs

In vitro release of DOX from the TNPs under acidic and neutral conditions (pH=5.0, 6.0 and 7.5) was evaluated. The release study was conducted in phosphate buffered saline (PBS, pH=7.5 and 6.0) and 0.1 M acetate buffer (pH=5.0) at room temperature with moderate shaking. Briefly, 1 ml of the DOX-loaded TNPs or free DOX solution (with the same concentration of DOX= 0.1mM) was added to a dialysis membrane tube (MWCO= 12KD) and immersed in a glass container containing 30 ml of release buffers. 0.5 ml of the released solution was collected at different time intervals and replenished immediately with the same volume of the corresponding fresh medium. DOX release profiles were determined by a Synergy HT multi-detection microplate reader (Bio-Tek Instruments Inc., Winooski, VT) at 480 nm excitation and 590 nm emission.

Cellular Uptake and Confocal Microscopic Study of DOX-loaded TNPs

The quantification of intracellular DOX uptake in cancer cells was evaluated by flow cytometry. In general, A549, MCF-7 and MCF-7/ADR cells were cultured in 6-well plates at densities of 1×10^6 cells/ml, and incubated at 37°C in 5% CO_2. The DOX-loaded TNPs or free DOX solution at 10μM of DOX concentration were added into the wells and incubated at 37°C for 1h, 2h, and 3h, respectively. The media were aspirated and cells were rinsed with PBS for three times. Flow cytometry analysis was carried out on an Epics XL Analyzer (Beckman Coulter Inc., Brea, CA) by collecting 20000 events for each sample and measuring the cell associated fluorescence. Confocal laser scanning microscopy (CLSM) was

used to investigate intracellular DOX distribution in the above three cell lines treated with the DOX-loaded TNPs, and free DOX was used as a control. Briefly, the cells were seeded on cover slips with a density of 10^6 cells/ml in a 6-well plate and cultured at 37°C in 5% CO_2 for 24 h. The cells were then treated with the DOX-loaded TNPs at 10 µM of DOX concentration for 1 h and 3h. To observe the intracellular distribution, endolysosome and nuclear markers, LysoTracker® green (100 nm) and Hoechst 33342 (4µM) were incubated with the cells for 30 min prior to the confocal visualization. The cover slip was washed with PBS three times and then set on a microscope slide and examined by CLSM.

In Vitro Cytotoxicity

The cytotoxicity of the DOX-loaded TNPs against A549, MCF-7 and MCF-7/ADR was evaluated by MTT (3-[4,5-dimethylthiazol-2-yl]-2,5-diphenyl tetrazolium bromide) assay.[57] Briefly, 5000 cells were plated in 96-well plates in 100 µl DMEM (for A549 cells) or RPMI 1640 (for MCF-7 and MCF-7/ADR cells) and supplemented with 10% fetal bovine serum (FBS) and 1.0 % penicillin-streptomycin per well and incubated at 37 °C in 5% CO_2 for 24 h to allow the cells to attach. The cells were then treated with different concentrations of the DOX-loaded TNPs for 48 h. Free DOX and the blank TNPs were used as controls. After the 48 h treatment, 10 µl of MTT solution (5 mg/ml in PBS; pH 7.4) was then added to each well and the plates were incubated for another 4 h. The cell culture media were removed and replaced with 100 µl DMSO. The absorbance was measured by a microplate reader (Bio-Tek µQuant) at 570 nm,

and the average IC_{50} (the dose having 50% cell inhibition) value was determined by cell survival plots using the “DoseResp” function in OriginPro 8.0.

Statistical Analysis

Values were presented as mean ± standard deviation (S.D.) of at least three independent measurements. Statistical significance was tested by one-way ANOVA followed by a Student's *t* test for multiple comparison tests. A *p* value of <0.05 was considered statistically significant.

Results and Discussion

Spherical nanoparticles isolated from tea infusion

An infusion-dialysis based procedure was developed to isolate nanoparticles from tea infusion **(Figure 1A-B)**. To remove the large debris, the tea infusion was centrifuged at 5000 rpm for 10 min. The supernatant was then filtered through a 1µm filter, and dialyzed to remove any compounds with MW of less than 300KD. To further validate the infusion-dialysis based procedure, size exclusion chromatography-high performance liquid chromatography (SEC-HPLC) analysis was utilized for separating the tea infusions before and after the dialysis. As shown in **Figure 1**, there were multiple UV peaks at 280 nm that occurred at different elution times before the dialysis (**Figure 1B**), while only one well-defined peak was detected at 0-10 min after the dialysis (**Figure 1D**). The single peak in the SEC-HPLC profile indicated that the dialyzed sample was more homogenous and likely contained a narrow range of nanoparticles.[58] To determine if the nanoparticles could be found in the fraction collected from this peak, the sample was scanned using AFM and SEM. As hypothesized, AFM images (**Figure 2A-B**) showed clearly that abundant spherical nanoparticles with diameters in the range of 100-300 nm were observed. Similarly, SEM analysis revealed the presence of abundant spherical nanoparticles in the range of 50-200 nm in diameter (**Figure 2C)**. To determine the size distribution of the TNPs in solution, DLS was conducted on the TNP containing fraction. Results in **Figure 3** and **Table 1,** the tea nanoparticles showed a relatively broad distribution of size with a mean hydrodynamic diameter of 318.3 nm.

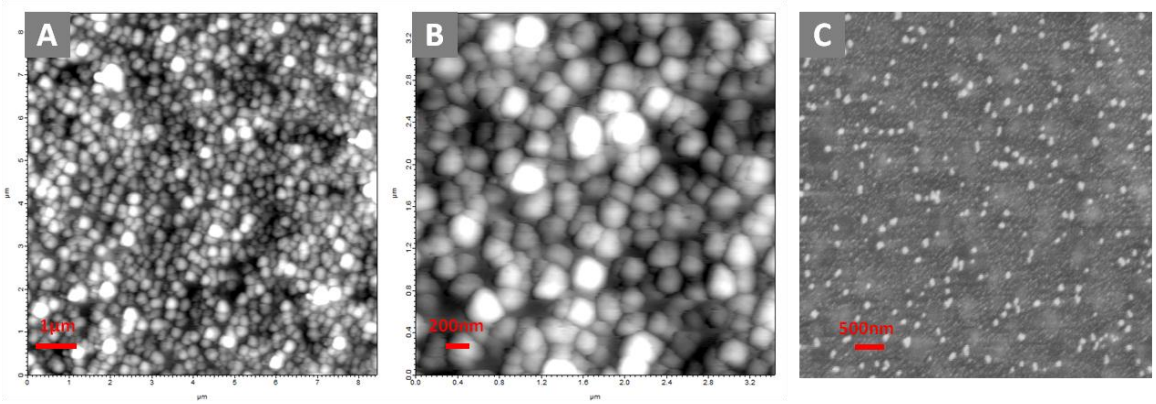

Figure 2 AFM (A-B) and SEM (C) images of the TNPs obtained from the green tea infusion.

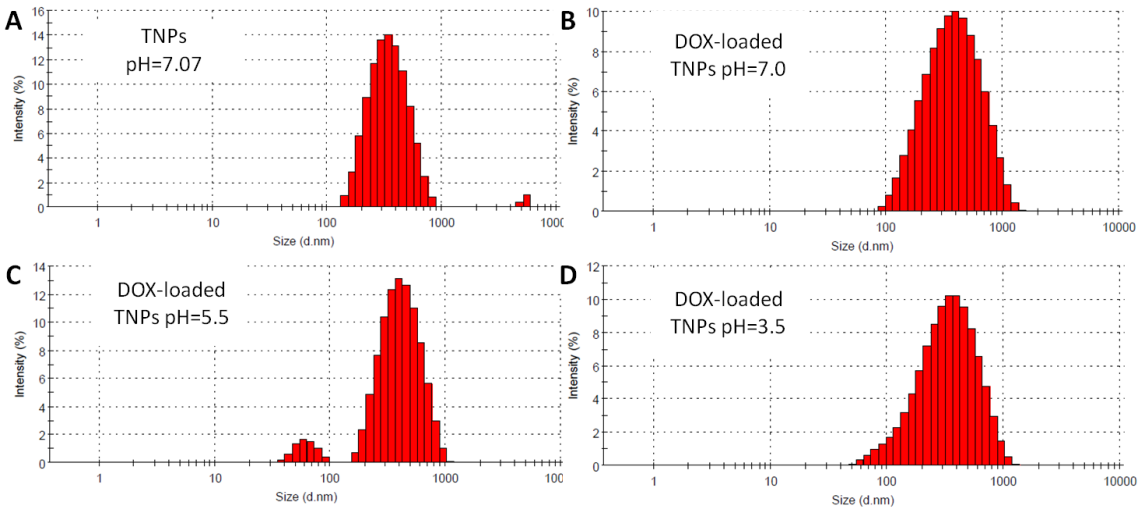

Figure 3 The size distribution of the TNPs at pH= 7.0 (A), and the DOX-loaded TNPs at pH= 7.0 (B), pH= 5.5 (C), and pH= 3.5 (D) in suspension measured by DLS.

Table 1 Characteristics of the TNPs and the DOX-loaded TNPs.

Samples	***Diameter [nm]***	***PDI***	***Zeta potential [mV]***	***Protein [μg/mg]***	***Polysaccharide [μg/mg]***
TNPs (pH=7.0)	318.3	0.324	-26.52±2.21	453.36±7.71	189.12±9.03
DOX-loaded TNPs (pH=7.0)	287.0	0.305	-6.34±1.49	--	--
DOX-loaded TNPs (pH=5.5)	301.6	0.292	-8.30±1.35	--	--
DOX-loaded TNPs (pH=3.5)	271.9	0.275	-9.15±0.33	--	--

Further, the surface charge potential of the TNPs was analyzed using ELS. The TNPs were found to be -26.52±2.21 mV at pH 7.0. The results from this analysis clearly demonstrated that the method developed for isolating nanoparticles from green tea infusion was effective, leading to a stable population of the TNPs. At present, it is not well understood how the nanoparticles are formed in tea, and what roles they play in the growth and development processes of green tea. However, several studies have reported the observation and tentative components of the nanoparticles in black tea.[43, 59] In 1995, a study reported nanoparticles in aqueous black tea extracts formed on cooling.[43] The black tea nanoparticles showed particle size of about 200-300 nm, similar to the nanoparticles isolated from green tea in this study. A study in 1963 [59] proposed that the main components in black tea nanoparticles were caffeine, theaflavins and the thearubingins; however, there was no direct evidence to validate these tentative components in their paper.[43] Due to the use of the infusion-dialysis based procedure for the TNP isolation in our study, small molecules not complexed with the TNPs were removed, thus several bioactive phytochemicals in green tea were not expected to be contained in the TNP fraction. In order to validate this assumption, we have analyzed the concentrations of three common phytochemicals from green tea, including (-)-epigallocatechin gallate (EGCG), caffeine and theobromine, using the reversed phase HPLC (RP-HPLC) method. To effectively solubilize these small molecules from the TNPs, a single extraction with methanol was used[60]. As shown in **Figure 4A-C,** the UV 280nm

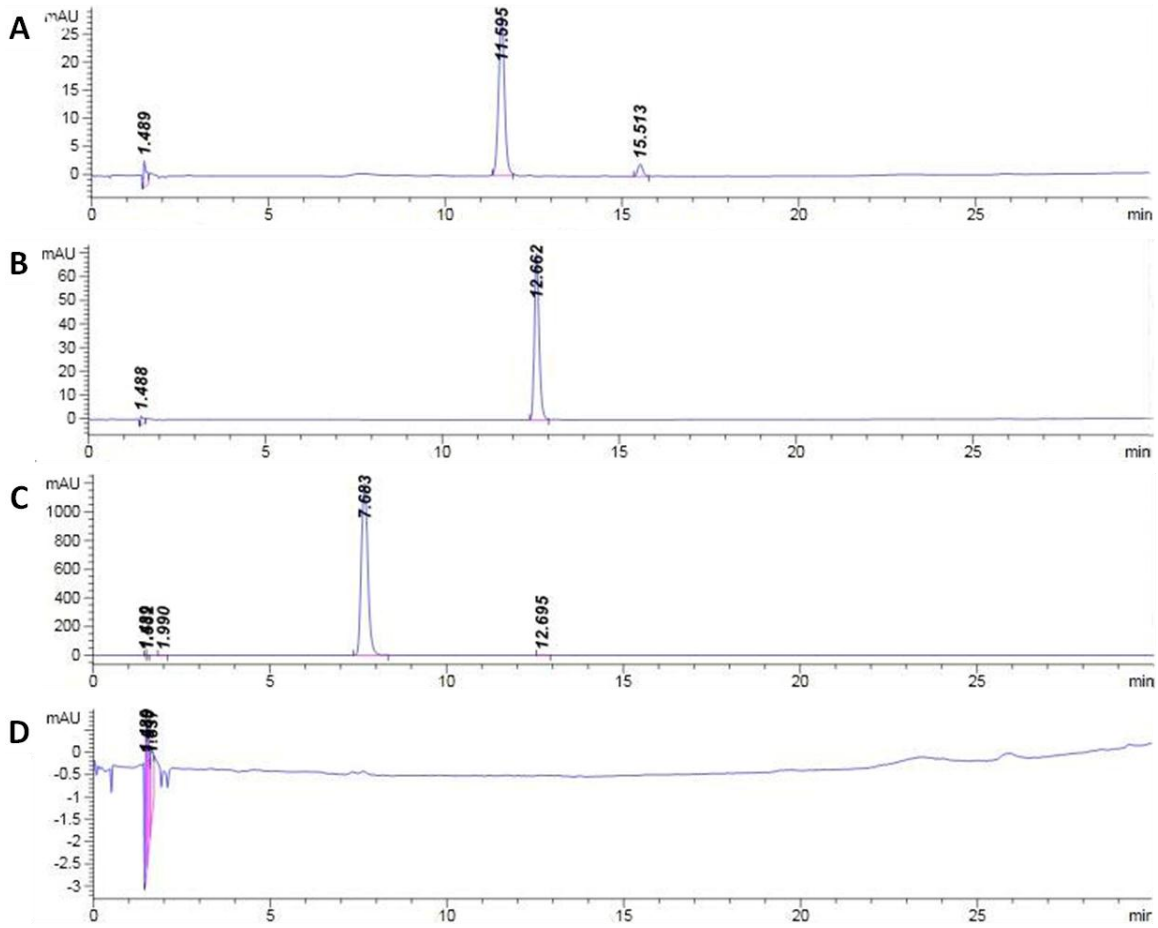

Figure 4 HPLC chromatograms of EGCG (A), caffeine (B), theobromine (C) as standards, and isolated TNPs (D) at 280 nm.

peaks of 10 μg/ml EGCG, caffeine and theobromine standards appeared at respective retention time of 11.59, 12.66 and 7.68 min. However, no peak from EGCG, caffeine and theobromine was observed in the TNP fraction, indicating that they were not present in the TNPs (**Figure 4D**). To further investigate the possible chemical components of the TNPs, we detected the concentrations of two common macromolecules (i.e., protein and polysaccharide) in the TNPs, measured by the BCA protein assay and anthrone-sulfuric acid method, respectively. As shown in **Table 1**, there were about 453.36 μg proteins and 189.12 μg polysaccharides in 1 mg TNPs. According to previous studies, the polysaccharides from green tea were believed to be a typical heteropolysaccharide and consisted of mannose, ribose, rhamnose, glucuronic acid, galacturonic acid, glucose, xylose, galactose and arabinose [61], and some acidic polysaccharides were reported to be bound to protein [62]. Considering the excellent biocompatibility of green tea, although there is no complete dissection for all components in these new natural nanoparticles, the two confirmed components, polysaccharide and protein, can still provide an opportunity for us to explore the potential biomedical application of the TNPs (**Figure 1E-F**).

Immunostimulatory effect of TNPs on RAW 264.7 mouse macrophages

As is well-known,polysaccharides isolated from a wide range of plants, including higher plants, mushrooms, lichens and algae often have macrophage modulatory effects [63], and thus are promising candidates for therapeutics in

immunomodulatory, anti-tumor and wound healing applications [63, 64]. Polysaccharides from green tea have also been reported to possess immunological and anti-cancer properties both *in vivo* and *in vitro* [65, 66]. Inspired by these studies, we have evaluated the potential immunological effect of the TNPs *in vitro*. It is well-known that macrophages as the first line of host defense can function as antigen-presenting cells, and interact with other immune cells to modulate the immune response [63]. For cancer treatment, macrophages mediate tumor cytotoxicity via the production of various cytokines and other immune factors [67]. Testing the secretion of cytokines and chemokines from macrophages induced by potential immunostimulatory substances is a common approach to evaluate their immunostimulatory activity [68]. Using a murine-derived macrophages RAW 264.7, we first tested 12-cytokine profiles, including IL-1A, IL-1B, IL-2, IL-4, IL-6, IL-10, IL-12, IL-17A, IFN-γ, TNF-α, G-CSF, and GM-CSF, after treatment with 50μg/ml of the TNPs. It is noteworthy that the levels of IL-6 ($p<0.01$), TNF-α ($p<0.05$) and G-CSF ($p<0.01$) were significantly increased after incubation of RAW 264.7 macrophages with the TNPs for 24 h as indicated by ELISArray (**Figure 5A)**. TNF-α is a multifunctional cytokine that plays a key role in apoptosis, cell survival, inflammation and immunity. The importance of TNF-α in the immune system mainly stems from its ability to interact with different receptors, and then activate several signal transduction pathways, leading to the diverse functions, especially its immunostimulatory effect [69]. It has also been reported that TNF-α could act synergistically with other drugs at the molecular level to trigger the apoptosis and dissociation of tumor vascular endothelial cells

in cancer treatment.[70, 71] IL-6 has been recognized as an important host defense molecule that can affect tumor cells.[72] It also plays key roles in T-cell-mediated immune responses, acting as a cofactor for T-cell proliferation.[73] G-CSF has a variety of functions including the induction of proliferation, survival and differentiation of hematopoietic cells, as well as mobilization of bone marrow cells.[74] Because G-CSF can stimulate the differentiation of bone marrow stem cells, and promote the mobilization of hematopoietic precursor cells from the bone marrow into the bloodstream,[75] it has been reported to be used in many cancer patients to prevent and counterbalance chemotherapy-associated neutropenia.[76] In addition to the ability of the TNPs to stimulate IL-6, TNF-α, and G-CSF secretion, secretion profiles of the 12 chemokines, including RANTES, MCP-1, MIP-1a, MIP-1b, SDF-1, IP-10, MIG, Eotaxin, TARC, MDC, KC, and 6Ckine, were also analyzed. As shown in **Figure 5B**, significantly enhanced productions of RANTES ($p<0.01$), IP-10 ($p<0.05$) and MDC ($p<0.01$) were observed after incubation with the TNPs. The primary function of chemokines is chemoattraction and activation of specific leucocytes in various immune-inflammatory responses. Besides their actions on haematopoietic cells, chemokines were also demonstrated to induce distinct effects in stromal and solid tumour cells.[77] RANTES was the first chemokine reported to mediate anti-tumor immunity in part through direct T cell effector recruitment.[78, 79] IP-10 has been suggested to exhibit anti-tumor and anti-metastatic properties, and its immunological properties appear to be dependent on the attraction of monocytes

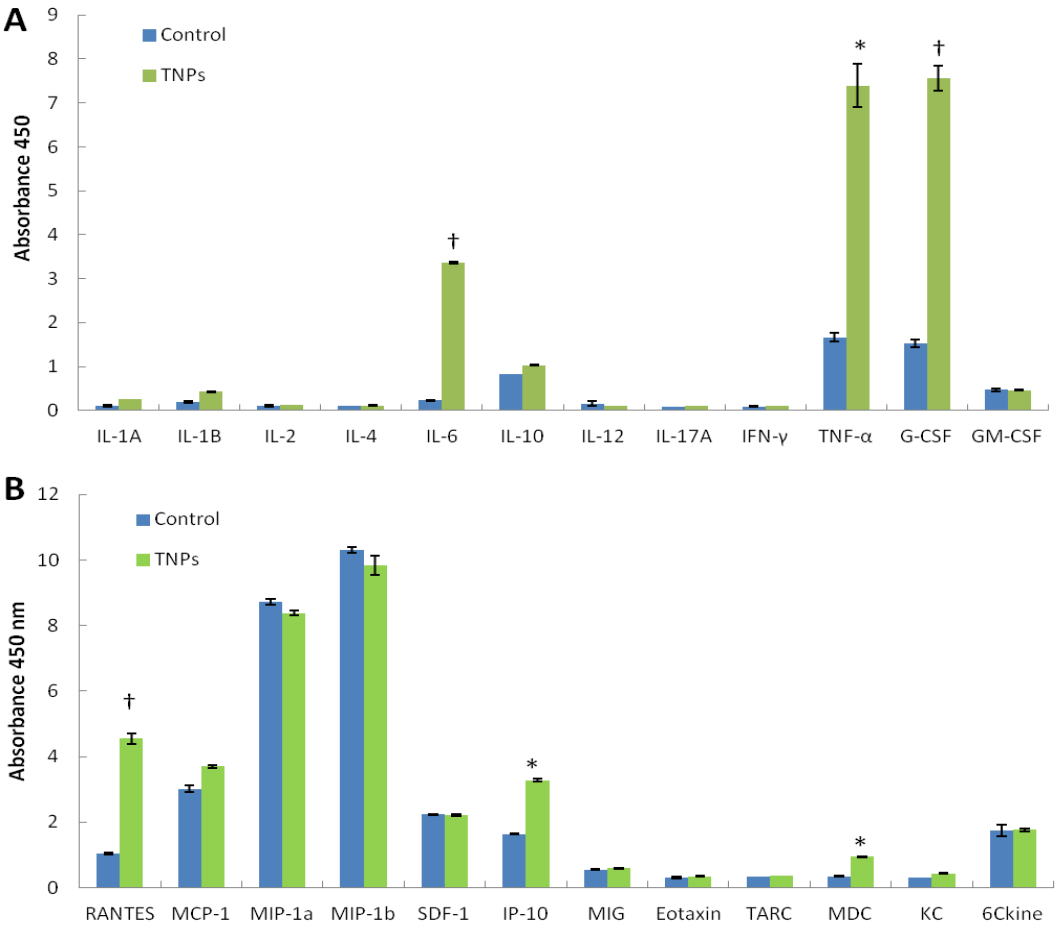

Figure 5 Effects of the TNPs (50μg/ml) on in vitro secretion of cytokines

Effects of TNPs (50ug/ml) on in vitro secretion of cytokines (IL-1A,IL-1B, IL-2, IL-4, IL-6, IL-10, IL-12, IL-17A, IFN-γ, TNF-α, G-CSF, and GM-CSF), and chemokines (RANTES, MCP-1, MIP-1a, MIP-1b, SDF-1, IP-10, MIG, Eotaxin, TARC, MDC, KC, and 6Ckine) by RAW264.7 macrophage cells. (A) Inductions of cytokines (IL-6, TNF-α and G-CSF) were determined by ELISArray in supernatants of the cells cultured for 24 h. (B) Secretion of chemokines (RANTES, IP-10 and MDC) were determined by ELISArray in supernatants of the cells cultured for 24 h. The values stand for means ± SD obtained from three independent experiments. *P<0.05 and †P< 0.01, as compared with the controls.

and T lymphocytes.[80] Moreover, IP-10 can induce tumor regression and immunity to subsequent tumor challenge.[77, 81] There is also *in vivo* evidence indicating that MDC is identified in diversion of effective antitumor responses.[82] These evidences indicate that the TNPs may exert various beneficial pharmacological effects, especially antitumor effect, via their ability to modulate macrophage immune function.

DOX loading in TNPs via electrostatic and hydrophobic interactions

As mentioned above, the TNPs have a surface potential of ~-26mV at pH7.0, which is a desirable property for binding cationic chemo-drugs. To test the potential of the TNPs as a nanocarrier, complexation of the isolated TNPs with the cationic cancer theraputic DOX was conducted. Typically, there are two ways to load DOX onto nanoparticles: electrostatic binding of cationic DOX to nanoparticles, and entrapment of the neutral DOX with hydrophobic groups.[83] Considering the negative surface potential of the TNPs at the physiological pH, the complexation of DOX with the TNPs through electrostatic interactions was performed. For this purpose, 0.3mM of DOX was mixed with 1mg/ml of the TNPs in 20mM HEPES buffer (pH 7.0) and incubated for 3 hours at room temperature. After loading the mixture onto a Sephadex G75 column, the DOX-loaded TNPs were collected from the first peak of the elution profile.[56] As shown in **Figure 6A**. the first peak (5-10 ml) stands for the DOX-loaded TNPs, while the second peak (11-20 ml) represents the free DOX.[56] The association efficiency of DOX loaded onto the TNPs was 46% at pH 7.0. The average diameter of the DOX-

loaded TNPs was similar to the blank TNPs; however the DOX-loaded TNPs showed a lower zeta potential (-6.34 mV) as compared with that of blank TNPs (-26.52 mV) (**Table 1**). This decrease in zeta potential suggests that the positively charged DOX molecules may be adsorbed onto the negatively charged TNPs through electrostatic interactions. To verify this hypothesis, 1mg/ml of TNP solution was mixed with 0.3mM of DOX at various pH (7.0, 5.5 and 3.5). The loading profiles of DOX to the TNPs under different pH values were recorded by separating the DOX-loaded TNPs from free DOX using G75 column. As shown in **Figure 6A**, compared with pH 7.0, there was a slight decrease for the amount of DOX loaded onto the TNPs at pH 5.5, while when the pH was adjusted to 3.5, the area of the first peak decreased dramatically and the second peak increased, indicating that DOX was not efficiently loaded. While a clear difference in loading was observed at pH 3.5, the average diameters and size distributions of the DOX-loaded TNPs under different pH did not show a clear difference (**Figure 3**). Apart from the electrostatic interaction between DOX and the TNPs, hydrophobic interactions may also contribute to the formation of the DOX-loaded TNPs. As shown in **Figure 6B-C**, compared to free DOX, a significant DOX fluorescence quenching effect in the DOX-loaded TNP sample was observed, while there was no significant decrease in UV absorption for the DOX-loaded TNPs at the same DOX concentration. This data suggests that hydrophobic interactions may lead to complexation of DOX to the TNPs, and the resulting quenching effect may be due to the dense packing of the DOX molecules on the nanoparticle surface.[84]

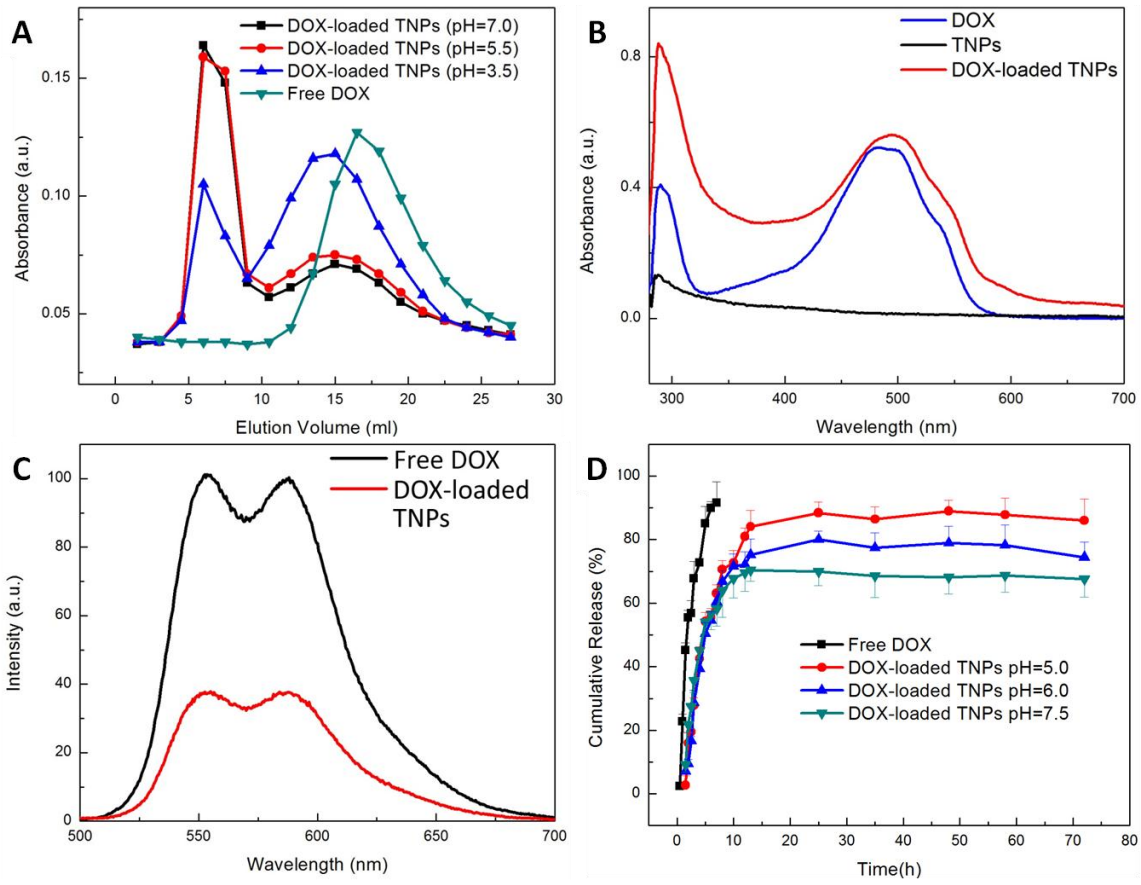

Figure 6 Characterization of the DOX-loaded TNPs.

(A) Loading profiles of DOX to TNPs under various pH conditions: acidic (pH= 3.5 and 5.5), and neutral (pH= 7.0). With the decrease of the pH value, the binding between the TNPs and DOX decreased. (B) UV-Vis absorbance spectra of DOX (blue), the TNPs (black), and the DOX-loaded TNPs (red) solution. Characteristic DOX absorption peak is at 480nm. (C) Fluorescence spectra of free DOX and the DOX-loaded TNPs solutions with the same DOX concentration (5 μM) under 480 nm excitation. A quenching effect of DOX fluorescence was observed for the DOX-loaded TNPs. (D) Release profiles of DOX from the TNPs under different pH conditions (pH=5.0, pH=6.0 and pH=7.5). Free DOX was used as a control.

To further evaluate whether covalent bonds were available between the TNPs and DOX, the DOX-loaded TNPs were characterized by FTIR, using free DOX and the TNPs as controls. Comparing the FTIR spectrum of the DOX-loaded TNPs with those of the blank TNPs and free DOX, there were additional absorption bands at ~1734 and 1289 cm^{-1} corresponding to the C-O-CH_3 stretching bands of DOX (**Figure 7**), indicating DOX was successfully loaded onto the TNPs. No other new peaks appeared or shifted, suggesting that there was no covalent bonding between DOX and the TNPs.

pH-responsive DOX release from TNPs

In order to evaluate the potential of the TNPs as a nanocarrier for cancer treatment, DOX release behavior from the DOX-loaded TNPs was evaluated at neutral and acidic pH by using buffers with varying pH values (pH=5.0, 6.0 and 7.5). As shown in **Figure 6D**, more than 90% of free DOX was released under the neutral condition after 6 hours, while the release of DOX from the TNPs under different pH values reached a plateau after 25 hours. The sustained DOX release from the TNPs demonstrated that the release process is a pH-responsive release at various pH conditions. During the first 10 hours of the first-order release curve, there was no significant difference in the cumulative release of DOX from the TNPs at both neutral and acidic pH, presumably because the hydrophobic interaction dominated the stability of the DOX-loaded TNPs, when more DOX was associated with the nanoparticles [85].

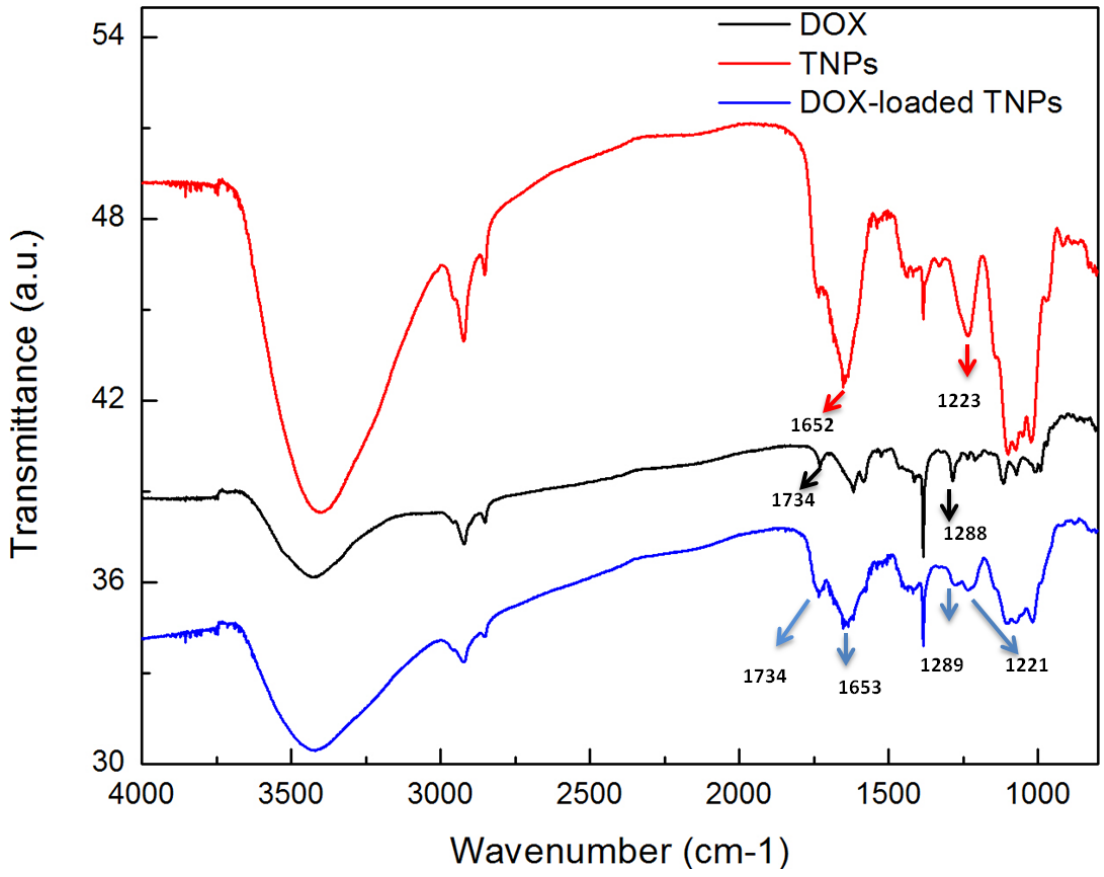

Figure 7 FTIR spectra of DOX (black), the TNPs (red), and the DOX-loaded TNPs (blue).

The absorption bands at ~1734 and ~1289 cm^{-1} correspond to the C-O-CH_3 stretching bands of DOX. The band around 1652 cm^{-1} and 1223 cm^{-1} may be due to the C=O and CN stretch vibrations of amide, which comes from proteins and polysaccharides of the TNPs. For the spectrum of the DOX-loaded TNPs, the bands all come from DOX and the TNPs, and no other new peaks appeared or shifted, suggesting that there is no covalent bonding between DOX and the TNPs.

While after 10 hours, the cumulative release of DOX from the TNPs was significantly higher in the acidic condition compared with the neutral condition. About 88% of DOX was released from the TNPs under the acidic condition at pH 5.0, while around 80% and 70% of DOX was released under pH 6.0 and 7.5 after 25 hours. It likely indicated that the dominant driving force maintaining the stability of the DOX-loaded TNPs was gradually shifted to the electrostatic interaction between DOX and the TNPs, due to the fact that a majority of DOX (~70%) released and less DOX remained in the TNPs.[85] Since acidic conditions could potentially cause a decrease in the negative charges on the TNPs, the binding between the TNPs and DOX was weakening, and more DOX was disassociated from the TNPs with the decrease of the pH value. The pH-responsive drug release behavior is regarded as a favorable property for *in vivo* antitumor applications.[86] Since only small amounts of DOX release in the blood circulation (pH=7.4), more active drug could be released after reaching the target, as a result of the lower pH in the tumor tissue or in the endosomes (pH=~ 5) after entering into cells via endocytosis.[86] Thus, the pH-responsive release property of DOX from the TNPs would probably make them to be used as an effective nanocarrier for drug delivery in cancer treatment.

TNPs facilitate intracellular DOX delivery in sensitive and resistant tumor cells

The quantitative determination of DOX uptake in cancer cells was conducted by flow cytometry. Two sensitive tumor cell lines, A549 human lung cancer cells and

MCF-7 breast cancer cells, were incubated with the DOX-loaded TNPs at a DOX concentration of 10 μM for1 h, 2 h and 3 h. The cell-associated fluorescence intensity, which was directly proportional to the amount of DOX internalized in cells, was then measured.[87] **Figure 8A-F** show the flow cytometry histograms of DOX fluorescence from both cells incubated with the DOX-loaded TNPs, free DOX and the blank TNPs. For all time points, the treatment of the DOX-loaded TNPs showed a significant increase in the level of DOX uptake compared with free DOX. To test if the TNPs could also increase the uptake and accumulation of DOX in drug-resistant cancer cells, the uptake of the DOX-loaded TNPs and free DOX by resistant MCF-7/ADR breast cancer cells was evaluated. As shown in **Figure 8G-J**, compared with free DOX, the intracellular accumulation of DOX increased from 1h to 3h in the resistant MCF-7/ADR cells treated with the DOX-loaded TNPs. The above data suggested that the DOX-loaded TNPs could provide an alternative treatment option for drug-resistant tumors.[88] To assess the intracellular distribution of the DOX-loaded TNPs, we incubated both sensitive cell lines with the DOX-loaded TNPs at a DOX concentration of 10 μM for 1h and 3 h, and then conducted confocal laser scanning microscopy (CLSM). The nucleus and endolysosomes were labeled with the nucleus-selective dye (Hoechst 33342, blue), and acidic endolysosomes-selective dye (LysoTracker®, green DND-26), respectively. As shown in **Figure 9,** the intracellular distribution of the DOX-loaded TNPs was different from that of free DOX in both cells. After 1h incubation, treatment of both cells with free DOX resulted in weak DOX fluorescence in the cytoplasm.

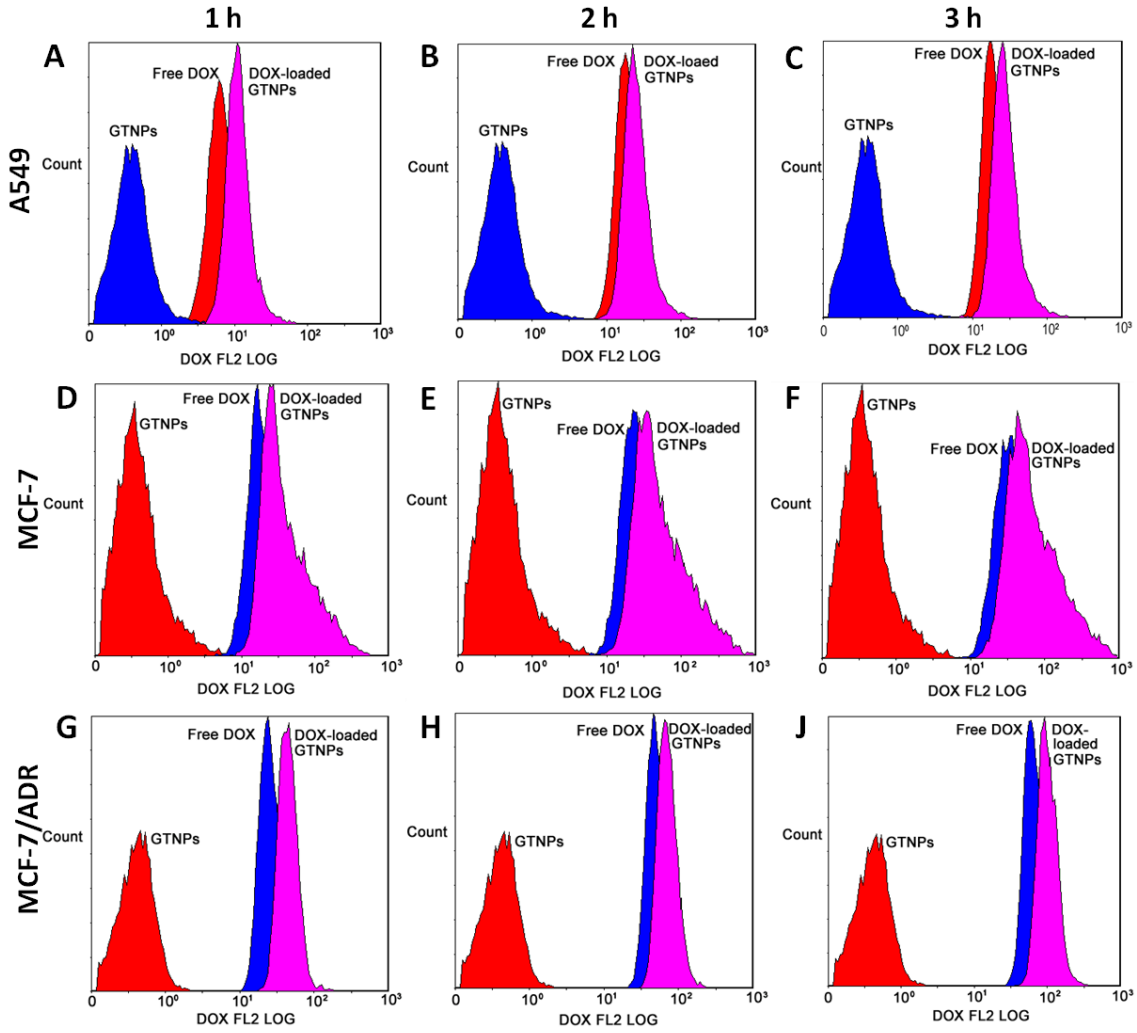

Figure 8 Quantitative flow cytometry analysis for intracellular uptake of free DOX and the DOX-loaded TNPs

Quantitative flow cytometry analysis for intracellular uptake of free DOX and the DOX-loaded TNPs in A549 (A-C), MCF-7(D-F) and MCF-7/ADR (G-J) cells at different time points (1h, 2h and 3h). All cells were treated with the DOX-loaded TNPs and free DOX at the same DOX concentration of 10 μM for different time intervals.

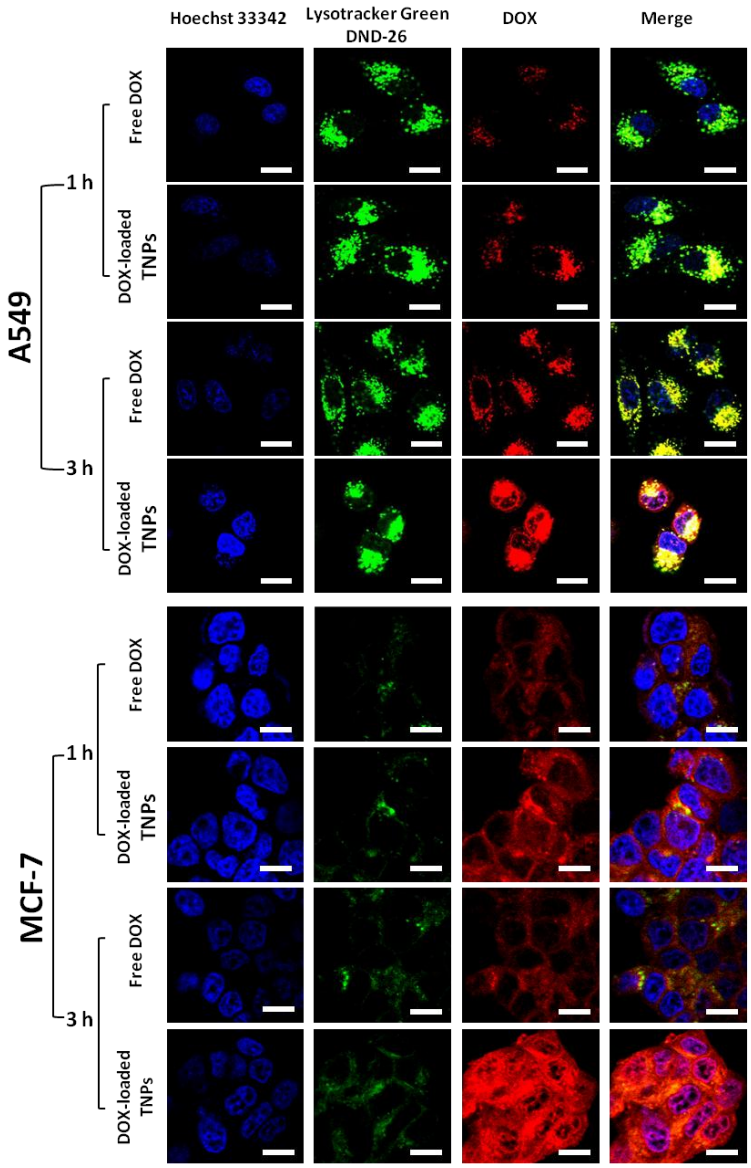

Figure 9 CLSM images of the intracellular distributions of the DOX-loaded TNPs in A549 and MCF-7 cells.

CLSM images of the intracellular distributions of the DOX-loaded TNPs and free DOX with the same DOX concentration (10μM) in sensitive human lung cancer A549 and human breast cancer MCF-7 cells for different time incubation (1 h and 3 h). The cells were stained with Lysotracker® green DND-26 (green) and Hoechst 33342 (blue). The pink color shows the localization of DOX (red) in nucleus (blue), and the yellow color indicates the localization of DOX (red) in endosomes/lysosomes (green). The scale bars represent 10 μm.

However, for the DOX-loaded TNPs treatment, stronger DOX fluorescence could be detected in the cytoplasm in both cells. Differences in intracellular distribution of the DOX-loaded TNPs and free DOX in both cells were also obtained after 3h treatment. The intense DOX fluorescence was visualized in both cytoplasm, and the nucleus for the treatment of the DOX-loaded TNPs, while in the treatment of free DOX, it appeared that there was less DOX fluorescence in the cytoplasm and a smaller amount of DOX fluorescence in the nucleus. These results are consistent with the cellular uptake investigated by flow cytometry in **Figure 8A-F**. In terms of DOX localization in both cells, a large fraction of the DOX-loaded TNPs was found to be entrapped in endolysosomes after 1 h incubation, while more DOX fluorescence was observed to be out of endolysosomes and localized in cytoplasm and nucleus after 3h incubation (**Figure 9**). Since the enhanced uptake of the DOX-loaded TNPs was also observed in resistant cells by flow cytometry, we visualized their intracellular distribution in MCF-7/ADR cells to further assess the potential of the TNPs for cancer treatment. As shown in **Figure 10**, after 1h treatment, small amount of DOX was localized in the cytoplasm of MCF-7/ADR cells; however, more DOX fluorescence accumulated in the discrete cytoplasm area was observed, when the MCF-7/ADR cells were treated with the DOX-loaded TNPs. For 3h treatment, most free DOX accumulated in discrete granules in the cytoplasm, and a little was observed in nucleus.

In case of the DOX-loaded TNPs, significant increase of intracellular DOX fluorescence was observed in both nucleus and cytoplasm.

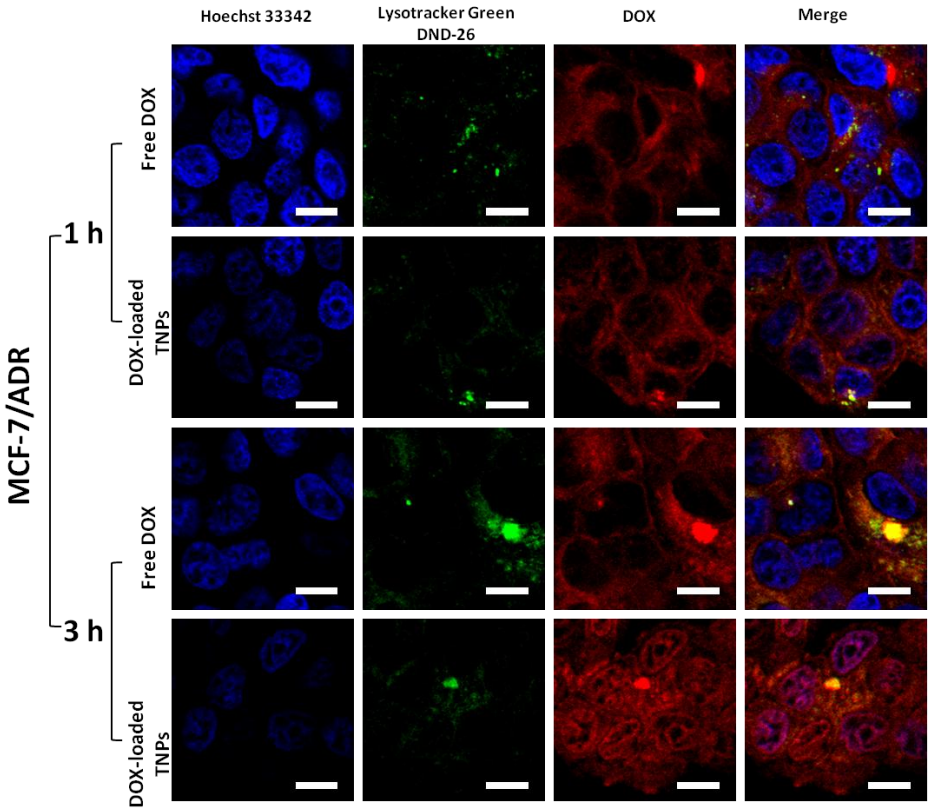

Figure 10 CLSM images of the intracellular distributions of the DOX-loaded TNPs and free DOX in MCF-7/ADR cells

CLSM images of the intracellular distributions of the DOX-loaded TNPs and free DOX with the same DOX concentration (10μM) in MCF-7/ADR cells for different time incubation (1 h and 3 h). The cells were stained with Lysotracker® green DND-26 (green) and Hoechst 33342 (blue). The pink color shows the localization of DOX (red) in nucleus (blue), and the yellow color indicates the localization of DOX (red) in endosomes/lysosomes (green). The scale bars represent 10 μm.

The TNPs were not possible to enter the nucleus due to size limitations for entry via the nuclear pore complex.[89] The results indicated that the TNPs could enhance the cellular uptake of DOX, and then affected its nuclear localization in both sensitive and resistant tumor cells. These observations demonstrated that the TNPs might be an effective nanocarrier to efficiently transport DOX into both sensitive and resistant tumor cells.

TNPs enhance in vitro cytotoxicity of DOX against sensitive and resistant tumor cells

Due to the enhanced intracellular DOX uptake by the TNPs in sensitive and resistant cell lines, we hypothesized that the TNPs could confer higher cytotoxicity against sensitive or even resistant tumor cells by enhancing intracellular delivery of drugs. To verify the hypothesis, we investigated the *in vitro* cytotoxic activity of the DOX-loaded TNPs against the sensitive cell lines and the resistant cell line for cancer therapy. First, it was determined that the TNPs had no cytotoxicity from 1.28 ng/ml to 100 μg/ml in the three cell lines after 48h treatment (**Figure 11A**). Different tumor cells were then treated with the DOX-loaded TNPs and free DOX at a series of DOX concentrations. **Figure 11B-D** shows the dose-dependent cell viability with the DOX-loaded TNPs and free DOX. The IC_{50} values for DOX-loaded TNPs and free DOX are listed in **Table 2**, indicating the enhancement of cytotoxic effect on DOX-loaded TNPs.

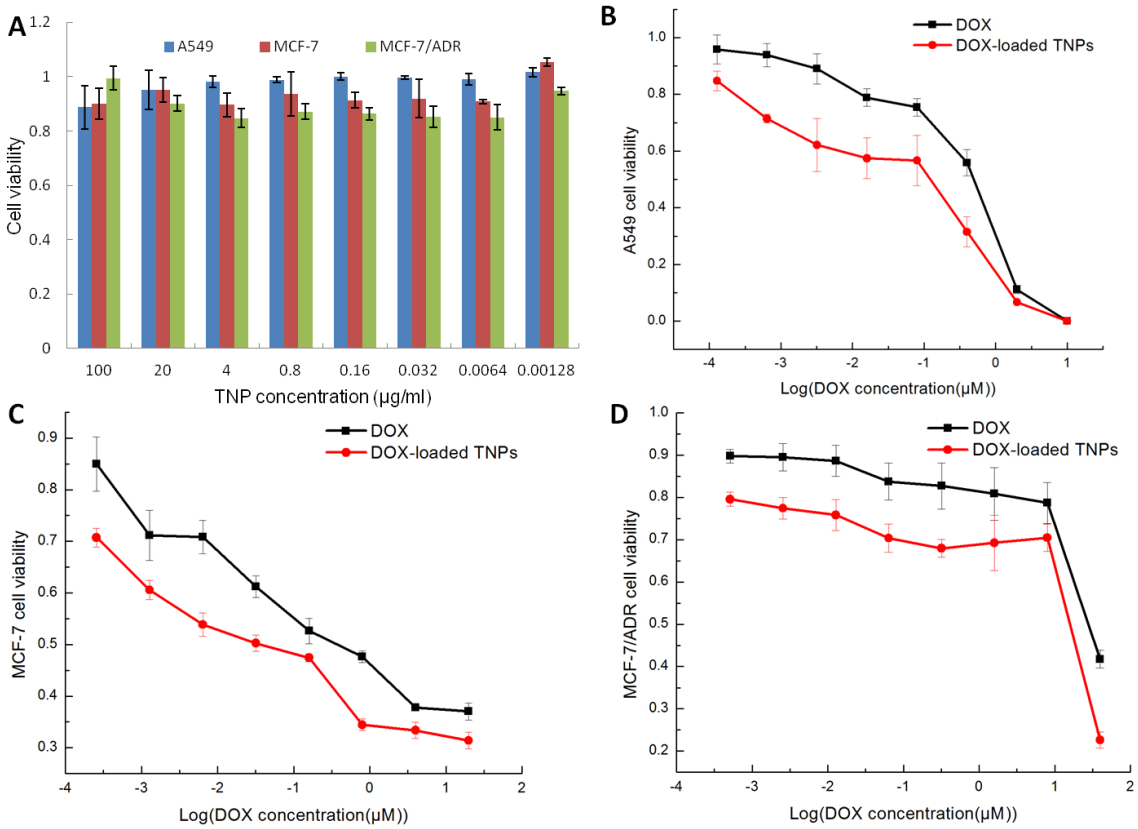

Figure 11 ***In vitro*** **cytotoxicity of the TNPs and DOX-loaded TNPs**

In vitro cytotoxicity of the TNPs (A) and the DOX-loaded TNPs in human lung cancer A549 (B), human breast cancer MCF-7 (C), and its drug resistant cell line MCF-7/ADR (D). All tumor cells were treated with the blank TNPs at the concentration of 1.28 ng/ml to100 μg/ml for cytotoxic test of the TNPs themselves. For the DOX-loaded TNPs and free DOX, the DOX dosage was from 0.1 nM to 10 μM (for A549 cells), from 0.3 nM to 20 μM (for MCF-7 cells), and from 0.5 nM to 40 μM (for MCF-7/ADR cells). The cells were treated with different samples for 48 h. Data are presented as the mean ± SD from three independent experiments.

Table 2 IC50 values (μM) of free DOX and the DOX-loaded TNPs in lung cancer A549 cells, human breast cancer MCF-7 and its drug-resistant cell line MCF-7/ADR after 48 h incubation.

IC_{50}(μM)	*A549*	*MCF-7*	*MCF-7/ADR*
DOX	0.30±0.05	0.46±0.09	69.69±21.67
DOX-loaded TNPs	0.026±0.005*	0.036±0.012*	15.16±7.05*

Note: IC_{50} was determined by using "Dose Resp" function of OriginPro 8.0; *P<0.05 as compared with free DOX.

Treatment of A549 cells with the DOX-loaded TNPs (from 0.64 nM to 10 µM) had significant higher cytotoxicity than the treatment with free DOX ($p<0.05$), with a half-maximal value of ~0.3µM (for free DOX) compared to ~0.026µM (for the DOX-loaded TNPs). Similarly, the IC_{50} value of the DOX-loaded TNPs (~0.036 µM) against MCF-7 cells was significantly lower than that of free DOX (~0.46 µM) ($p<0.05$), indicating much higher cytotoxicity of the DOX-loaded TNPs. In both cell lines, the IC_{50} value was ~12 times lower when associating of DOX with the TNPs (**Table 2**). More interestingly, in the case of resistant MCF-7/ADR cells, the IC_{50} value of the DOX-loaded TNPs was about 15.16 µM, which was 4.6 times lower than that of free DOX (69.69 µM) ($p<0.05$) (**Table 2**). The data indicated that the enhanced DOX uptake exerted by the TNPs could effectively increase the cytotoxicity against both sensitive and resistant tumor cells. The cytotoxicity data combined with the increased cellular uptake substantiate the use of the TNPs as a nanocarrier for the delivery of cancer therapeutics, especially for multidrug resistant tumors.

Further purification of the TNPs

It is well-known that the bioactivity of nature-based nanoparticles depends on their chemical characteristics. Thus, the verification of the components and their chemical structures in the TNPs is very important for the future biomedical applications. In this thesis, the TNPs were simply purified by using weak anion exchanger (WAX) and size exclusion chromatography (SEC). The TNPs were subjected to ion exchange chromatography on a 10×70 mm column of DEAE-cellulose. Different fractions were prepared in a stepwise elution with a series concentration of NaCl (0.1-1 M) solution, and with collection of 1 ml for each tube. The nanoparticles content in each fraction were determined by anthrone-sulphuric acid method [54]. The elution pattern plotted by the anthrone-sulfuric acid method suggested these fractions contained abundant polysaccharides. The fractions eluted with 0.2 M NaCl gradient, and then chromotographed on the Sephadex G75 in DI water, were designated TNP-D1 (**Figure 12 A**). Similarly, the fractions eluted with 0.3 M NaCl gradient, and then chromotographed on the Sephadex G75 in DI water, were designated TNP-D2 (**Figure 12 B**). These results suggested that TNP-D2 had the stronger negative charge owing to the elute solvent was the higher concentration of NaCl (0.3 M), while TNP-D1 had the weaker negative charge owing to the elute solvent at the lower concentration of NaCl (0.2 M).

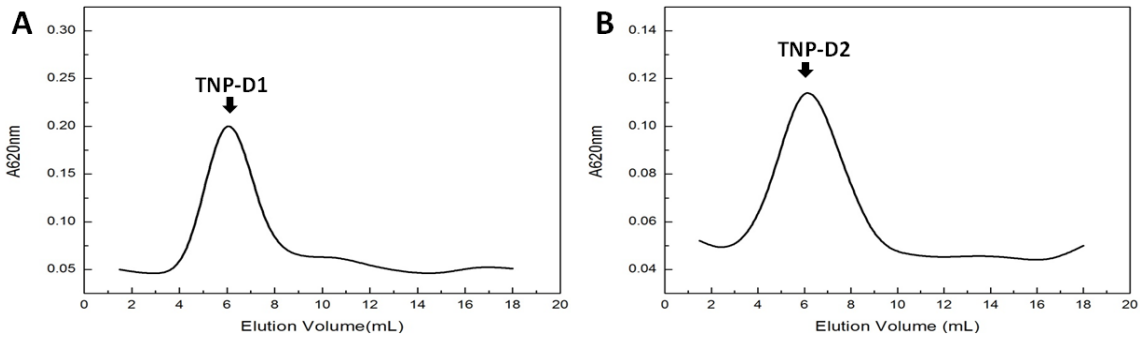

Figure 12 Elution profile of the isolated TNP-D on a DEAE-cellulose column (10×70mm). TNP-D1 was eluted with 0.2M NaCl and B) TNP-D2 was eluted with 0.3M NaCl.

.

The purified fractions were further characterized by AFM, DLS and ELS. As shown in **Figure 13**, all the purified fractions contained a large amount of spherical nanoparticles had similar particle size of 50-100 nm in diameters. The surface charge potential of the purified TNPs was analyzed using ELS, and the zeta potential of TNP-D2 was found to be -44.9 at pH 7.0, which was lower than those of TNP-D1 (-32 mV) (**Table 3**). These results further supported the elution profiles through the WAX column that the lower surface charges of TNP-D1 were easily eluted at lower concentration of NaCl solution (0.2M). In addition to the morphology, sizes and zeta potentials, it was found that neutral polysaccharides were considered to be the main components for TNP-D1, TNP-D2 fractions, which is similar to the TNPs. The presence of neutral polysaccharides was shown in TNPs, TNP-D1 and TNP-D2 by PAS staining after SDS-PAGE analysis (**Figure 13**). The quantitative data of polysaccharides and proteins in all samples were listed in Table 3. To further identify the functional groups in different TNP fractions, FTIR analysis was employed. As shown in **Figure 14**, the IR spectra of all samples exhibited the obvious characteristic absorption at 3600-3200 cm-1, 3000-2800 cm-1, 1400-1200 cm-1, 1200-1000 cm-1 corresponding to the existence of polysaccharides [90]. The absorption peaks at around 1650 and 1250 cm-1 indicated the existence of ring sugar [91]. The strong peak at around 3400 cm-1 was assigned to –OH stretching. The peaks at 1740 cm-1 and 1632 cm-1 were attributed to C-O stretching vibration of carbonylic group and N-H vibration or C=O asymmetric vibration of carboxyl group, which were also the characteristics of polysaccharides [90].

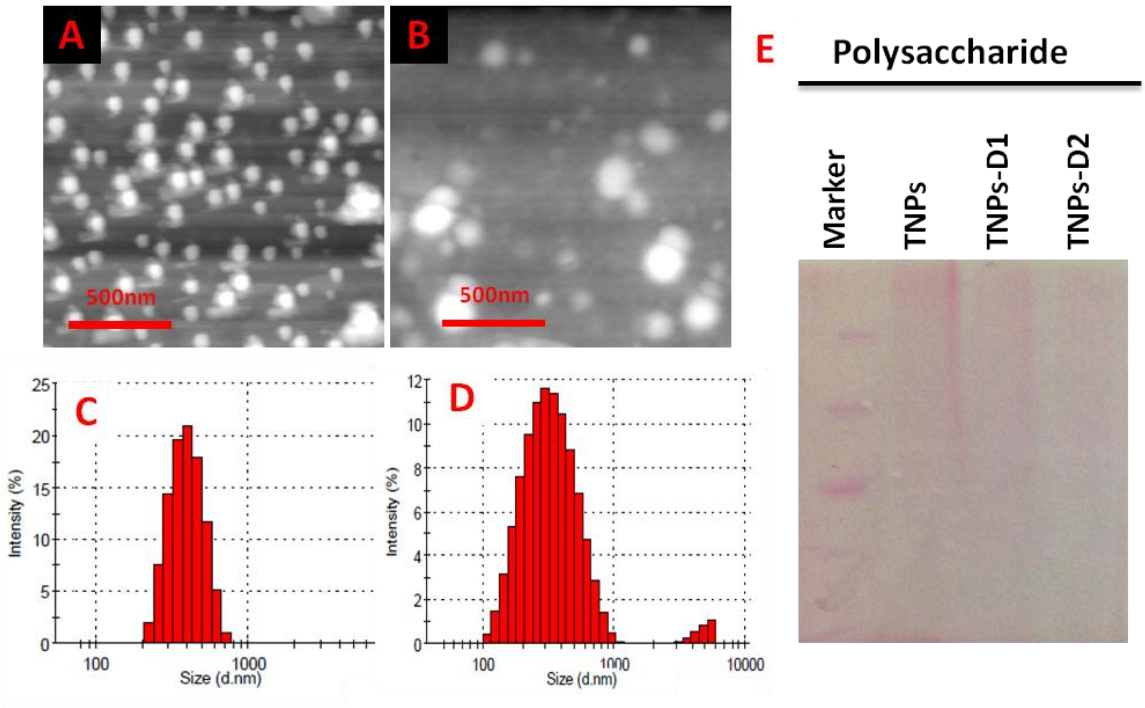

Figure 13 Characterization of purified TNPs

AFM images of purified TNPs: TNP-D1 (A), TNP-D2 (B). The size distribution of the purified TNPs: TNP-D1 (C), TNP-D2 (D) at pH=7.0 in suspension measured by DLS. (E) Analysis by SDS-PAGE of crude TNP samples: TNPs and purified TNP samples: TNP-D1 and TNP-D2. Samples were prepared in DI water and separated on 10% SDS-PAGE. Gel stained with PAS showed the neutral polysaccharides in all samples.

Table 3 Characterization of the purified TNPs via AEX and SEC procedures

Samples	TNP	TNP-D1	TNP-D2
Size(nm)	306.1	330.0	263.7
PDI	0.301	0.206	0.293
Zeta Potential (mV)	-32.5±2.4	-32±1.2	-44.9±0.7
Polysaccharide (mg/ml)	1.20±0.015	0.53±0.11	0.45±0.006
Protein (mg/ml)	0.67±0.005	0.05±0.004	0.03±0.001

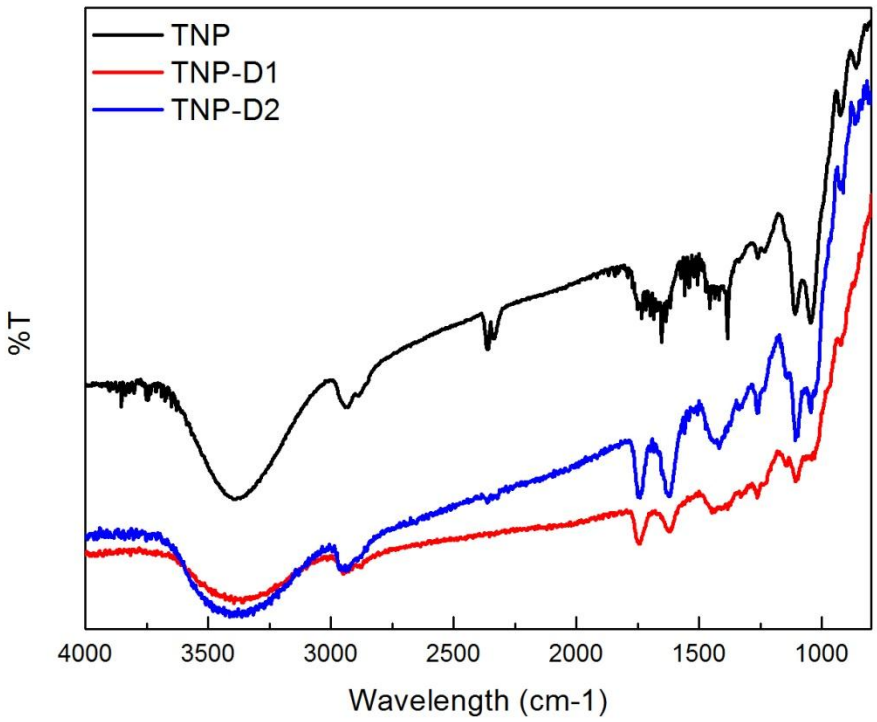

Figure 14 FTIR spectra of TNPs (Black), TNP-D1 (Red) and TNP-D2 (Blue) in the range of 4000-800 cm-1.

Conclusions

In this work, an infusion-dialysis based procedure for isolating organic nanoparticles from green tea was developed. Using this method, the TNPs isolated were spherical with diameters of 100-300 nm and a zeta potential of -26 mV at pH 7.0. Chemical analyses revealed that there were two macromolecules (polysaccharide and protein) and no small molecules (EGCG, caffeine and theobromine) were identified in the TNPs. It was determined that the TNPs had an immunostimulatory effect by inducing the secretion of various cytokines (IL-6, TNF-α, G-CSF) and chemokines (RANTES, IP-10, MDC) from RAW264.7 mouse macrophages. Further analysis showed that DOX could be effectively loaded onto the TNPs via electrostatic and hydrophobic interactions. More importantly, compared to free DOX, greater DOX uptake was observed for the DOX-loaded TNPs in sensitive tumor cells (A549 cells and MCF-7) and drug resistant tumor cells (MCF-7/ADR), all resulting in the enhanced cytotoxicity. Although the underlying mechanism of how the TNPs facilitate the DOX uptake in tumor cells and eventually lead to higher cytotoxic activity is still unknown; however, considering the immunostimulatory activity of the TNPs, this work provides a potential basis for utilizing the multifunctional nanoparticles from tea to improve antitumor efficacy in the cancer immunochemotherapy.

CHAPTER III
NATURALLY OCCURRING NANOPARTICLES FROM ARTHROBOTRYS OLIGOSPORA AS A MULTIFUNCTIONAL DRUG CARRIER FOR TUMOR IMMUNOCHEMOTHERAPY

Introduction

Cancer is a leading cause of death worldwide, accounting for 7.6 million deaths (around 13% of all deaths) in 2008, and the deaths are expected to continue rising, with an estimated 13.1 million in 2030 [92]. Chemotherapy is generally regarded as the first line approach for the treatment of malignant cancer in the past decades [93, 94]. However, conventional chemotherapy remains a daunting challenge to the successful treatment of metastatic tumors and becomes ineffective in many patients after first few treatments [95]. This might be due to the tumor heterogeneity, plasticity, and ineffective drug delivery to tumor tissues and cells, which enable a subgroup of cancer cells to mutate and evade the chemotherapy [96-98]. Simply increasing drug dose does not guarantee elimination of this subset of tumor cells, but would eventually lead to systemic toxicity in normal tissues and high frequency multi-drug resistance in tumor cells [95, 99].

To evade the emergence of the systemic toxicity and therapy resistance, it is critical to design a treatment modality with multiple mechanisms of cell killing in tumors. One such therapy is the combined immuno-chemo-therapeutic regimen, which has demonstrated great potential in maximizing the clinical outcomes of cancer patient due to synergistic antitumor effects between chemotherapy and immunotherapy [100]. Different clinical trials incorporating cancer vaccines, immune checkpoint blockade, or adoptive cellular therapy have typically tested the immunotherapies integrated with standard-dose chemotherapy [101]. Current clinical data suggest that combined immunochemotherapy regimens are not only

drug dependent but also dependent on drug dose, timing and schedule in related to immune-based intervention [100, 101]. Because of the aforementioned strategy conditionally dependent synergism between chemotherapy and immunotherapy, it is expected that developing rational carriers that could incorporate and simultaneously deliver both immune-stimulating and cytotoxic chemotherapeutic agents [102] may be facilitate the precise temporal and spatial delivery of different therapeutics. From this perspective, a few combination therapies using engineered nanoparticle-based delivery systems, including nanoparticles [102, 103], liposomes [104-106] and macromolecular conjugates [98], etc, in conjunction with different chemical drugs and immune-stimulants, have been reported for chemoimmunotherapy in various cancers, providing promising preclinical outcomes[107]. However, among these nanoparticle-enhanced combinatorial immunochemotherapies, few engineered biomaterials themselves have been used as immunostimulants or adjuvants. They are generally inert biomaterials, simply conjugated or encapsulated with an immunostimulatory agent and a chemo-drug for the use of the combined antitumor therapy. Due to the complex pathogenesis of malignancy, which juxtaposes intrinsic aberrations in tumor cells with profound effects on the host innate and acquired immune system, it demands a multi-functional therapeutic strategy that targets tumor cells and improves or reestablishes antitumor immune responses [108]. Thus, future rational immunochemotherapies call for novel therapeutic biomaterials with multi-functional modes of action, in conjunction with

conventional chemo-drugs, to establish the utility and feasibility of immunochemotherapy [108].

Naturally occurring nanoparticle is an alternative source for production of biopolymer-based nanoparticles with diverse properties and biofunctions through different biological systems. The use of naturally occurring organic nanoparticles and their biomimetic/bioinspired nanomaterials in biomedical and industry fields have recently drawn significant interest from scientific communities. In previous study, our group first discovered that the adventitious roots of English ivy secreted organic nanoparticles and demonstrated that they were an attractive candidate for sunscreen fillers [23]. Similar organic nanostructures have been discovered in the secretions of a variety of marine species, including polychaetes, mussels, barnacles, and sea stars [109-113] and their potential applications in diverse industry fields were also explored and discussed [25]. It is anticipated that the study on naturally occurring nanoparticles will not only help us to understand the roles of nanoparticles in biological systems, but also provide insight into the development of these nanomaterials for novel treatment of diseases. As a natural counterpart of engineered nanoparticles, naturally occurring organic nanoparticles, with multi-pronged modes of action in the context of cancer therapy, may be approached in the same way as other engineered inert nanoparticles that have been used for the aforementioned combined immunochemotherapy, producing improved immune responses. In

2012, our group has first revealed that the secreted nanoparticles from a carnivorous fungus, *Arthrobotrys oligospora,* had promising properties as an immunostimulatory and antitumor agent for cancer treatment [114]. *A. oligospora* is a representative flesh eater in the fungal kingdom, and it can develop into the specialized 3D adhesive traps for capturing, penetrating and digesting free-living nematodes in diverse environments [115]. The natural-based nanoparticles from *A. oligospora*, designated as fungal nanoparticles (FNPs) in this study, had mild cytotoxic activity in tumor cells, induced the secretion of tumor necrotic factor (TNF-α) from macrophage, and could be simultaneously used as a drug carries for chemical drug delivery into the tumor cells [114]. Therefore, the novel therapeutic bionanomaterial from this carnivorous fungus would be a new multifunctional modality for optimal cancer treatment by simultaneously modulating immune system, direct killing antitumor cells and delivery chemo-drug into tumor cells and tissues.

The purpose of this study was to further evaluate the immunostimulatory activity, dissect the mechanism of the cytotoxicity, and explore the potential in cancer immunochemotherapy using the FNPs as a multifunctional nanocarrier *in vitro*. We have established a cost-effective and robust platform to produce and collect the FNPs from the sitting drop culture system established in our lab. The FNPs collected by a washing-dialysis procedure in our previous study showed a size of 200-300 nm in diameters measured by SEM/AFM, and even 300-400 nm in

aqueous solution measured by DLS analysis [114]. From the perspective of mere passive targeting tumor *in vivo*, the upper bound size for nanoparticles participating in the enhanced permeability and retention (EPR) effect is believed to be approximately 400 nm[116], and an effective drug carrier for *in vivo* cancer treatment should have a diameter less than 200nm considering the multiple factors *in vivo*, such as limited fenestration size of the leaky vasculature in tumors and rapid systemic clearance [99]. Thus, in this study, we first established a new approach for purification of the crude FNPs collected from the sitting drop culture system in order to obtain the purified FNPs with proper size ranges, followed by characterization of critical physical-chemical properties of the purified FNPs. The purified FNPs used as a novel multifunctional nanocarrier for cancer immunochemotherapy *in vitro* was investigated, including immunostimulation, the mechanism of the cytotoxicity, synergistic cytotoxicity, drug delivery into tumor cells and combined immunochemotherapeutic effect. Here we report a novel immunochemotherapy approach based on the multifunctional fungal nanoparticles, which may open a new avenue for combined cancer immunochemotherapy in the future.

Materials and Methods

Chemicals, fungus and cell lines

Arthrobotrys oligospora (ATCC 24927), A549 human non-small-cell lung cancer cells (CCL-185) and RAW 264.7 murine macrophages (TIB-71) were obtained from the American Type Culture Collection (Manassas, VA). B16BL6 murine melanoma cells, MCF-7 human breast tumor cell line and its resistant cell line MCF-7/ADR were obtained from the National Cancer Institute-Central Repository (Frederick, MD). Splenocytes, derived from C57BL/6 mice, were purchased from the Allcells Company (Emeryville, CA). HEPES, 1, 9-dimethyl-methylene blue (DMMB), chondroitin sulfate (CS), Sephadex G75, DEAE-cellulose and phosphate buffered saline (PBS) were purchased from Sigma-Aldrich (St. Louis, MO). Doxorubicin hydrochloride (DOX) was purchased from Abcam (Combridge, MA). LysoTracker Green DND-26 and Hoechst 33342 were purchased from Invitrogen Life Technologies (Grand Island, NY). Fetal bovine serum, DMEM medium and RPMI 1640 medium were purchased from Mediatech (Manassas, VA). Penicillin (10000 units/ml)-streptomycin (10000 μg/ml) solution was obtained from MP biomedicals (Solon, OH).

Arthrobotrys oligospora culture and purification of FNPs

A. oligospora was cultured in the sitting drop culture system as the previously study [114] with minor modifications. Briefly, conidia suspension (about 1000-2000 conidia in 200 μl) was inoculated into the media droplet and incubated at 25˚C for 7 days. The isolation procedures were shown in **Figure 15A**.

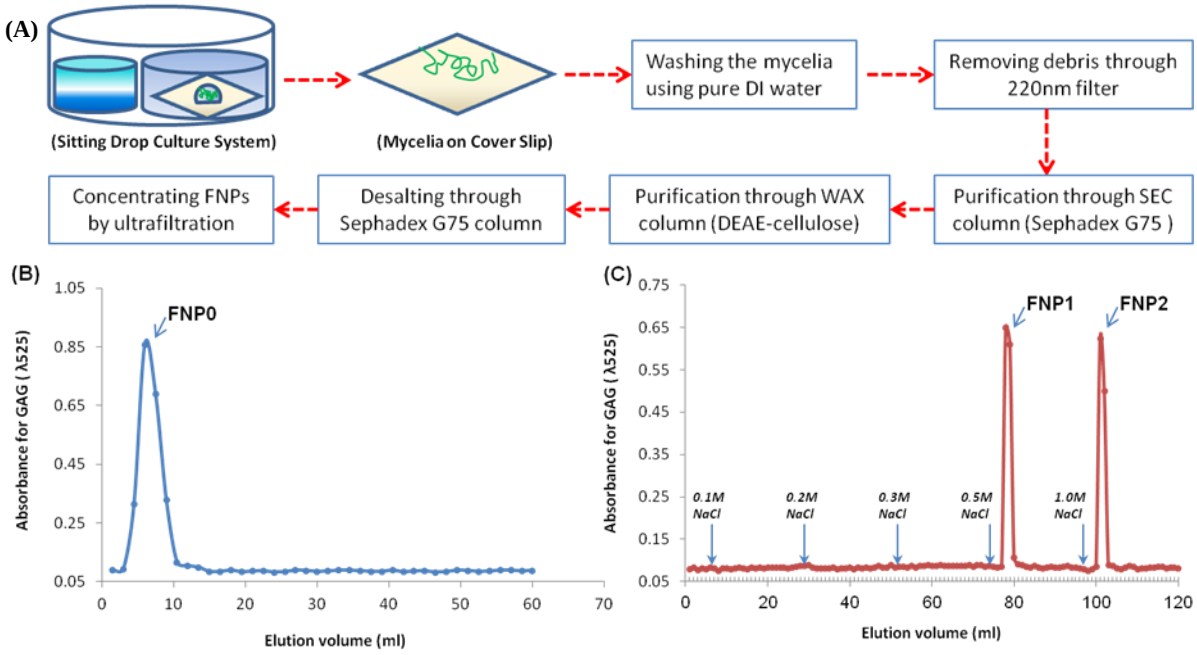

Figure 15 Schematic of a new isolation method, SEC-WAX-SEC procedure

For the FNP purification (A), and the elution profiles of the FNPs-containing media collected by washing mycelia in the sitting drop culture system using a size exclusion chromatography (SEC, Sephadex G75, 15 mm×70 mm) column (B) and a weak anion exchange (WAX, DEAE-cellulose, 10mm×70mm) column (C). The FNPs isolated from SEC column was designated as FNP0, which is a crude nanoparticle sample. After loading FNP0 into the WAX column, two FNP fractions eluted from 0.5M NaCl and 1.0M NaCl were designated as the FNP1 and FNP2, respectively. The FNPs were qualitatively determined by colorimetrically measuring the absorbance (λ525) of glycosaminoglycan (GAG) in the FNPs (M&M Section 2.2).

First, the mycelia developed on the cover slip were washed more than 10 times using distilled water. The wash water containing nanoparticles was collected, and the samples were then filtered through a 0.2 μm syringe filter (cellulose acetate, VWR, Radnor, PA). The FNPs were desalted by a Sephadex G75 column as reported previously [56]. The desalted FNPs is designated FNP0, which is a crude sample. To purify the FNP0, weak anion-exchange (WAX) chromatography on DEAE-cellulose was performed as described previously [117]. The DEAE-cellulose columns were then eluted in a stepwise fashion with 0.1 M, 0.2 M, 0.3 M, 0.5 M and 1.0 M NaCl. As our previous study, glycosaminoglycan (GAG) is one of the main components in the FNPs [114]. Thus, the colorimetric assay (λ525nm) for GAG with 1, 9-dimethyl-methylene blue was used to monitor the FNPs in the eluent from the DEAE-cellulose column. The elution profiles of the FNPs, reflected from GAG concentration, were plotted versus elution volumes. The collected peaks containing FNPs from WAX column were subjected to the Sephadex G-75 column for desalting, and the desalted FNPs were concentrated to final volume of 150μl using a centrifugal filter tube (Amicon Ultra-15 100K, Merck Millipore, Ireland).

Characterization of FNPs

To characterize morphology and particle size of the FNPs, the samples were analyzed using AFM (MFP-3D, Asylum Research, Santa Barbara, CA). Briefly, 10μl of the particle solution was air-dried on a glass cover slip, and analyzed in AC mode based on the software Igor Pro from Wavemetrics and an ACTA Probe

from AppNano (Santa Clara, CA) at room temperature. The nanoparticle samples were further analyzed by dynamic light scattering (DLS) and electrophoretic light scattering (ELS), using a Zetasizer Nano (Malvern Instruments Ltd, Worcestershine, UK), to determine the size distribution and zeta potential of the samples in solution. To qualitatively determine the chemical components in the nanoparticles, SDS-PAGE was used for staining the GAG and neutral polysaccharides in the nanoparticles using Alsian blue and PAS reagents (Thermo Scientific, MI), respectively. To quantitatively determine the chemical components in the nanoparticle samples, the total amounts of polysaccharides were measured using the anthrone-sulfuric acid assay [54]. The amount of GAG in each sample was determined by a Proteoglycan Detection Kit (1, 9-dimethylmethylene blue, Astarte Biologics, Redmond, WA) [114], and the uronic acid in the nanoparticles were determine using carbozole assay [118]. Meanwhile, the concentration of protein in the samples was quantitatively determined by the BCA protein assay (Pierce, Rockford, IL) following the manufacturer's instructions. In addition, the endotoxin concentration in the nanoparticle samples was measured by using the ToxinSensor Chromogenic LAL Endotoxin Assay Kit (GenScript, Piscataway, NJ) following the manufacturer's instructions.

Immunostimulatory activity

The mouse macrophage RAW 264.7 cells and splenocytes derived from C57BL/6 mice were cultured in DMEM and RPMI 1640 culture media, respectively. Both media were supplemented with 10% FBS and 1% penicillin-

streptomycin at 37°C in 5% CO_2. The cells were plated in 12-well plates at a density of 5×10^6 cells/ml, treated with the FNPs at the GAG concentration of 5μg/ml. After a 24-h incubation, the supernatants were collected for ELISArray analysis. Mouse common cytokines and chemokines multi-analyte ELISArray kits (SABiosciences Corporation, Frederick, MD) were used to determine 12 cytokines (IL-1A, IL-1B, IL-2, IL-4, IL-6, IL-10, IL-12, IL-17A, IFN-γ, TNF-α, G-CSF, and GM-CSF) and 12 chemokines (RANTES, MCP-1, MIP-1a, MIP-1b, SDF-1, IP-10, MIG, Eotaxin, TARC, MDC, KC, and 6Ckine) in the supernatants following the manufacturer's instructions. The concentration of nitric oxide (NO) in the supernatants of both cells treated with the FNP samples were also determined using Griess assay, as described elsewhere [119].

MTT assay

The cytotoxicity of the purified FNP samples and the DOX-FNP complexes against four cancer cell lines (A549, B16BL6, MCF-7 and MCF-7/ADR cells) was evaluated by MTT assay as early described [56], and the biocompatibility of the purified FNP samples toward mouse fibroblast NIH3T3 cell was also measured with MTT assay[120]. Briefly, 8000-10000 cells were plated in 96-well plates in 100 μl culture media per well and incubated at 37 °C in 5% CO_2 for 24 h to allow the cells to attach. Specifically, DMEM were used for A549 and B16BL6 cells, RPMI 1640 for MCF-7 and MCF-7/ADR cells and DMEM-α for MIH3T3 cells. The media were supplemented with 10% fetal bovine serum (for tumor cells) or calf serum (only for NIH3T3), and 1.0 % penicillin-streptomycin. The cells were then

treated with different concentrations of the FNPs or the DOX-FNP complexes. After a 48-h treatment, 10 µl of MTT solution (5 mg/ml in PBS, pH 7.4) was then added to each well and the plates were incubated for another 4 h. The cell culture media were removed and replaced with 100 µl DMSO. The absorbance was measured by a microplate reader (Bio-Tek µQuant) at 570 nm. For the DOX-FNP complexes, the average IC_{50} value (the dose having 50% cell inhibition) was determined by cell survival plots using the "DoseResp" function in OriginPro 8.0.

Apoptotic assay

The apoptosis study was determined by evaluating DNA ladder formation [121]. Briefly, A549 cells and B16BL6 cells were treated with the FNP samples at the GAG concentration of 10µg/ml, and then incubated at 37 °C in 5% CO2 for 48h. Apoptotic cells were identified by TdT-mediated dUTP nick and labeling (TUNEL) assay using APO-BrdUTM TUNEL Assay Kit (Invitrogen, Eugene, OR) according to the manufacturer's instructions. The cells were then analyzed using flow cytometry (Epics XL Analyzer, Beckman Coulter Inc., Brea, CA) by collecting 20000 events for each sample and measuring the cell associated fluorescence.

Cell cycle analysis

To determine cell cycle distribution, A459 and B16BL6 cells were passed into 24-well plates and treated with the FNP samples at the GAG concentration of 10µg/ml, and then incubated at 37°C in 5% CO2 for 24h. The cells were then trypsinized, washed with PBS, and fixed in 75% ethanol at 4°C for 2 h. The fixed

cells were stained with propidium iodide/RNase A staining buffer (Invitrogen, Eugene, OR) at 37˚C for 30 min in the dark. The cell cycle analysis was conducted using flow cytometry (Epics XL Analyzer, Beckman Coulter Inc., Brea, CA) by collecting 20000 events for each sample and measuring the cell associated fluorescence.

Formation of DOX-FNP complexes

To prepare the complexes between DOX and the FNPs, 60µl of DOX (3mM) was added into 110µl of the FNP1 (~143 µg/ml GAG) or 160µl of the FNP2 (~95µg/ml) in 20mM HEPES buffer at pH 7.0, and then incubated at room temperature overnight. The precipitates between DOX and the FNPs were then centrifuged at 10,000 rpm for 10 min. The precipitates were dispersed in 500µl PBS buffer, and then sonicated for 10min in a bath sonicator (Aquasonic 7500, VWR). The amount of DOX in the dispersed precipitates was quantified by measuring UV absorbance at 480nm and the entrapment ratios of DOX in the complexes were calculated as previously reported [56]. To determine the stability of DOX in the complexes in the PBS buffer, the dispersed complexes were applied to Sephadex G75 column. The first peak, standing for the stable complexes, and the second peak, standing for free DOX, was collected for quantification. The morphology, particle size and zeta potential of the DOX-FNP complexes were characterized using AFM, DLS and ELS analysis, as above described.

In vitro release study

DOX release from the DOX-FNP complexes was studied at different pH values. 150μl of the DOX-FNP1 complexes (168μM for DOX), 200μl of DOX-FNP2 complexes (~126μM for DOX), or 84μl of free DOX (300μM) were placed in a dialysis tube (MWCO 300 K, Spectra/por membrane tubing, Spectrum Labs, CA), and then immersed in tubes containing 6 ml of release buffers at different pH values (1 × PBS, pH 7.4; 0.1 M acetic acid buffer, pH 5.5). All tubes were incubated at 37˚C under mild agitation. The dialysate sample (0.5 ml) was collected at different time points and replenished immediately with the same volume of the fresh medium. The concentration of DOX in the dialysate was analyzed fluorometrically at λex480 nm and λem590 nm, and the cumulative release profiles were plotted verse release times.

Cellular uptake and confocal microscopic study

The quantification of intracellular DOX uptake in cancer cells was evaluated by flow cytometry. A549 and B16BL6 cells were cultured in 6-well plates at densities of 1×106 cells/ml, and incubated at 37°C in 5% CO2. The DOX-FNP complexes at the DOX concentration of 10μM were added into each well, and free DOX was used as a control. After a 4-h incubation, the media were aspirated. The cell monolayer was rinsed with PBS for three times, and then trypsinized. Flow cytometry analysis was carried out on an Epics XL Analyzer (Beckman Coulter Inc., Brea, CA) by collecting 20000 events for each sample.

Confocal laser scanning microscopy (FluoView FV1000 Confocal Microscope, Olympus, Japan) was used to investigate intracellular DOX distribution in tumor cells treated with the DOX-FNP complexes. Briefly, the cells were seeded on cover slips with a density of 106 cells/ml in 6-well plates and cultured at 37°C in 5% CO2 for 24 h. The cells were then treated with the DOX-FNP complexes at the DOX concentration of 10 μM for 4h. Free DOX was used as a control. To observe the intracellular distribution, endolysosome- and nuclear-specific markers, LysoTracker® green (100 nm) and Hoechst 33342 (4μM), were incubated with the cells for 30 min prior to the confocal imaging. After that, the cover slip was washed with PBS three times, set on a microscope slide, and then examined by confocal microscopy.

To observe the internalization of the FNPs themselves, the FNPs were first labeled with FITC. For such a purpose, 3.5mg/ml of FITC in DMSO was diluted to 0.7mg/ml with 100 mM carbonate buffer (pH 9.3), and then 150μl of the FNP1 (138.56μg/ml) and FNP2 (56.83μg/ml) were added into 400μl of the above carbonate buffer. After a 24-h incubation at the room temperature, resulting solution was dialysized (MWCO 300 K, Spectra/por membrane tubing, Spectrum Labs, CA) against PBS buffer for three days. After that, the cells were treated with the FITC-labeled FNPs at the FITC concentration of 2ng/ml, and the internalization of the FNPs was then imaged with confocal microscopy as above detailed.

Co-culture system for testing immunochemotherapeutic activity

A co-culture system using B16BL6 tumor cells and the splenocytes derived from C57BL/6 mice was used to evaluate the immunotherapeutic effect of the DOX-FNP complexes in vitro [98, 103]. Briefly, 2×10^5 tumor cells, labeled with 5 μM CFSE, were co-cultured with 5 x106 splenocytes, and then the co-cultures were treated with free DOX and both DOX-FNP complexes at the DOX concentration of 1μM. After a 24-h incubation, the death of tumor cells was determined by the PI uptake method using flow cytometer after gating on the CFSE labeled cancer cells.

Statistical analysis

All the values were presented as mean ± standard deviation (S.D.) of at least three independent measurements. Statistical significance was tested by one-way ANOVA followed by a Student's t test for multiple comparison tests. A p value of <0.05 was considered statistically significant.

Results and Discussion

Purification and characterization of FNPs

The sitting drop culture system for the fungus A. oligospora has been established in our lab, from which the secreted FNPs was isolated and characterized [114]. Using a dialysis procedure, these crude isolates of the FNPs demonstrated a spheroidal shape with diameter of 100-500 nm [114]. In this study, we established a new purification procedure using a combination of size exclusion chromatography (SEC) and weak anion exchanger (WAX) to purify the FNPs. As shown in **Figure 15A**, after inoculation of at least 1000 conidia per cover slip on which about 500µl of media drop was added, the fungal mycelia were grown for 7 days and the mycelia thrived on the cover slip were washed using distilled water. The collected wash media were then filtered to remove any debris, and then applied to Sephadex G75 column. Through the SEC column, the first peak, designated as FNP0, was collected (**Figure 15B**), and characterized using AFM. As shown in **Figure 16A-B**, spheroidal nanoparticles with 100-300nm in diameter were observed. The nanoparticle FNP0 was further analyzed with DSL and ESL, showing average size of ~300nm (**Figure 16C**) and negative zeta potential of ~30 mV (**Table 4**). These crude isolates of FNPs were further applied to DEAE-cellulose column, leading to production of two FNP fractions that were eluted respectively using 0.5M NaCl and 1.0M NaCl (**Figure 15C**). Both FNP fractions, designated respectively as FNP1 and FNP2, were further characterized for their morphology, hydrodynamic size and zeta potential using AFM, DLS and ELS.

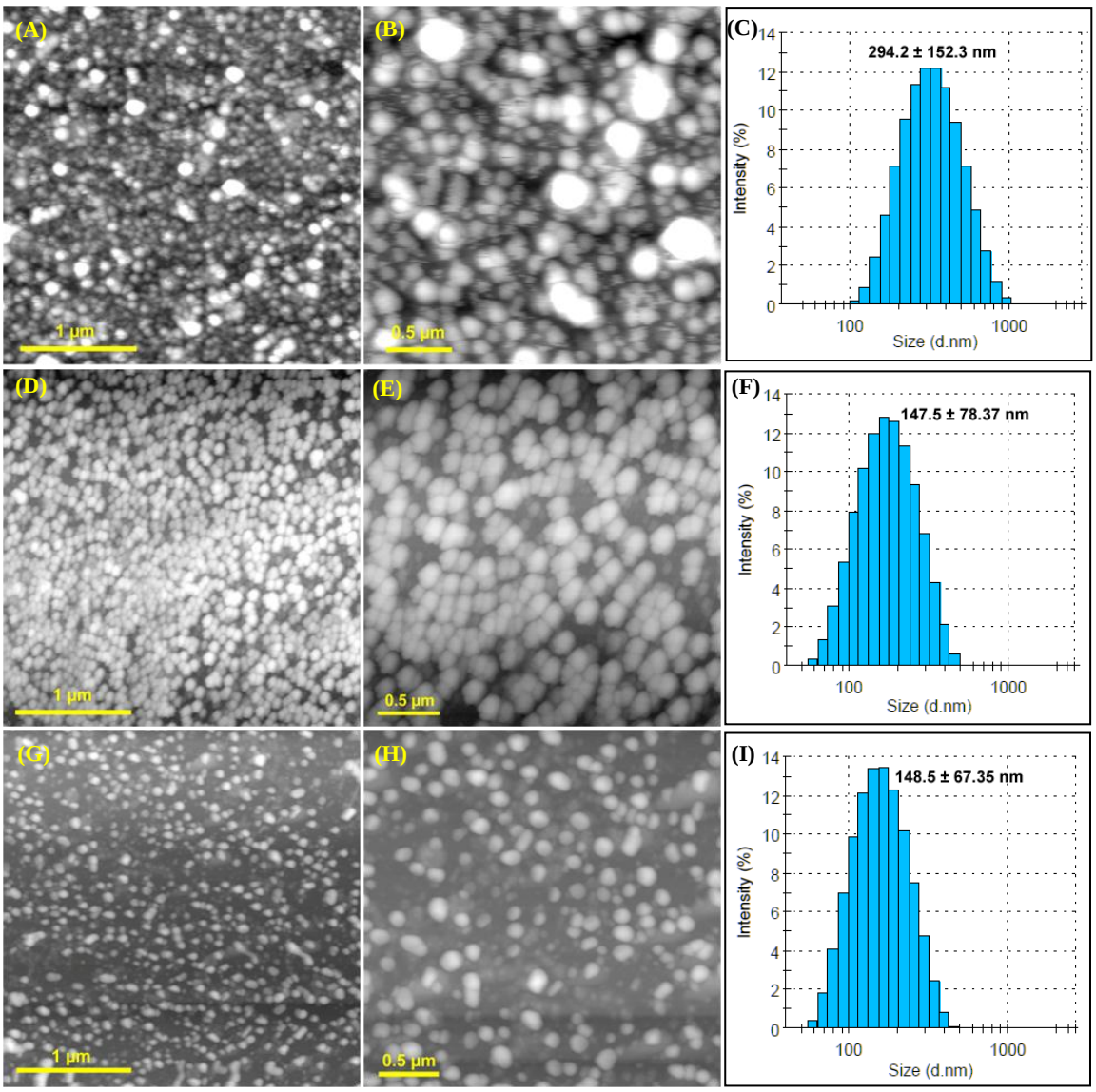

Figure 16 AFM images (A-B, D-E and G-H) and size distribution (C, F and I) of the FNPs prepared with the SEC-WAX-SEC procedure.

(A-C) The nanoparticle FNP0, prepared with only SEC procedure (Sephadex G75 column); (D-F) The nanoparticle FNP1, prepared with the SEC-WAX-SEC procedure and eluted with 0.5M NaCl; (G-H) The nanoparticle FNP2, prepared with the SEC-WAX-SEC procedure and eluted with 1.0M NaCl.

Table 4 Physicochemical characterization of the FNPs prepared with the SEC-WAX-SEC procedure

	Size (nm)	Zeta potential (mV)	Protein (µg/ml*)	GAG (µg/ml*)	Uronic acid (µg/ml*)	Total Sugar (µg/ml*)
FNP0	294.2 ± 152.3	-30.7 ± 9.1	661.1 ±10.7	187.6 ±10.7	162.6±23.1	410.1±6.4
FNP1	147.5 ± 78.4	-26.9 ± 6.9	86.8 ±6.3	296.5 ±38.1	153.9±10.8	506.2±25.2
FNP2	148.5 ± 67.4	-32.1 ± 7.6	3.7 ±0.7	98.7 ±7.4	40.4±7.7	162.7±8.5

Note: * The concentrations of protein, glycosaminoglycan (GAG), uronic acid and total sugar in the FNPs were determined after they were concentrated to 150 µl using a spin filter (M&M Section 2.2&2.3). Therefore, the unit here is designated as µg/ml nanoparticle solution instead of µg/mg freeze-dried nanoparticles. All concentrations were based on the following preparation methods: the FNP0 was prepared using one batch of fungal culture (40 small disks), and the purified FNP1 and FNP2 were prepared using three batches of fungal culture (120 small disks).

As shown in **Figure 16 D-F**, the first peak (FNP1), eluted from 0.5M NaCl, were spheroidal nanoparticles with ~150nm in hydrodynamic diameter. The second peak, FNP2, had similar hydrodynamic size with spheroidal morphology (**Figure 16 G-I**). However, as shown in Table 1, the FNP1 had zeta potential of ~ -27 mV, which is lower than that of FNP2 (~ -32mV). The difference in zeta potentials for both FNP fractions is consistent with their elution profiles through the WAX column. Due to relatively lower surface charge of the FNP1 fraction, it was eluted more easily at low concentration of NaCl than FNP2 fraction [117] (**Figure 15 C**). Therefore, at low salt concentration, i.e. 0.5M NaCl, the FNP1 was first eluted, and then the FNP2 was selectively eluted at higher concentration, i.e. 1.0M NaCl.

Apart from the differences in morphology, sizes and zeta potentials, FNP1 and FNP2 had chemical components as similar as the crude FNP0. As shown in **Figure 17 A-B**, glycosaminoglycan (GAG) and neutral polysaccharides were demonstrated to be the major components for both FNP1 and FNP2 fractions, which is similar to the crude FNP0 sample. The quantitative data for GAG, uronic acid and total sugars in the three FNPs are listed in **Table 4**. For the protein component in the three FNP samples, the ratio of protein to total sugar in the FNP0 was much higher than those in the TNP1 and TNP2 (**Table 4**), indicating most proteins in the crude FNP0 were free and unbound proteins. These proteins were not bound to FNPs, leading to complete washing away through the purification procedure with lower salt concentration (< 0.5M NaCl). Therefore, compared to the amount of total sugar, the purified FNP1 and FNP2 only had lower ratios of proteins to total sugars in the nanoparticles.

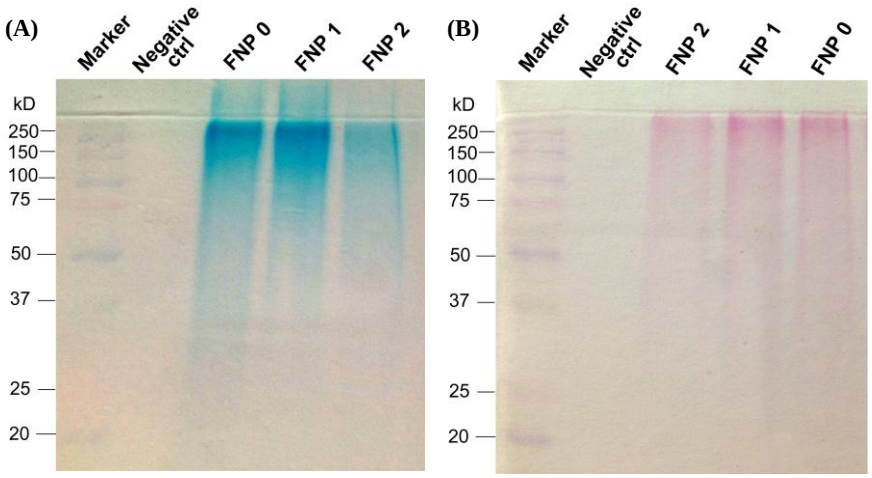

Figure 17 SDS-PAGE analyses of polysaccharides in the FNPs by using Alcian blue staining (A) and PAS staining (B).

Alcian blue were used for glycosaminoglycan (GAG) staining and PAS for neutral polysaccharide staining.

Due to most GAGs covalently attaching to core proteins to form proteoglycan [122], we presume that some proteins probably were bound to the GAGs in the nanoparticles. On the other hand, two protein bands were observed in the FNP sample prepared using dialysis method in our previous report [114] and the protein bands with similar MW were also observed in the FNP0 samples in this study. For the purified FNP1 and FNP2, both similar protein bands with relatively weaker intensities were also appeared in the SDS-PAGE analysis (Data not shown). No matter how the proteins are chemically bound to or physically associated with the FNPs, the polysaccharides, including acidic GAG and neutral polysaccharides, are main chemical components in the purified FNPs.

FNPs stimulate secretion of multiple proinflammatory cytokines and chemokines from macrophage and splenocytes

In our previous study, it has been demonstrated that the FNPs prepared using a dialysis approach induced the secretion of TNF-α from a macrophage cell line RAW264.7 in a dose-dependent manner [114], indicating the potential of antitumor immunity using the FNPs. In this work, after obtaining the purified FNPs, FNP1 and FNP2, macrophage stimulatory activity was first studied using the cultured mouse macrophage RAW 264.7 as a cell model. As shown in **Figure 18A**, after a 24-h incubation of the FNP-treated macrophage RAW264.7 at the GAG concentration of 5μg/ml, ELISArray demonstrated significantly elevated levels of IL6, TNF-α, and G-CSF from the macrophage treated by the three FNP

samples, FNP0, FNP1 and FNP2, as compared to the untreated cells. Of the panel of 12 cytokines assayed, except for above three cytokines, low but statistically significant increases in IL1α and IL17A were also detected for the FNP1 and FNP2 in the supernatant of the treated macrophage, respectively. As is well known, TNF-α is a Th1-biased cytokine as a potential anticancer agent for many years [123], playing a key role in apoptosis, cell survival, inflammation and immunity [69]. It has been demonstrated that TNF-α was critical for antitumor T cell immunity in mice [124] and could act synergistically with other drugs at the molecular level to trigger the apoptosis and dissociation of tumor vascular endothelial cells in cancer treatment [70, 71]. As a Th2-biased cytokine, IL-6 plays key roles in T-cell-mediated immune responses, acting as a cofactor for T-cell proliferation [73], and as a growth inhibiting factor, the antitumor effects of IL-6 on multiple murine tumor in vivo has been reported [125-127]. G-CSF can enhance the differentiation of stem cells in bone marrow, facilitate the mobilization of hematopoietic precursor cells into the bloodstream [75],and accelerate recovery from chemotherapy-induced myelosuppression [128]. The synergistic antitumor effect of TNF-α and G-CSF has been established and antitumor effect of TNF was enhanced by combination with G-CSF in multiple tumors *in vivo* [129]. As such, we presume that significant higher amount of TNF-α, IL-6 and G-CSF secreted from the treated macrophages will be benefit for adjuvant anticancer therapy using the FNPs. FNP0, FNP1 and FNP2, as compared to the untreated cells. Of the panel of 12 cytokines assayed, except for above three cytokines, low but statistically significant increases in IL1α and IL17A

were also detected for the FNP1 and FNP2 in the supernatant of the treated macrophage, respectively. As is well known, TNF-α is a Th1-biased cytokine as a potential anticancer agent for many years [123], playing a key role in apoptosis, cell survival, inflammation and immunity [69]. It has been demonstrated that TNF-α was critical for antitumor T cell immunity in mice [124] and could act synergistically with other drugs at the molecular level to trigger the apoptosis and dissociation of tumor vascular endothelial cells in cancer treatment [70, 71]. As a Th2-biased cytokine, IL-6 plays key roles in T-cell-mediated immune responses, acting as a cofactor for T-cell proliferation [73], and as a growth inhibiting factor, the antitumor effects of IL-6 on multiple murine tumor in vivo has been reported [125-127]. G-CSF can enhance the differentiation of stem cells in bone marrow, facilitate the mobilization of hematopoietic precursor cells into the bloodstream [75], and accelerate recovery from chemotherapy-induced myelosuppression [128]. The synergistic antitumor effect of TNF-α and G-CSF has been established and antitumor effect of TNF was enhanced by combination with G-CSF in multiple tumors *in vivo* [129]. As such, we presume that significant higher amount of TNF-α, IL-6 and G-CSF secreted from the treated macrophages will be benefit for adjuvant anticancer therapy using the FNPs. To confirm this, immunostimulation of the FNPs was further evaluated using the primary splenocytes isolated from C57BL/6 mice, which have all types of immune cells and the cross talk between immunocytes, including macrophage and T cells [98, 103].

Figure 18 Effects of the FNPs on the secretion of cytokines (A and B), chemokines (C and D) and nitric oxide (E and F) from RAW 264.7 macrophage cells (A, C and E) and splenocytes (B, D and F).

The macrophage RAW264.7 cells and splenocytes were treated with the FNPs at the GAG concentration of 5μg/ml for 24 h, and then the culture media were collected. A panel of 12 cytokines and 12 chemokines in the culture media were measured using ELISArry kits, and the nitric oxide in the culture media was detected with Griess assay. The results are expressed as mean ±SD. *P < 0.05, †P < 0.01, significantly different from the controls.

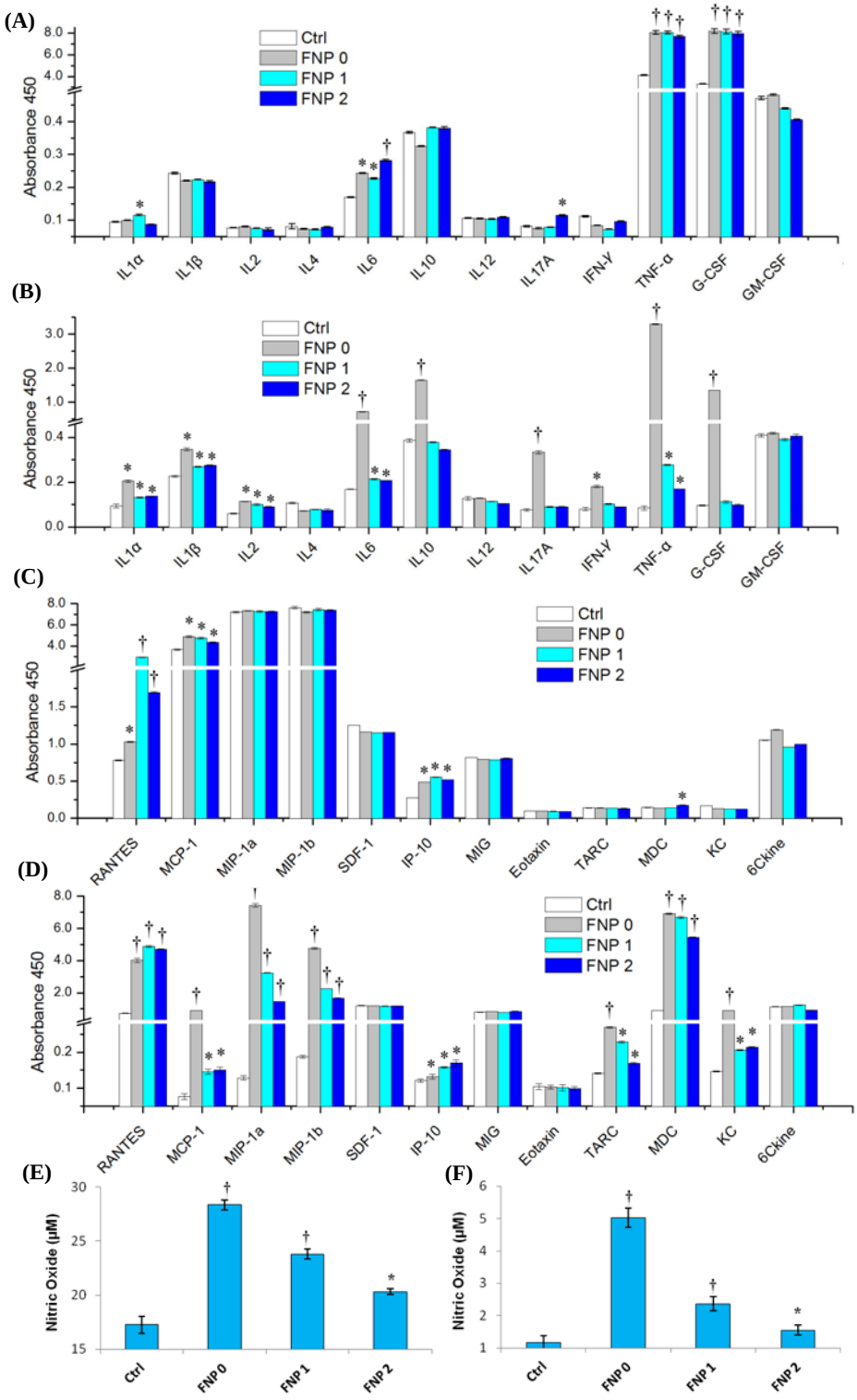
(A)
Absorbance 450
Ctrl
FNP 0
FNP 1
FNP 2
IL1α
IL1β
IL2
IL4
IL6
IL10
IL12
IL17A
IFN-γ
TNF-α
G-CSF
GM-CSF
(B)
Absorbance 450
Ctrl
FNP 0
FNP 1
FNP 2
IL1α
IL1β
IL2
IL4
IL6
IL10
IL12
IL17A
IFN-γ
TNF-α
G-CSF
GM-CSF
(C)
Absorbance 450
Ctrl
FNP 0
FNP 1
FNP 2
RANTES
MCP-1
MIP-1a
MIP-1b
SDF-1
IP-10
MIG
Eotaxin
TARC
MDC
KC
6Ckine
(D)
Absorbance 450
Ctrl
FNP 0
FNP 1
FNP 2
RANTES
MCP-1
MIP-1a
MIP-1b
SDF-1
IP-10
MIG
Eotaxin
TARC
MDC
KC
6Ckine
(E)
Nitric Oxide (μM)
Ctrl
FNP0
FNP1
FNP2
(F)
Nitric Oxide (μM)
Ctrl
FNP0
FNP1
FNP2

As expected, significantly higher amount of IL6 and TNF-α were detected in the culture supernatant of the splenocytes treated with the three FNP samples (**Figure 18B**) in comparison with the untreated control. The other stimulatory cytokines, including IL-1α, IL-1β and IL2, were also secreted in a low but significantly higher amount from the treated groups with the three FNP samples. It has been reported that IL-1 has multiple effects, involving immunomodulation, inflammation, wound healing, hematopoiesis, metabolism and the endocrine system [130]. IL-1, including IL1α and β, also has a number of properties potentially useful in the treatment of cancer, including direct antiproliferative activity against certain human tumor cell lines and several murine tumors, the activation of effector cells in vitro, and the inhibition of tumor angiogenesis [130]. In addition, IL-1 has the capacity to protect and restore the bone marrow from radiation or chemotherapy-induced injury [130]. The cytokine IL-2 is known to be a T-cell growth factor, inducing clonal expansion of T cells following antigen stimulation, and is also important for the differentiation of CD4+ T cells into Th1 and Th2 effector subsets [73]. IL-2 has been used for the treatment of melanoma and renal cell carcinoma [131], and recombinant human IL-2 is a potent cytokine and a FDA-approved anticancer drug [132]. As such, we believe that the three cytokines, IL-1α, IL-1β and IL-2, with elevated levels in the supernatant of splenocytes after the treatment with the FNPs also favor the antitumor immunity in the cancer treatment. Additionally, in the treated splenocytes, only the crude fungal nanoparticle, FNP0, induced significantly higher amount of IL-10, IL-17A, IFN-γ, and G-CSF as compared to the untreated control, while the purified FNPs

didn’t show this activity. As is well known, IFN-γ is a functionally pleiotropic cytokine, is able to induce anti-viral activity, and has direct anti-proliferative effects on some tumor cell lines [133]. Hence, like G-CSF, IFN-γ is also benefit for antitumor immunity. Unfortunately, both purified fungal nanoparticles, FNP1 and FNP2, didn’t have the activity on both macrophage and splenocytes. However, the bias in immunostimulatory activity between the purified FNPs and the crude FNPs may also helpful to establish the antitumor immunity *in vivo*, because the elevated level of IL-10, an anti-inflammatory, immunosuppressive cytokine that favors tumor escape from immune surveillance [134], was observed in the supernatant of splenocytes treated with the crude fungal nanoparticles, FNP0. It is notable that a higher amount of another cytokine, IL-17A, was observed from the treated splenocytes by the crude FNP0, and a low but significant increase in this cytokine was also observed in the treated macrophage by the FNP2. The role of IL-17A in anti-tumor immunity is controversial and remains elusive, and both pro- and anti-tumor activities of IL-17A have been reported [135, 136]. Overall, these results suggest that the FNPs, especially two purified FNPs, can potentially modulate the immune cells to an activated state to induce an efficient antitumor response in the cancer immunotherapy.

Subsequently, we investigated the production of chemokines by the FNPs in both macrophages and splenocytes. Chemokines are small chemotactic cytokines which can induce migration of leukocytes, activate inflammatory responses, and are implicated in the regulation of tumor development and growth [137]. They can modulate tumor growth via regulation of tumor-associated angiogenesis, by

activation of host immunological responses, by direct inhibition of tumor cell proliferation [137], or by modulation of the neutrophils influx into the tumor tissue after treatment with chemo-drug during the immunochemotheray [138]. As shown in **Figure 18C**, of the panel of 12 chemokines assayed, TRANTES, MCP-1 and IP-10 were highly induced in the treated macrophages by the three FNPs, and low but statistically significant increases in MDC was also observed in the FNP2-treated macrophages. It has been reported that RANTES enhances anti-tumor immunity in a mouse model in part through direct T cell effector recruitment [78, 79]. MCP-1 has been reported to augment the antitumor effects by promoting lymphocyte infiltration into the tumor and subsequent cytokine production [139]. IP-10 has been demonstrated to elicit strong anti-tumor and anti-metastatic properties, and its immunological properties appear to be dependent on the attraction of monocytes and T lymphocytes [80], while MDC is chemotactic for a variety of leukocytes, and has been shown to be involved in Th-2 mediated cellular immunity [140]. For the activation of the splenocytes, except for RENTES, MCP-1, IP-10 and MDC, the elevated levels of the MIP-1a, MIP-1b, TARC, and KC were also observed after treatment with the three FNPs as compared to untreated control (**Figure 18D**). It has been demonstrated that MIP-1a showed potent anti-tumor effect after intravenous administration along with intra-tumor injection of certain adjuvants [141], while MIP-1b is a chemokine which can chemoattract T cells and NK cells, inducing efficient antitumor responses in a pre-established tumor model [137]. In conjunction with RANTES, TARC, which mediate the chemoattraction of both antitumor-specific effector T

cells, has been demonstrated to enhance the antitumor immune effects of GM-CSF [142, 143]. The production of chemokine KC may amplify filtration of inflammatory cells, creating a more sustained antivascular action [138]. Given the elevated cytokines and chemokines from both macrophage and splenocytes, they provide the evidences that the favorable antitumor immunity *in vivo* could be established by stimulating different immunocytes, such as macrophages and splenocytes, with the fungal nanoparticles, especially the purified FNPs, FNP1 and FNP2. Apart from multiple cytokines and chemokines, the bactericidal mediator, nitric oxide (NO), stimulated by the FNPs was further evaluated on both macrophages and splenocytes. As shown in **Figure 18E-F**, compared to the untreated cells, significantly elevated levels of NO were produced in both macrophages and splenocytes treated with the FNPs. NO is an important regulator and mediator of macrophage-directed cytotoxicity against tumor cells and microbes [119]. Significantly higher amount of NO production from the treated macrophages and splenocytes substantiates the potential of anti-cancer immunity in the cancer immunotherapy using the polysaccharide-based nanoparticles secreted from fungi.

FNPs induce cytotoxicity in tumor cells via apoptosis and cell cycle arrest

The cytotoxicity of the crude FNPs, prepared with dialysis method, has been demonstrated in A549 and B16BL6 cell lines in our previous study. In this work, after obtaining two different FNP fractions, FNP1 and FNP2, we further

investigated the in vitro cytotoxicity of both purified FNPs in four different tumor cell lines. As shown in Figure 19 A-C, the three FNP samples showed a dose-dependent cytotoxicity against four tumor cell lines, including A549, B16BL6, MCF-7 and MCF-7/ADR. For the crude FNP0 sample, ~11-39% inhibition of cell proliferation were seen in the three tumor cell lines, A549, B16BL6 and MCF-7, at the concentration ranging from 1-10 μg/ml. For the purified FNP2, the inhibition rates of 26-37% for B16BL6 cells, 9-33% for A549 cells, and 3-30% for MCF-7 cells were observed at the same concentration range. However, using a higher concentration range (2-25μg/ml), the purified FNP1 showed similar inhibition rates in the three tumor cells, i.e., 15-32% for B16BL6 cells, 11-28% for A549 cells, and 3-28% for MCF-7 cells. In comparison with the FNP1 and FNP2, we found that the similar inhibition rates in the three tumor cells were resulted from different concentration ranges. The concentrations of the FNP1 were at least 2-fold higher than those of the FNP2, indicating that the purified FNP2 have stronger cytotoxic activity than the purified FNP1. In addition, it is notable that all the three FNP samples showed lower inhibition rates (8-18% for the FNP0, 5-15% for the FNP1, and 9-17% for the FNP2) in the multidrug resistant cell line MCF-7/ADR at the respective concentration ranges. The lower inhibition rates here suggest that the FNPs only possess mild to moderate cytotoxic activity and the maximal concentration tested in this study is still not enough to effectively inhibit the proliferation of the resistant cells.

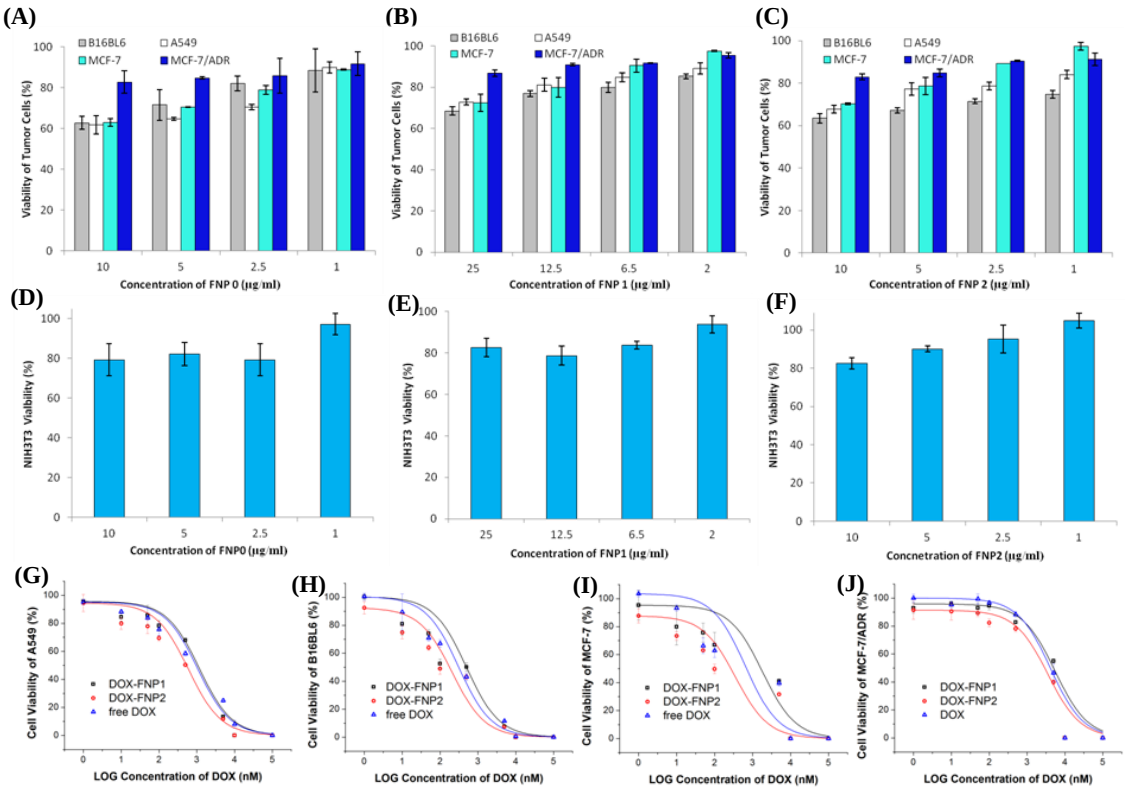

Figure 19 Cytotoxicity of the FNPs and the DOX-FNPs complexes against multiple cell lines.

(A-C) The cytotoxicity of the FNPs against four tumor cells, i.e. human non-small-cell lung cancer A549 cells, mouse melanoma B16BL6 cells, human breast cancer MCF-7 cells and the multidrug resistant cell line MCF-7/ADR; (D-F) The cytotoxicity of the FNPs against mouse embryo fibroblast cell line NIH3T3; (G-J) The cytotoxicity of the DOX-FNP complexes against four tumor cell lines (A549, B16BL6, MCF-7 and MCF-7/ADR). The sigmoidal dose-response curves were fitted using OriginPro 8.0.

Even for the sensitive tumor cells, the highest inhibition rates were still less than 40% at the maximal concentration of 10μg/ml for FNP2 or 25μg/ml for FNP1. The mild to moderate cytotoxic activity of the FNPs were further evidenced by an in vitro biocompatibility test using NIH3T3 cell line. NIH3T3 is a mouse embryo fibroblast, which were commonly used in the biocompatibility evaluation of nanomaterials [120, 144]. Less than 20% inhibition rate were seen in NIH3T3 cells treated with the three FNPs at the respective concentration ranges (Figure 19D-F), suggesting that the FNPs didn't have strong cytotoxic effect against normal cells, but had slightly higher cytotoxicity against tumor cells, especially towards the sensitive tumor cells.

Even though the FNPs only possess mild to moderate cytotoxic activity, given that the FNPs induced the secretion of multiple proinflamatory cytokines and chemokines from immunocytes (**Figure 18**), we believe that they are a potential immunomodulator of biological responses in the adjuvant antitumor therapy in which the synergistic effect could be reached between the mild cytotoxic activity and the immunostimulatory activity. For the purified FNPs, we have demonstrated a similar immunostimulatory activity between the FNP1 and FNP2, inducing almost same levels of cytokines and chemokines from immunocytes (**Figure 18**). However, as far as the cytotoxic activity concerns, the FNP2 showed around 2-fold stronger activity in the tumor cells tested in this study (**Figure 19A-C**). To better understand the difference in the cytotoxicity between both purified FNPs, we further investigated the apoptotic effect and cell cycle arrest in the tumor cells treated by both purified FNPs. As expected, the purified

FNP2 induced strong apoptosis in the A549 cells and B16BL6 cells after an 48-h incubation, and the crude FNP0 had similar but weaker apoptosis induction in both tumor cells; however, the purified FNP1 couldn't induce significantly apoptotic effect in A549 tumor cells and induced only slight apoptotic effect in B16BL6 cells (**Figure 20A-B**), which may explain the weaker cytotoxicity of the FNP1 as compared to the FNP2. The cell cycle arrest analysis using A549 and B16Bl6 cells treated with both purified FNPs substantially agrees with the apoptosis assay. As shown in **Figure 20C-D**, the FNP2 arrested the cell cycle at sub G0/G1 phase in both tumor cells after an 24-h incubation, and the crude FNP0 showed the similar activity in both tumor cells. A significant increase in the sub G0/G1 peak, which corresponds to apoptotic cells, represents that the tumor underwent apoptosis [145, 146]. However, the purified FNP1 couldn't significantly induce the cell cycle arrested at the sub G0/G1 phage, indicating that there should be different mechanisms for the cytotoxicity of the purified FNP1 and FNP2, although they showed similar immunostimulatory activity.

Formation of pH-responsive complexes by efficiently binding DOX to FNPs

Utilizing the purified FNPs as a nanocarrier for chemo-drug delivery is the purpose of this study to implement the synergistic effect between the immunostimulation from FNPs themselves and cytotoxicity from both FNPs and chemo-drugs. For such a purpose, DOX was used as a model chemo-drug in this study to form a DOX-FNP nanocomplex.

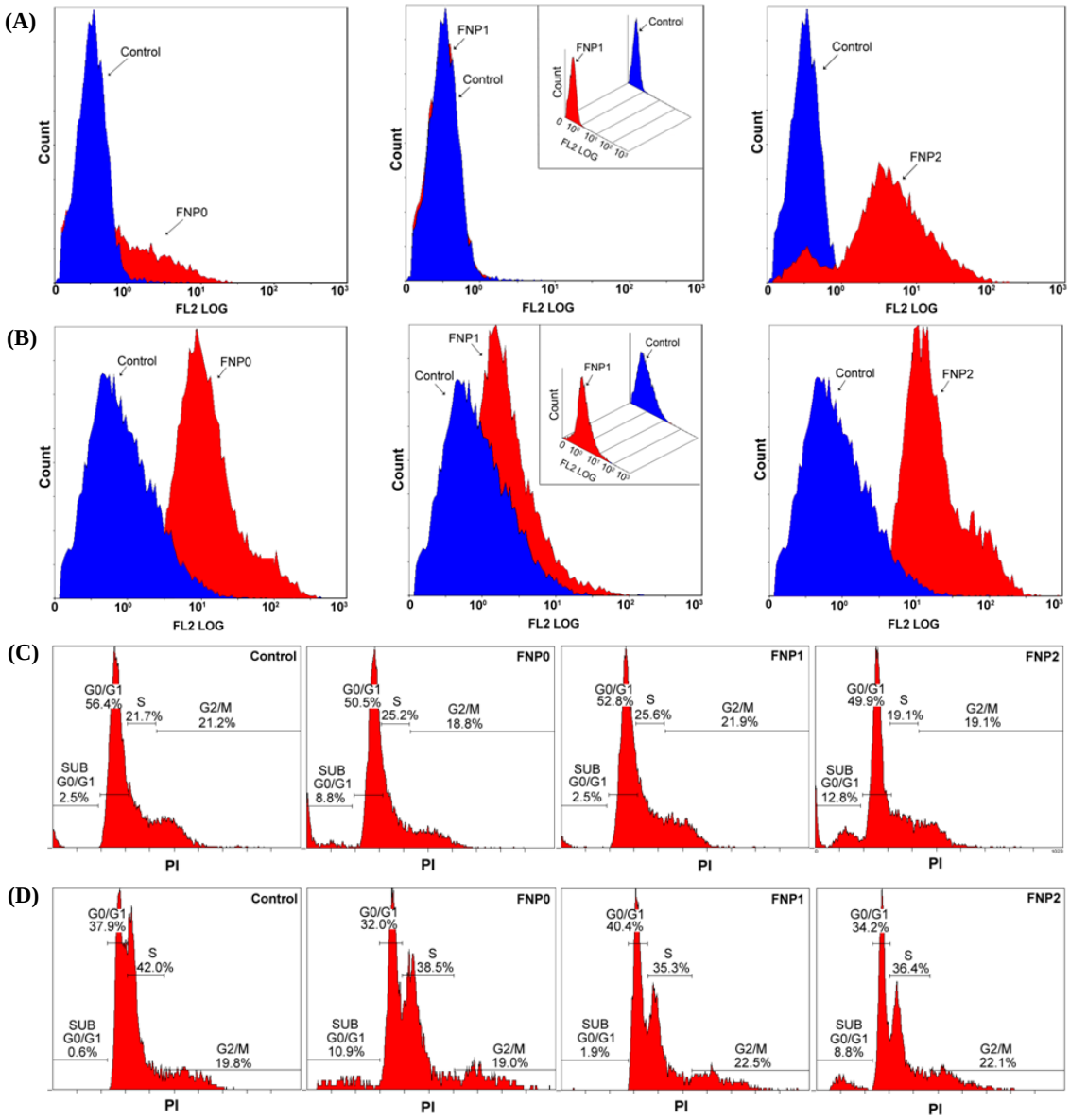

Figure 20 Apoptosis (A-B) and cell cycle arrest (C-D) in human non-small-cell lung cancer A549 cells (A and C) and mouse melanoma B16BL6 cells (B and D) induced by the FNPs.

The cells were treated with the FNPs at the GAG concentration of 10μg/ml for 48 h (apoptosis assay) or 24h (cell cycle analysis). For apoptosis assay, the fragmented DNA was stained with TUNEL method (M&M Section 2.6) and then measured by flow cytometry. For cell cycle analysis, the cells were stained with PI, and then measured with flow cytometry.

The physical characteristics, *in vitro* cytotoxicity and immunochemotherapeutic effect of the complexes were further evaluated. As shown in **Figure 21A**, DOX could be efficiently bound to both fungal nanoparticle fractions, FNP1 and FNP2, when mixing DOX and the FNPs in 20mM HEPES buffer at pH 7.0. Due to negative surface charges for both FNP1 and FNP2 (**Table 4**), DOX, carrying positive charges from deprotonation of the amino group at pH7.0 in HEPES buffer [147], could be bound to FNPs via electrostatic interactions. The binding between DOX and FNPs was so highly efficient that leads to formation of precipitates overnight after centrifugation at 10,000 rpm for 10min (**Figure 21A**). The collected precipitates were then dispersed in PBS buffer (pH 7.0) and nano-sized DOX-FNP complexes were formed. As shown in Table 2, for both complexes, DOX-FNP1 and DOX-FNP2, the hydrodynamic diameters, measured by DLS analysis, were less than 200nm, which was slightly increased compared to the blank FNPs (**Table 4**). The morphology of the dispersed DOX-FNP complexes in the PBS buffer was also imaged with AFM, and both DOX-FNP complexes were spheroidal nanoparticles with diameters of less than 200 nm (**Figure 21 C-D**), similar to the blank FNPs (**Figure 16**). In addition, from **Table 5**, there were significant decreases in zeta potentials for the DOX-FNP complexes as compared to both blank FNPs, indicating a direct association of DOX with the FNPs via electrostatic interactions [148]. More importantly, the entrapment ratio of DOX in the FNPs was as high as ~72%-77%, and the precipitated DOX-FNP complexes with such a high drug loading were demonstrated to be stable after the nano-sized DOX-FNP complexes were formed in the PBS buffer.

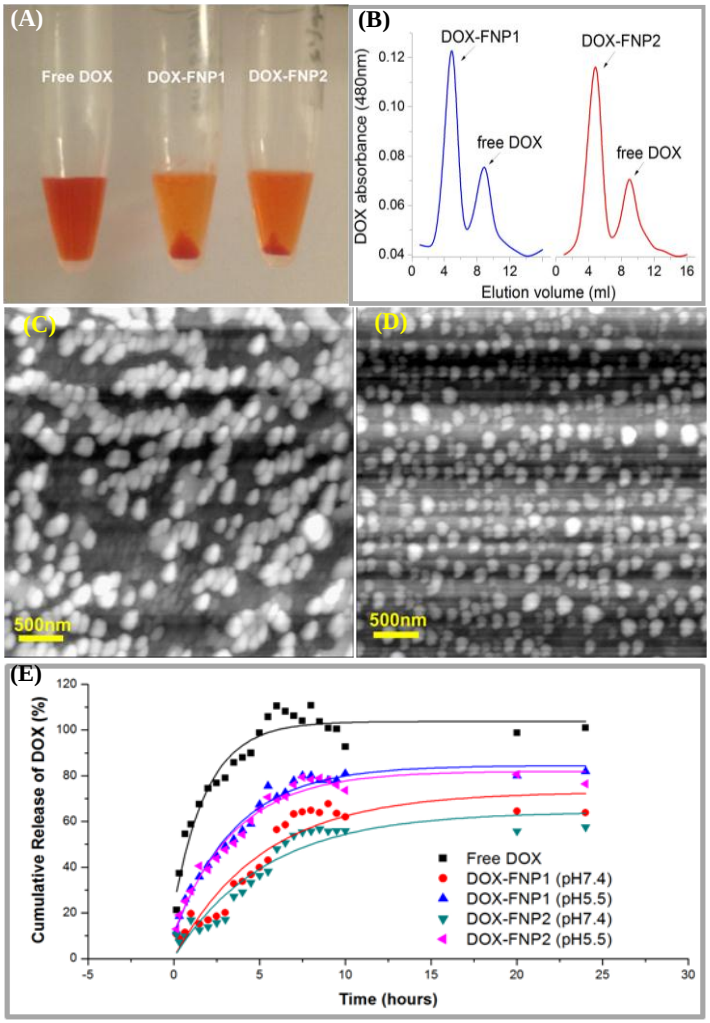

Figure 21 Characterization of the DOX-FNP complexes and pH-responsive release of DOX from the complexes.

(A) The DOX-FNP complexes were precipitated in 20mM HEPES buffer (pH7.0) after centrifugation at 10,000 rpm for 10min; (B) Purification of the precipitated DOX-FNPs complexes from free DOX using SEC column after being well dispersed in PBS buffer (pH7.4); (C) AFM images of the DOX-FNP1 complexes; (D) AFM images of the DOX-FNP2 complexes; (E) pH-responsive release of DOX from the complexes.

Table 5 Physical characteristics and cytotoxicity of the DOX-FNP complexes

	Size	Zeta potential	Entrapment ratio	IC_{50} (nM)			
				A549	B16BL6	MCF-7	MCF-7/ADR
DOX-FNP1	194.5±79.5	-22.2±7.5	77.4%±2.4%	1170.60±92.33	494.87±38.00	1830.53±270.47	5464.57±16.87
DOX-FNP2	186.9±89.7	-24.24±6.0	72.2%±0.7%	599.34±15.85	209.63±23.72	355.71±23.06	3522.55±110.03
Free DOX	-	-	-	1052.54±67.58	308.82±26.55	648.39±75.77	4177.36±116.12

As shown in **Figure 21B**, the amount of DOX dissociated from the complexes in the PBS buffer was as low as ~20%. As such, the DOX-FNPs complexes dispersed in PBS buffer were directly used as a nano-sized antitumor agent without further purification to remove free DOX for the following studies, including uptake, cytotoxicity and immunochemotherapeutic effect.

In principle, pH-responsive release of DOX was expected from the nano-complexes formed via an electrostatic driving force between DOX and nanoparticles, which could provide a stimulus-responsive release mechanism after internalization by tumor cells or penetration into the tumor tissue in vivo [149]. The release profiles of DOX from both complexes at different pHs were further evaluated by immersing the dialysis tubes in large volume centrifuge tubes containing 6 ml of release buffers with different pH values. As shown in **Figure 21E**, a free DOX control confirmed that the dialysis membrane tubing with 300K MWCO in this study couldn't restrict diffusion of the released drugs into the bulk release media in which the sink condition was established, and they were able to reach 100% release after 5 h. However, the release of DOX from both complexes at different pH couldn't reach a plateau until at least 9-10 h. The total released drug from both DOX-FNP complexes was significantly different under different pH conditions (**Figure 21E**). Up to ~55% and ~65% of total drug were released at the physiological pH 7.4 for the DOX-FNP1 and DOX-FNP2 complexes, respectively; however, around 80% of total drug released at pH 5.5 were observed for both complexes. More importantly, the release rate of drug from both complexes increased with decreasing in the pH of release medium,

indicating a pH-sensitive release behavior with accelerated release of DOX in an acidic environment from both complexes. This favorable property is believed to facilitate passive tumor targeting and endosome escaping since the interstitial space of solid tumors and intracellular endosome compartments have a lower pH value [56].

Cytotoxicity, uptake and intracellular distribution of DOX-FNP complexes in tumor cells

Fungal nanoparticles have been demonstrated to be cytotoxic in our previous study [114]. In current work, we also confirmed that both purified fractions, FNP1 and FNP2, had mild to moderate cytotoxic activity against multiple tumor cell lines. However, compared to the FNP1, the FNP2 itself at the same GAG concentration had around 2-fold increase in cytotoxicity against 4 tumor cell lines tested in this study (**Figure 19 A-C**). In our early study, we demonstrated that there was synergistic cytotoxicity exerted by covalently conjugating DOX with FNPs via amide bond [114]. As such, a synergistic cytotoxic effect between DOX and the FNPs when forming the physical complexes via the electrostatic interactions is anticipated in this study. As expected, the DOX-FNP2 complexes showed significantly higher cytotoxicity against 4 tumor cells than free DOX after a 48-h incubation (**Figure 19 G-J**). The IC50 of the DOX-FNP2 complexes and free DOX are listed in **Table 5**. For A549, B16BL6 and MCF-7 cell lines, the IC50 for the DOX-FNP2 complexes was ~1.5-1.8 fold lower than free DOX; even for

the multidrug resistant cell line MCF-7/ADR, the IC50 for the DOX-FNP2 was still ~1.2 fold lower than free DOX. These data demonstrate a synergistic cytotoxic effect when DOX was bound to one fraction of the FNPs, i.e., FNP2, even against the resistant tumor cell line. As shown in Figure 5G-J, at the respective IC50 values of free DOX (**Table 5**), free DOX inhibited cell proliferation by 50%, whereas the DOX-FNP2 complexes showed ~62%-75% inhibition against the four tumor cells. According to a ~72% entrapment ratio for the DOX-FNP2 complexes (**Table 5**), the concentration of the FNP2 in the complexes at the respective IC50 values of free DOX for the A549, B16Bl6 and MCF-7 cells was calculated to be less than 0.25 μg/ml of GAG concentration, and for the resistant MCF-7/ADR cells less than 1.0μg/ml of GAG concentration. From **Figure 19A-C**, almost no significant inhibition effect on four tumor cells was observed at that concentration for FNP2 itself, indicating that DOX and FNP2 in their physical complexes via the electrostatic interactions exerted synergistic cytotoxic effects and led to the IC50 values 1.2-1.8 fold lower against four different tumor cells (**Table 5**).

Unexpectedly, the cytotoxicity of the DOX-FNP1 complexes was similar or even lower than free DOX in the four different cell lines, which is completely different from the DOX-FNP2 complexes. As shown in **Table 5**, the IC50 values for the DOX-FNP1 complexes were ~1.1-2.8 fold higher than free DOX against 4 tumor cell lines, indicating that there is no obvious synergistic effect between DOX and the FNP1 upon forming the physical complexes. We postulate that the difference in the cytotoxicity of both complexes was due to their different cytotoxicity of the

FNPs themselves, because the FNP1 showed at least 2-fold higher cytotoxicity against different tumor cells than the FNP2 at the same GAG concentration (**Figure 19A-C**). Presumably, the differences in the cytotoxicity of the FNPs portend the different chemical structures for both FNP1 and FNP2 fractions, including polysaccharide chain, monosaccharide composites and linkages, uronic acid content, sulfation degree, and possible core proteins. Although the similar chemical components were characterized for both FNPs in the Table 1 and **Figure 17**, showing that the polysaccharide including acidic GAG and neutral polysaccharides were main components in both FNPs, the specific chemical structures for both FNPs still remained elusive. We presume that different chemical structures in both purified FNPs eventually lead to different cytotoxicity of FNPs themselves and the DOX-FNP complexes, as well as the different physical properties including zeta potential and morphology (**Table 4**, **Figure 16** and **21**).

In order to elucidate whether the different cytotoxicity between the DOX-FNP1 and DOX-FNP2 complexes is related to DOX uptake and intracellular distribution after forming the complexes, we quantitatively analyzed the cell-associated DOX fluorescence intensity using flow cytometry after treatment of both tumor cell lines, A549 and B16BL6, with both complexes. As shown in **Figure 22**, for both tumor cells, there was no significant difference in the DOX fluorescence for both complexes and free DOX at the DOX concentration of 10 μM after a 4-h incubation, indicating that DOX uptake wasn’t impeded upon the formation of the DOX-FNP complexes via the electrostatic interactions.

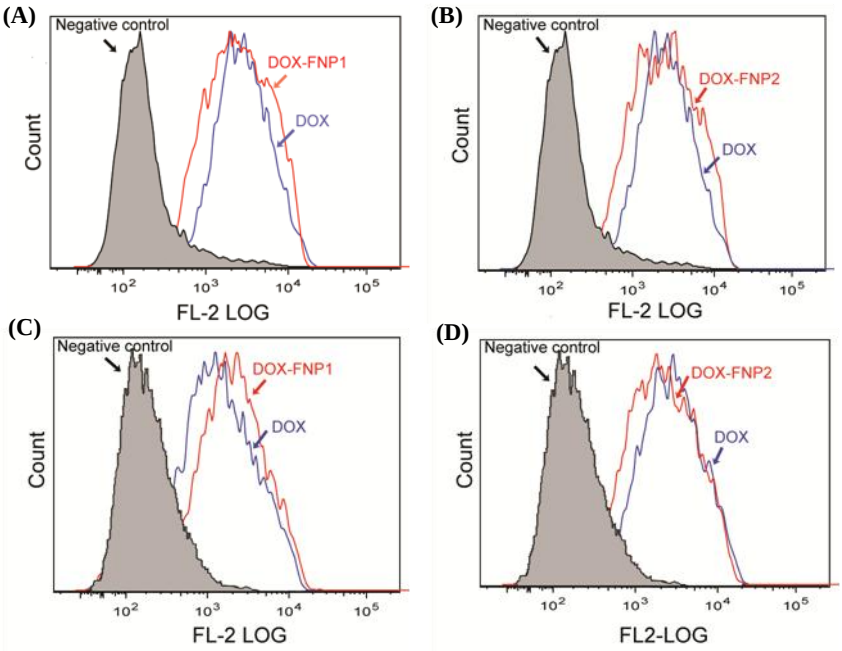

Figure 22 Quantitative analyses of DOX uptake by human non-small-cell lung cancer A549 cells (A-B) and mouse melanoma B16BL6 cells (C-D).

Both cells were treated with the DOX-FNP complexes or free DOX at DOX concentration of 10 μM for 4 h, and then the mean DOX fluorescence associated with the cells were measured by collecting 20 000 events for each sample.

On the other hand, these data substantiate that the different cytotoxicity of both complexes was from their different cytotoxicity of the FNPs themselves rather than the increase in the DOX uptake enhanced by the FNPs in the tumor cells.

To further observe intracellular distribution of both DOX-FNP complexes, the nuclei and endolysosome were labeled with a nucleus-specific dye, Hoechst 33342 (blue), and an acidic endolysosome-specific dye, LysoTracker green DND-26, respectively. Before investigating both DOX-FNP complexes, we first tested if the FNPs themselves could be efficiently internalized in the tumor cells. For such a purpose, the FNPs were conjugated with FITC (**Table 6**), and then incubated with A549 tumor cells for 4 hours. As shown in **Figure 23**, both purified FNPs, FNP1 and FNP2, were confirmed to be efficiently taken up by the tumor cells after a 4-h incubation. The internalization of FNPs themselves by tumor cells substantially indicates that the FNPs themselves could mediate the uptake and distribution of DOX in tumor cells via the DOX-FNP complexes, instead of free DOX released from the complexes. Upon confirming the uptake of the FNPs themselves by tumor cells, we imaged sub-cellular distribution of the DOX-FNP complexes in both tumor cells, A549 and B16BL6. As shown in **Figure 24**, the confocal analysis showed that different intracellular distribution of both DOX-FNP complexes and free DOX was observed in both tumor cells after a 4-h treatment. The majority of DOX in both cells incubated with both complexes were predominantly distributed in the endolysosomal compartment, while most of the free DOX was located outside the organelle.

Table 6 Characteristics of the FITC-labeled FNPs*

	Size (nm)	Zeta potential (mV)	Conjugation ratio (%)
FITC-labeled FNP1	246.9±42.6	-19.9±3.8	0.031%±0.007%
FITC-labeled FNP2	252.5±60.6	-27.1±0.9	0.025%±0.009%

*Note: The preparation of FITC-labeled FNPs was detailed in the M&M Section 2.10.

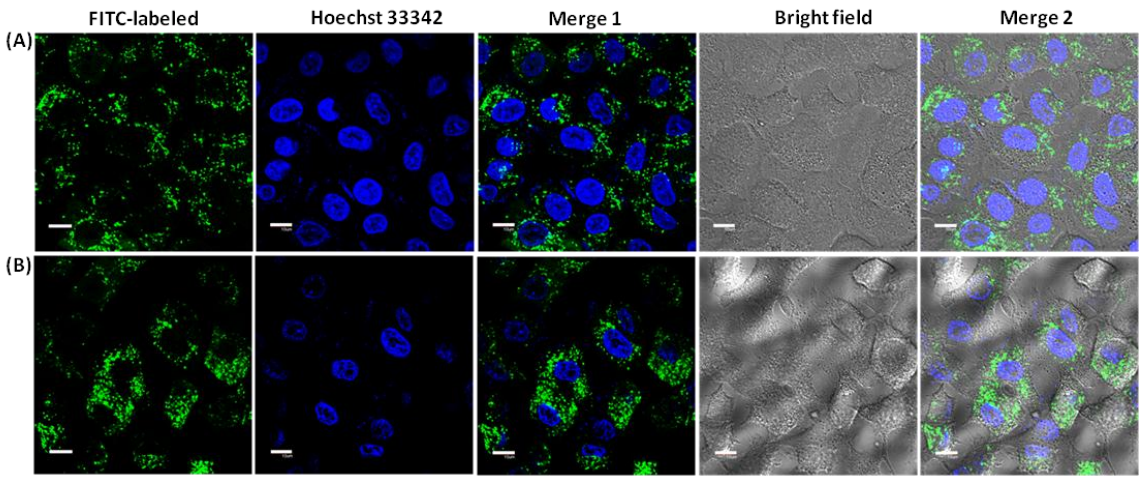

Figure 23 Internalization of the purified FNP1 (A) and FNP2 (B) themselves in human non-small-cell lung cancer A549 cells.

Both FNPs were labeled with FITC and then incubated with A549 cells at the FITC concentration of 2ng/ml for 4h. For confocal imaging, the nuclear-specific dye Hoechst 33342 was used to label the tumor cell nuclear. The cells were also recorded in the bright-field for the morphology. Scale bars represent 10 μm.

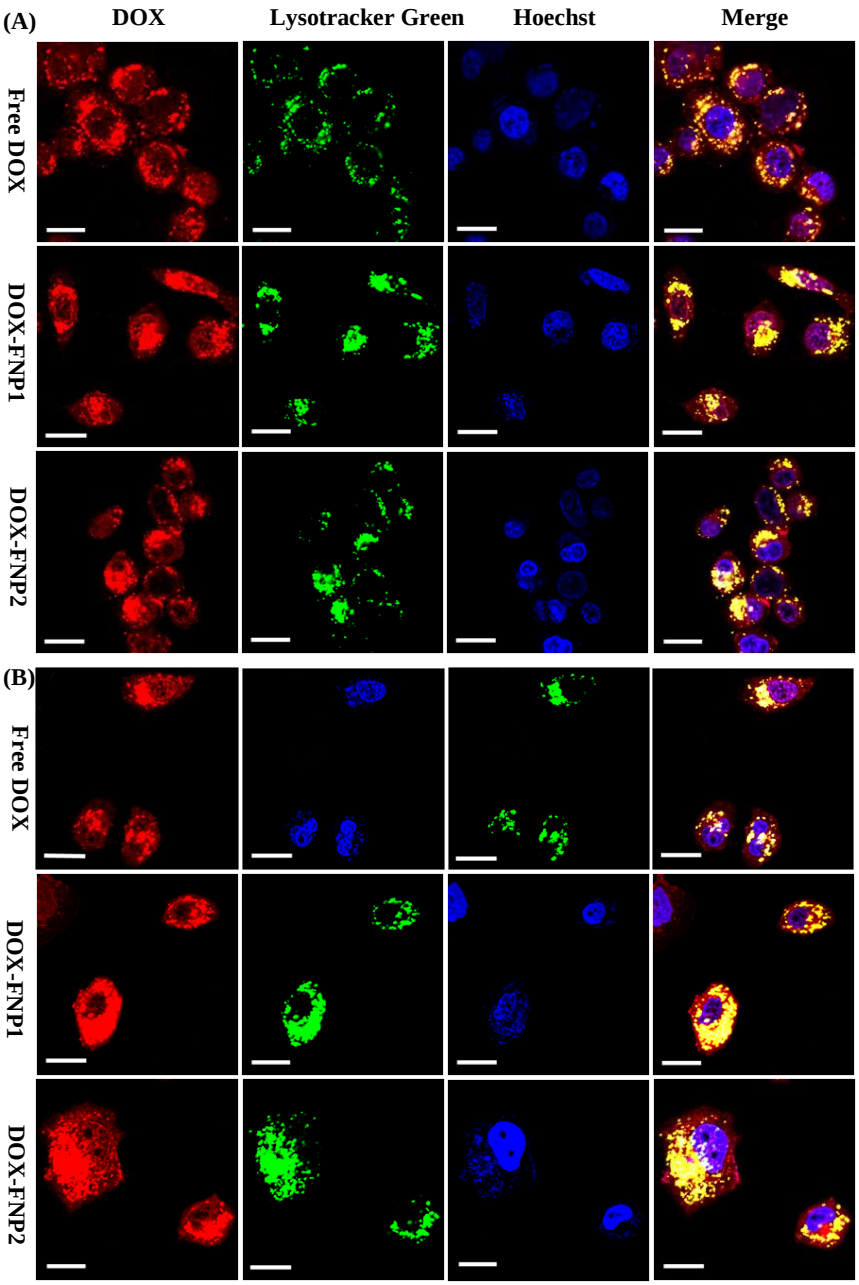

Figure 24 Confocal analysis of intracellular distribution of the DOX-FNP complexes at the DOX concentration of 10 μM in human non-small-cell lung cancer A549 cells (A) and mouse melanoma B16BL6 cells (B).

The cells were incubated with the samples at 37 °C in 5% CO2 for 4 h, and then 100 nM Lysotracer Green DND-26 and 4 μM Hoechst 33342 were added for 30 min incubation prior to imaging by confocal microscopy. Scale bars represent 10 μm.

As is well known, major nanoparticles internalized via endocytosis were mainly found within endosomes or lysosomes [150]. Thus, we presume that the DOX-FNP complexes might be internalized by endocytic pathway in both tumor cell lines. In this study, the DOX-FNP complexes were demonstrated to have a pH-sensitive release behavior with accelerated release of DOX in an acidic environment (**Figure 21B**), which facilitate DOX escaping from endosome or lysosomes after internalization of both complexes in tumor cells. Hence, we believe that the different distribution couldn't be another cause that led to the different cytotoxicity for both DOX-FNP complexes. Overall, the results here demonstrate that even though there was a different sub-cellular distribution, the formation of the DOX-FNP complexes did not decrease DOX uptake by both tumor cell lines, which further supports that the different cytotoxicity of both complexes was from their different cytotoxicity of the FNPs themselves against tumor cells.

Immunochemotherapeutic activity of DOX-FNP complexes in an in vitro co-culture system

After demonstrating the different cytotoxicity of both DOX-FNP complexes against tumor cells, the hypothesis of combined immunochemotherapy using the complexes was further confirmed by the co-culture analysis. The co-culture study is an *in vitro* model system for mimicking *in vivo* situation [98, 103]. For such a purpose, B16BL6 tumor cells were first labeled with CFSE, and co-incubated with splenocytes isolated from C57BL/6 mice; the co-cultures were then incubated

with either DOX-FNP complexes, or free DOX at the DOX concentration of 1μM for 24h. As expected, significantly higher death of the cancer cells was observed with the treatment of the DOX-FNP2 complexes as compared to free DOX or the DOX-FNP1 complexes (**Figure 25**), which is consistent with the data in the direct cytotoxicity experiment using MTT assay (**Figure 19G-J** and **Table 5**). As the DOX-FNP2 complexes had both cytotoxic and immunostimulating activity, these two might be cooperating with each other to produce a synergistic effect, resulting in higher death in the co-culture cells treated with the complexes. Interestingly, compared to the direct cytotoxicity experiment where the DOX-FNP1 complexes had lower cytotoxicity than free DOX (**Figure 19G-J** and **Table 5**), in the co-culture experiment where a mixed culture of cancer cells and splenocytes were treated, the DOX-FNP1 complexes unexpectedly enhanced tumor cell death as compared to free DOX alone. In this co-culture experiment, higher death of the cancer cells exerted by both complexes, especially the DOX-FNP1 complexes could be attributed to the immune stimulatory activity of the FNPs as both FNPs have been shown to induce the secretion of multiple pro-antitumor cytokines and chemokines from splenocytes, such as TNF-α and MIP-1a, which has direct cytotoxic activity. Overall, the enhanced tumor cell death by both complexes in this experiment confirmed the potential in combined caner immunochemotherapy using the DOX-FNP complexes *in vivo* in the future.

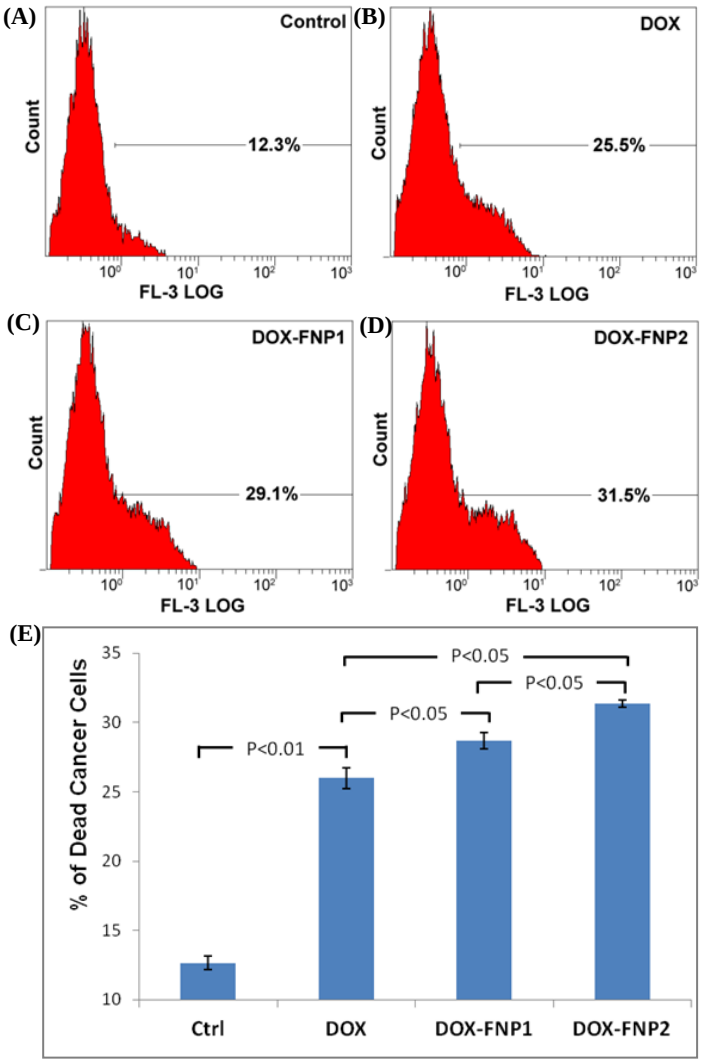

Figure 25 Chemo-immunotherapeutic activities of both DOX-FNP complexes in an in vitro experimental system where B16BL6 tumor cells were first labeled with CFSE and then co-cultured with the splenocytes derived from C57BL/6 mice.

The co-cultures were treated with free DOX (B) and both DOX-FNP complexes(C-D) at the DOX concentration of 1μM, incubated for a 24-h, and then the death of tumor cells was determined by the PI uptake method using flow cytometry after gating on the CFSE labeled cancer cells. The untreated co-cultured cells were used as a negative control (A). Statistical analysis of the mean DOX fluorescence associated with the cells was performed, and significant differences (P<0.05) between different treatments were observed (E).

Conclusions

The purpose of this study was to evaluate the immunostimulatory activity, dissect the mechanism of the cytotoxicity, and explore the potential in cancer immunochemotherapy using the FNPs as a multifunctional nanocarrier. For such a purpose, we first established a new isolation procedure, SEC-WAX-SEC, to purify the FNPs, by which two purified FNP fractions, FNP1 and FNP2, were prepared. AFM imaging and DLS analysis showed that both purified FNPs had a reduced diameter of 100-200 nm compared to the crude FNPs. SDS-PAGE and chemical assays showed that polysaccharide including glycosaminoglycan were main constituents in the purified FNPs. They were demonstrated to enhance the secretion of multiple proinflammatory cytokines and chemockines from macrophages and splenocytes, measured by ELISArray, suggesting the efficacy of the FNPs as an immunomodulator of biological responses in the adjuvant antitumor therapy. MTT assay showed that both purified FNPs had mild to moderate cytotoxicity against multiple tumor cells but the FNP2 had stronger cytotoxic activity than the FNP1. The apoptotic assay and cell cycle analysis further demonstrated that the FNP2, not the FNP1, could inhibit cell proliferation via inducing apoptosis and arresting tumor cells at sub G0/G1 phase, which may explain the difference in the cytotoxicity between both FNPs. For testing the combined cancer therapy, both FNPs formed the pH-responsive nanocomplexes with chemo-drug, DOX, via the electrostatic interactions. Upon binding of DOX to the FNPs, it was demonstrated that the DOX-FNP2 complexes had higher

cytotoxic activity than free DOX against multiple tumor cells, while the cytotoxic activity of the DOX-FNP1 complexes was weaker than free DOX. Interestingly, in a co-culture experiment where splenocytes were co-cultured with tumor cells, both nanocomplexes demonstrated higher antitumor activity than free DOX, suggesting the synergistic effect between the immunostimulation of the FNPs and cytotoxicity of the nanocomplexes *in vitro*. In conclusion, this work developed a one-step therapy containing agents for both immuno- and chemotherapy using the natural-based nanoparticles as a multifunctional nanocarrier, which may open a new avenue for combined cancer therapy in the future.

CHAPTER IV
BIO-SYNTHESIS OF GOLD NANOPARTICLES USING ENGLISH IVY (HEDERA HELIX)

Introduction

Gold nanostructures have been used in many applications, including waveguides for electromagnetic radiation [151], optical coatings [11], Surface Enhanced Raman Spectroscopy (SERS) [152-154], and cancer diagnostics [155-159]. Consequently, various physical, chemical and biological methods have been reported to produce gold nanostructures [160-163]. Gold nanoparticles (AuNPs) can be produced using a multitude of chemical and physical processes; however, these approaches are often costly and have environmental risks associated with their production. To reduce the use of toxic chemicals used in typical AuNP synthesis, researchers are actively investigating alternative synthesis methods using biological materials (proteins, polysaccharides, polyphenol, etc.) for green-synthesis of gold nanoparticles [164-167].

Recently, several plants have been reported to efficiently synthesize gold and silver nanoparticles [168-170]. For example, the leaf extract from tea [171], lemongrasss [11], *Aloe vera* [172], *Fagopyrum esculentum* [165], and the fruit extract of *Embica officinalis* [173], and *Tanacetum vulgare* [174] have demonstrated the potential for reducing gold ions into AuNPs. According to these biosynthetic procedures, AuNPs could be obtained after simply mixing $HAuCl_4$ solution with the plant extract [166]. Multiple reductases and chemical reducing agents from the extracts have been found to be responsible for the formation of these nanoparticles [9]. For instance, NADPH, a common biological coenzyme [175], proteins, polyphenols, and carbohydrates from plant extracts have been suggested to be involved in the synthesis of AuNPs [9]. However, the exact

mechanism of this synthesis is still not completely understood, due to the large number of components in the plant extracts, any of which could be involved in the synthesis. The multitude of chemical compounds found in plant extracts also leads to the formation of various species of AuNPs from a single reaction. Synthesized AuNPs often vary in size, shape, and morphology, and further processing must be conducted to isolate a single species [13, 164, 166, 176-178]. Despite the ease of AuNP synthesis using plant extracts, a major hurdle exists in developing a sustainable procedure for the production of AuNPs. Previous studies have attempted to resolve this challenge by using live plants to synthesize AuNPs; however, most of these procedures involve harvesting AuNPs from the plant tissue, which introduces increased complexity due to the limited amount of AuNPs relative to the large plant biomass [48, 49]. Of greater concern for sustainability, is that the plant must be sacrificed to harvest the AuNPs, which means that plant will be removed from the production system. This will lead to the increased costs, and delay the production of the nanoparticles.

In this work, both a sustainable biological synthesis method and a rapid synthesis procedure have been developed for continuous and scalable manufacturing of gold nanoparticles. The proposed approaches allow for the production of AuNPs out of aqueous $HAuCl_4$ with either actively growing English ivy (*Hedera helix*) shoots or the extract formed from the adventitious roots. The synthesized AuNPs were easily collected from both methods requiring minimal time and effort. By replacing the $HAuCl_4$ solution every 24 hours, in the sustainable production system, AuNP synthesis was carried out over a period of 30 days using the same

raw material. The development of a robust and sustainable procedure for synthesizing AuNPs with a reduced environmental impact represents an important step forward in scalable green production of metal nanoparticles. Furthermore, the use of various molecular weight fractions of the adventitious root extract demonstrated the ability to rapidly form smaller nanoparticles than the sustainable method. Using these two methods, we have demonstrated how plant materials represent an efficient “green” solution to address the growing need for AuNP synthesis.

Materials and methods

Chemicals and Reagents

Chemical analysis grade hydrogen tetrachloroaurate (III) ($HAuCl_4$), 1,9-Dimethyl-Methylene Blue (DMMB)), chondroitin sulfate (CS), and phosphate buffered saline (PBS) were purchased from Sigma-Aldrich. For protein quantification, the BCA Protein Assay Kit (Pierce) was purchased from Thermo Scientific. Dialysis membranes were purchased from Spectrum Laboratories, Inc (Rancho Dominguez, CA). Ivy shoots and adventitious roots were donated from Swan Valley Farms (Bow, WA).

Method One: Sustainable synthesis of AuNPs using live shoots

Upon receipt, live ivy shoots were cut to lengths of 15 cm, leaving one attached leaf on the apical end of the stem. After sterilization and treatment with auxins, four shoots were placed into Magenta GA7 (MAG) boxes and held upright by placing them through holes cut into the lids. After 24 hours, the boxes were transported to a windowsill, where the nanoparticle synthesis was conducted. To initiate nanoparticles synthesis, aqueous $HAuCl_4$ was added to the 50 ml of water present in the MAG boxes to achieve concentrations of 0, 0.025, 0.05, 0.1, 0.2, 0.5, 1 and 5 mM. The shoots were exposed to these concentrations for 24 hours, before the solution was removed to test for nanoparticle production. After collecting the solution after 24 hours, fresh $HAuCl_4$ solution at the same concentration was added back to the MAG boxes. This method was repeated for the duration of the study. To concentrate any nanoparticles present in the solution, the solution was centrifuged at 14,000 rpm for 10 min. The supernatant

was then removed, and DI water was added to the precipitate. This procedure was repeated three times to remove soluble factors present in the solution, including secreted proteins, polysaccharides, and excess HAuCl4. A schematic for this method is shown in **Figure 26A**.

Method Two: Synthesis of AuNPs using adventitious root extract

Upon receipt, adventitious roots were homogenized in a minimal volume of water, creating a dense solution. This solution was centrifuged at 4,400 rpm for 5 min to remove large tissue debris from the homogenization. The resulting light brown supernatant was then transferred to dialysis tubing with a molecular weight cutoff value (MWCO) of 3.5 kDa, and dialyzed overnight against DI water. After dialysis, the solution outside of the dialysis tubing was collected and labeled as Solution I. The solution remaining in the tubing was then transferred to new tubing and dialyzed at 12 kDa. As indicated above, the solution outside of the tubing was collected and labeled Solution II, followed by a final dialysis through dialysis tubing with a cutoff value of 300 kDa. The final solution outside of the membrane was labeled as Solution III, and the solution remaining in the tubing was labeled Solution IV. Prior to analysis, the extracts were freeze dried and re-suspended in DI water. To synthesize gold nanoparticles from the ivy rootlet extract solutions, 500 µl of each solution (I-V) was transferred into a clean microfuge tube and aqueous HAuCl4 was added to a final concentration of 0.5 mM. The mixture was then vortexed, and reacted at room temperature. To concentrate the synthesized

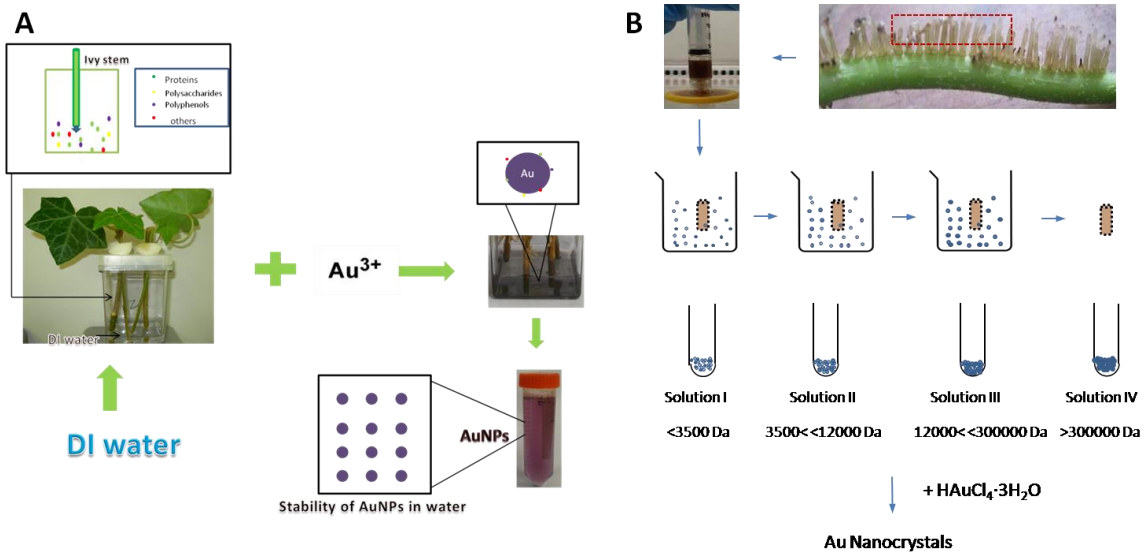

Figure 26 Schematic diagrams of two different methods used in this study.

A, Schematic of the sustainable biosynthesis and stability of AuNPs in ivy shoots culture system.HAuCl4 solution was added to the culture media and the gold nanoparticles could be collected after 24 hours. And then fresh HAuCl4 solution was added back for sustainable synthesis of AuNPs; B, Procedure for the ivy rootlet extracts preparation, separation and gold nanocrystal synthesis. Dialysis tubings with different molecular weight cutoff value (M.W.CO) of 3500 Da, 12,000 Da and 300,000 Da were used to separate different fractions from ivy rootlet extract. And then the four factions were used to synthesize gold nanoparticles.

gold nanoparticles, the solutions were centrifuged and washed as described above. A schematic for this method is shown in **Figure 26B.**

Characterization of the gold nanoparticles

A variety of techniques were used to determine if AuNPs were formed using the two methods described above. First, the Surface Plasmon Band (SPB), generated by the formation of AuNPs was examined using a Thermo Scientific Evolution 600 UV-Vis Spectrophotometer (Waltham, WA). After confirming the presence of SPB, the samples were analyzed by DLS and Zeta Potential analysis, using a Zetasizer Nano (Malvern Instruments Ltd, Worcestershine, UK), to determine the size distribution of the nanoparticles, and also the stability of the nanoparticles in solution. In order to characterize the morphology of the synthesized AuNPs, 10 µl of solution was air-dried onto a piece of silicon wafer and scanned at high resolution with a LEO 1525 FE-SEM equipped with a Gemini Emission Column. Simultaneously, energy dispersive x-ray spectroscopy (EDS) was conducted on the nanoparticle images to ensure that the nanoparticles were Au. The amount of protein present in the culture water was also characterized using a bicinchoninic acid (BCA) protein assay kit (Pierce) following the manufacturer's instructions. Similarly DMMB was used to measure the concentration of proteoglycan in solution using standard methodology [179].

To evaluate the intracellular uptake of the synthesized AuNPs, pelleted AuNPs were resuspended in PBS and added to cell culture medium. The AuNPs

containing media were then incubated with mouse MC3T3 cells for 4 hours. After incubation, cells were washed three times with PBS buffer and incubated in fresh α-MEM medium supplemented with 10% fetal bovine serum (FBS), 1.0 × 105 U/l penicillin (Sigma) and 100 mg/ml streptomycin (Sigma) overnight. The intracellular uptake of the AuNPs was observed using the Cytoviva™ system attached to a Nikon Eclipse E600.

Results

UV-Vis analysis of AuNP Formation (Method One)

After a few hours, the culture solution changed in color from clear to red, violet, dark purple, and light purple, depending on the concentration of HAuCl4 (insert in **Figure 27A**). At this point the solution was removed for analysis of the AuNPs formed during, and fresh HAuCl4 solution was added back to the GA7 boxes. Analysis of the UV-Vis spectra of the solution collected after incubation with HAuCl4 concentrations of 0.025, 0.05, 0.1, 0.2, 0.5 and 1 mM showed a SPB around 550 nm, specific for AuNPs [180]. No SPB was present at HAuCl4 concentrations of 0 and 5 mM (**Figure 27A**). While the SPB appeared at the same absorbance for AuNP forming concentrations, there was a significant difference in the width of the SPB at different concentrations of HAuCl4 solution.

To test the sustainability of the AuNP synthesis procedure described above, the HAuCl4 solution was removed and replaced with fresh solution every 24 hours and UV-Vis spectroscopy was conducted on the freshly removed solution to determine if AuNPs were still being produced. **Figure 27B** shows that at 0.1 mM HAuCl4, AuNPs were formed every 24 hours continuously over a 10 day period. Based on the Beer-Lambert law, the UV- Vis absorbance of a solution is directly proportional to the concentration of the absorbing species in the solution and the path length [181]. In our experiments, the path length was kept constant, thus the concentration of AuNPs in the solution, can be linearly correlated to the absorbance of the AuNP solution. We used this relationship to determine the relative concentration of AuNPs at each time interval, and to calculate the

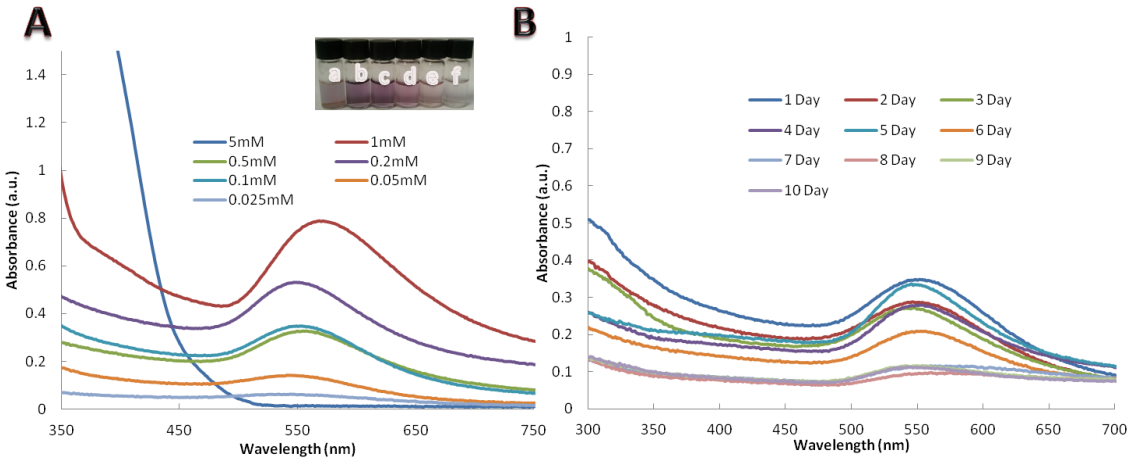

Figure 27 UV absorption spectra of gold nanoparticles synthesized.

A. UV-vis absorption spectra of gold nanoparticles synthesized in 0.025, 0.05, 0.1, 0.2, 0.5, 1 and 5mM aqueous AuCl4- in ivy culture system in the 1st day. The inset photo showed gold nanoparticles formed with different concentration of aqueous AuCl4- (a. 1 mM, b. 0.5 mM, c. 0.2 mM, d. 0.1 mM, e. 0.05 mM, f. 0.025 mM) in ivy culture system. B. UV-vis absorption spectra recorded the gold nanoparticles formation in live ivy culture system, rich with 0.1 mM aqueous $AuCl4^-$ environment from the 1st day to the 10th day respectively (Each curve experienced 24 hours reaction time).

efficiency of the synthesis procedure over time. From the spectral data, the efficiency of AuNP production remained high for the first 5 days, and decreased from day 6 -30. Despite the decrease in efficiency, AuNPs could still be obtained from the production system for greater than 30 days, demonstrating the sustainability of this method. The same sustainable property was also observed at lower HAuCl4 concentrations (0.025 mM, 0.05 mM) (**Figure 28A-B**). In the presence of higher concentrations of HAuCl4 solution (0.5 mM, 1 mM) the decrease in production efficiency was more obvious compared to the lower concentrations (**Figure 28C-D**), especially at 1 mM HAuCl4. At this high concentration of HAuCl4 some toxicity may occur in the ivy shoots, which decreases the rate of the overall production.

UV-Vis analysis of AuNP Formation (Method Two)

Solutions I-IV were reacted with 0.5 mM HAuCl4 solution at room temperature, as described in the Material and Methods section. A characteristic surface plasmon resonance band (SPR) for gold nanoparticles at 500-600 nm was detected in all four samples (I-IV) (**Figure 29**), confirming the synthesis of gold nanoparticles in these solutions.

Morphological analysis of AuNPs in Solution

DLS and Zeta potential analysis was used to analyze the size of the AuNPs in solution, and to determine the stability of nanoparticles. DLS of the AuNPs formed using Method One, indicated that the average size of the AuNPs increased from 10 to 300 nm with an increasing concentration of HAuCl4 from

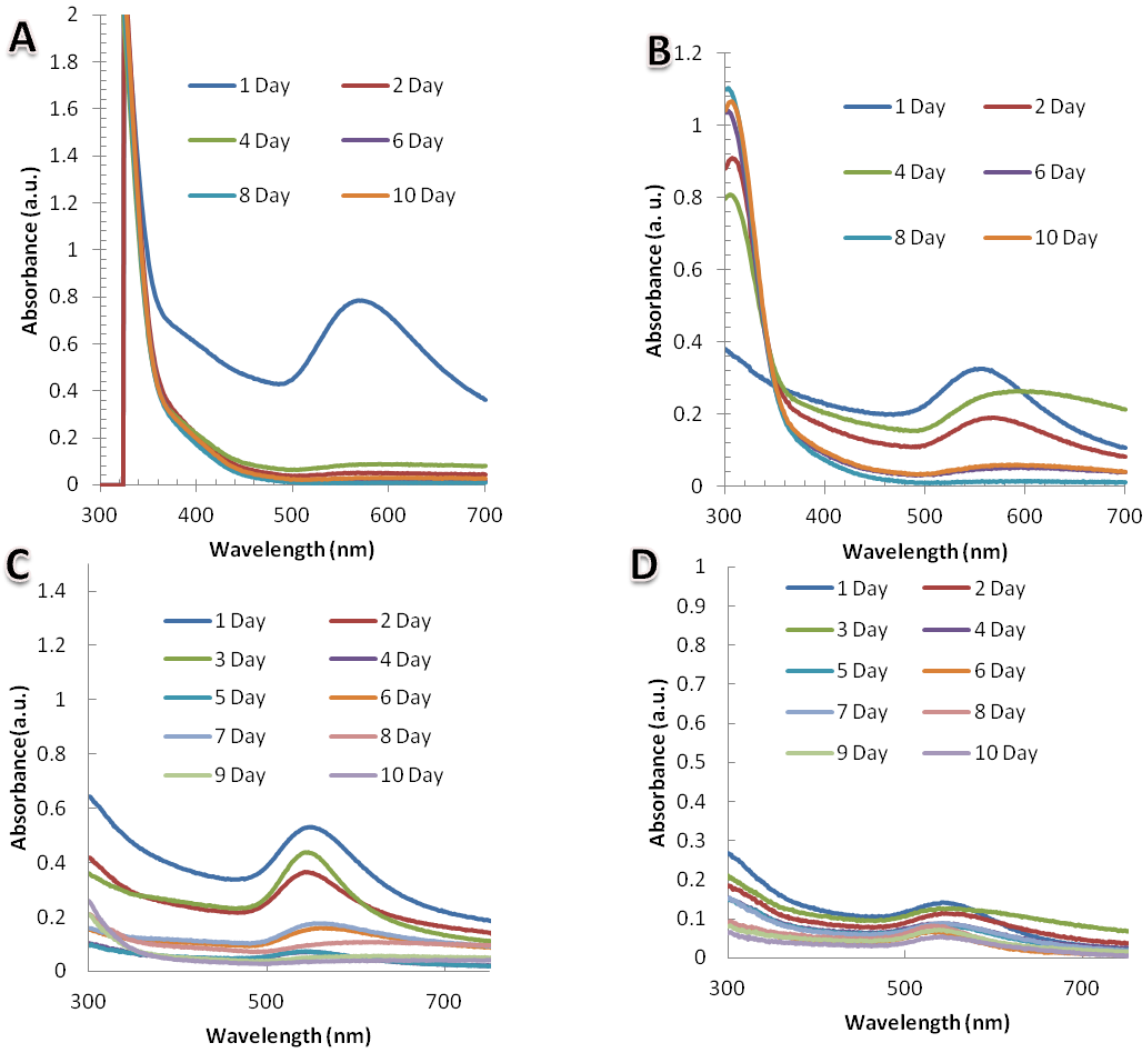

Figure 28 UV-Vis absorption spectra recorded the gold nanoparticles formation in live ivy culture system.

UV-Vis absorption spectra recorded the gold nanoparticles formation in live ivy culture system, rich with different concentration of aqueous AuCl4- environment (A, 1 mM; B, 0.5 mM; C, 0.05 mM; D, 0.025 mM) from the 1st day to the 10th day respectively.

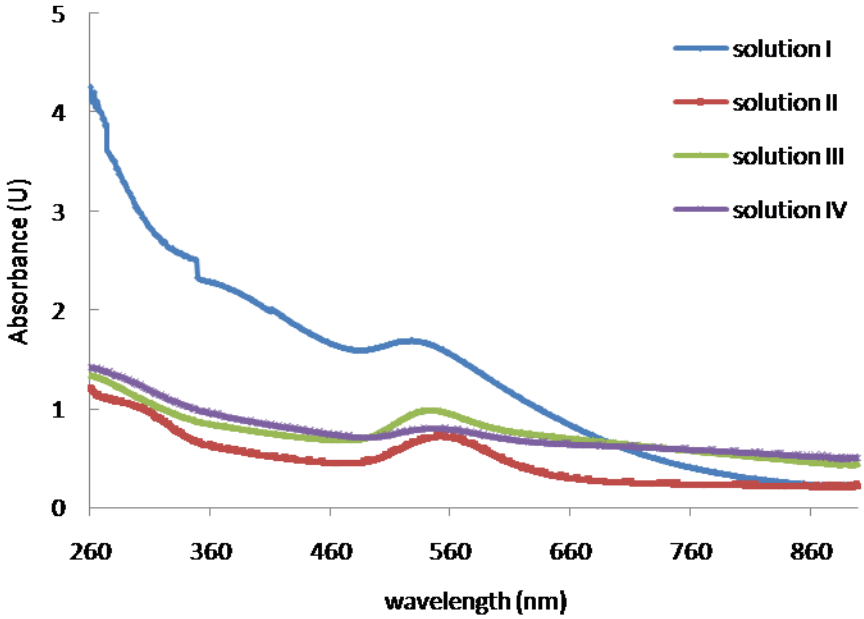

Figure 29 UV/Vis spectra of gold nanoparticles synthesized by different ivy rootlet extract solutions.

UV/Vis spectra of gold nanoparticles synthesized by different ivy rootlet extract solutions. Gold nanoparticles from solution I has a larger absorbance value at λmax, indicating more gold nanoparticles synthesized from solution I. Gold nanoparticles from solution III and IV have more absorbance over 720 nm, suggesting more nanoplates or clusteres in the solution III and IV.

0.025 to 2 mM. This agreed well with the red-shift of the UV-Vis spectra with higher concentrations, as shown in **Figure 27**. The size distribution of gold nanoparticles, formed from 0.1, 0.5 and 1 mM HAuCl4, were measured by DLS and displayed in **Figure 30A-C**. Based on the Zeta potential analysis, none of the solutions containing the AuNPs, formed using Method One, was stable in water, with zeta potentials ranging from -18.1 to -33.5 mV. This analysis was not surprising, since the AuNPs were observed to sediment from solution, and could easily be centrifuged at a low speeds.

The size distributions of AuNPs synthesized using Method Two, were also analyzed by DLS and Zeta potential analysis. AuNPs formed using Solution I and II showed smaller average sizes compared with solution III and IV (**Figure 30D-G**). A significant difference was observed in the Zeta potential of the AuNPs synthesized from the different solutions. Solution I, with a Zeta potential < -30 mV was moderately stable in solution. In solution II, the Zeta potential increased to > -30 mV, suggesting an instability of the AuNPs in solution. The Zeta potential further increased in solution III and IV to larger than -15 mV. Precipitates in these two solutions could be clearly observed, indicating the instability of the AuNPs and the aggregation of these AuNPs.

Morphological analysis of dry AuNPs

To examine the effect of the HAuCl4 concentration on the morphology of the nanoparticles produced, SEM was conducted. SEM images of the AuNPs synthesized using Method One revealed different sizes and shapes of gold

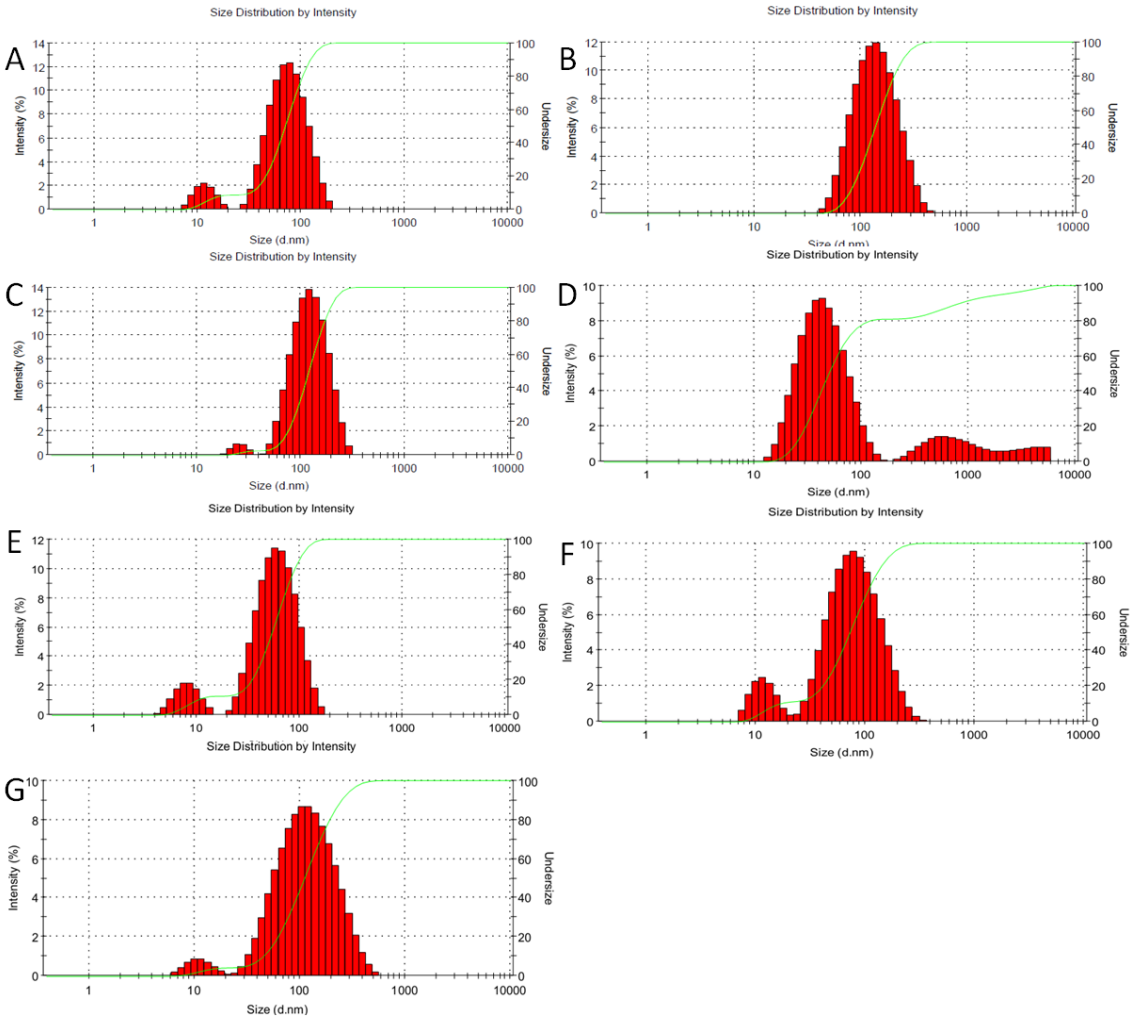

Figure 30 Size/ intensity histograms of gold nanostructures

Size/ intensity histograms of gold nanostructures synthesized from 0.1mM (A), 0.5Mm (B), 1mM (C) aqueous AuCl4- by live ivy shoots at room temperature. Size/ intensity histograms of gold nanoparticles synthesized by different ivy rootlet extract solutions I (D), II (E), III (F) and IV (G).

nanostructures produced by the varying HAuCl4 concentration (**Figure 31A-C**). Fig. 6A showed relatively uniform, spherical gold nanoparticles with sizes ranging from 10 to 100 nm, formed from 0.1 mM HAuCl4. The SEM images of gold nanoparticles synthesized using 0.5 mM HAuCl4 showed that most of the AuNPs had a spherical morphology, with a narrow size range of around 100 nm. At 1 mM HAuCl4, the AuNPs formed were heterogeneous with triangular, hexagonal, and spherical morphologies (**Figure 31C**). EDS was run simultaneously and determined that the nanoparticles were Au (**Figure 31D**).

Similar to the results obtained from the AuNPs synthesized using Method One, SEM images of AuNPs formed using Method Two revealed micro- or nano-crystals in all samples (**Figure 31E-H**). In solution I, spherical nanoparticles with a size range of 20-50 nm size were observed, with no other shapes of nanocrystals (**Figure 31E**). In solution II, nanoplates, nanorods, and spherical nanoparticles were observed (**Figure 31F**). In solution III, nanocrystals with sizes larger than 50 nm dominated, with triangular nanoplates also appearing (**Figure 31G**). Analysis of solution IV revealed the presence of predominately triangular nanoplates, with only a small number of spherical nanoparticles and nanocrystals with small diameters (**Figure 31H**).

Protein and polysaccharide concentration of the reaction solutions

Using a BCA kit, the concentration of protein present in the reaction solution for Method One was determined to be 1.45 µg/ml. However, the protein concentration of the adventitious root extract without dialysis in Method Two,

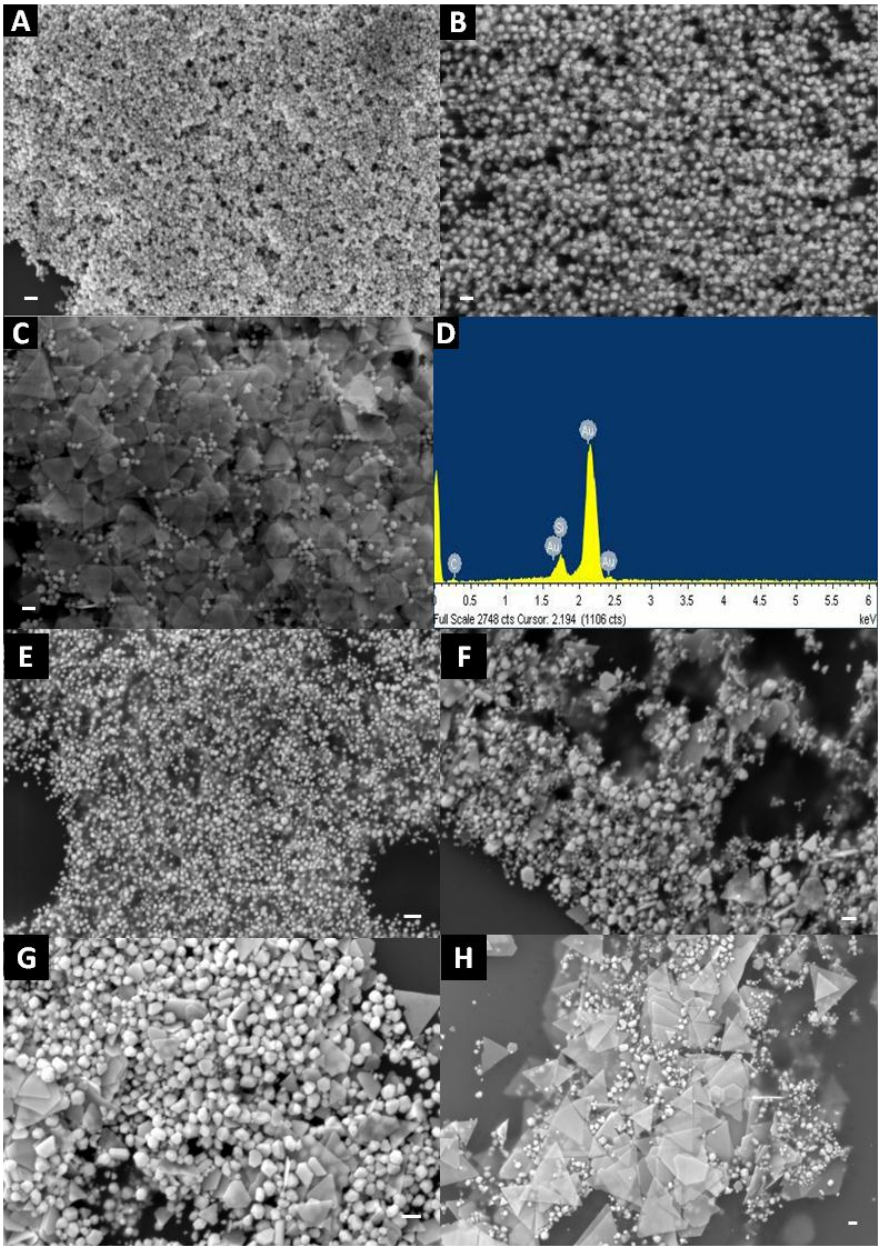

Figure 31 SEM images of gold nanostructure synthesized in 0.1mM, 0.5mM, 1mM aqueous AuCl4- by live ivy shoots at room temperature.

SEM images of gold nanostructure synthesized in 0.1mM (A), 0.5mM (B), 1mM (C) aqueous AuCl4- by live ivy shoots at room temperature, (D) EDX of the treated sample. SEM micrographs of gold nanoparticles synthesized by different ivy rootlet extract solutions I (E), II (F), III (G) and IV (H). (All scale bar= 100nm)

prior to reaction with HAuCl4, was found to be 1815.3 µg/ml. After reaction with HAuCl4, using Method Two, only 340.1 µg/ml remained in the supernatant, an 80% decrease compared to the starting concentration. Unlike the trend in protein concentration between the two methods, the DMMB assay determined that the concentration of proteoglycan in the reaction solution using Method One was 4.675 µg/ml, while the concentration for Method Two was 2.33 µg/ml.

Intracellular uptake of synthesized AuNPs

To test whether the AuNPs produced by both methods could be transported into cells for potential biomedical applications, a Cytoviva™ condenser mounted to a Nikon Eclipse microscope was used. Briefly, various AuNPs obtained from both methods were incubated with DMEM containing 10% serum for 24 hours, followed by centrifugation at 14,000 rpm and three washes of PBS. Microscopic analysis showed the internalization of the AuNPs into MC3T3 cells. Using the Cytoviva™ condenser, AuNPs were distinct from organelles due to their scattering properties, which make them appear scarlet or yellow in color (**Figure 32**). The control group without nanoparticles had no internal particulates, whereas the experimental samples displayed scarlet or yellow nanoparticles. This confirmed that the AuNPs synthesized in this study can be transported across the cell membrane, similar to AuNPs produced by other methods used for cancer therapy [182]. Previously, AuNPs have been proven to have great potential in drug delivery, cancer therapy and bio-imaging applications [183]. It is

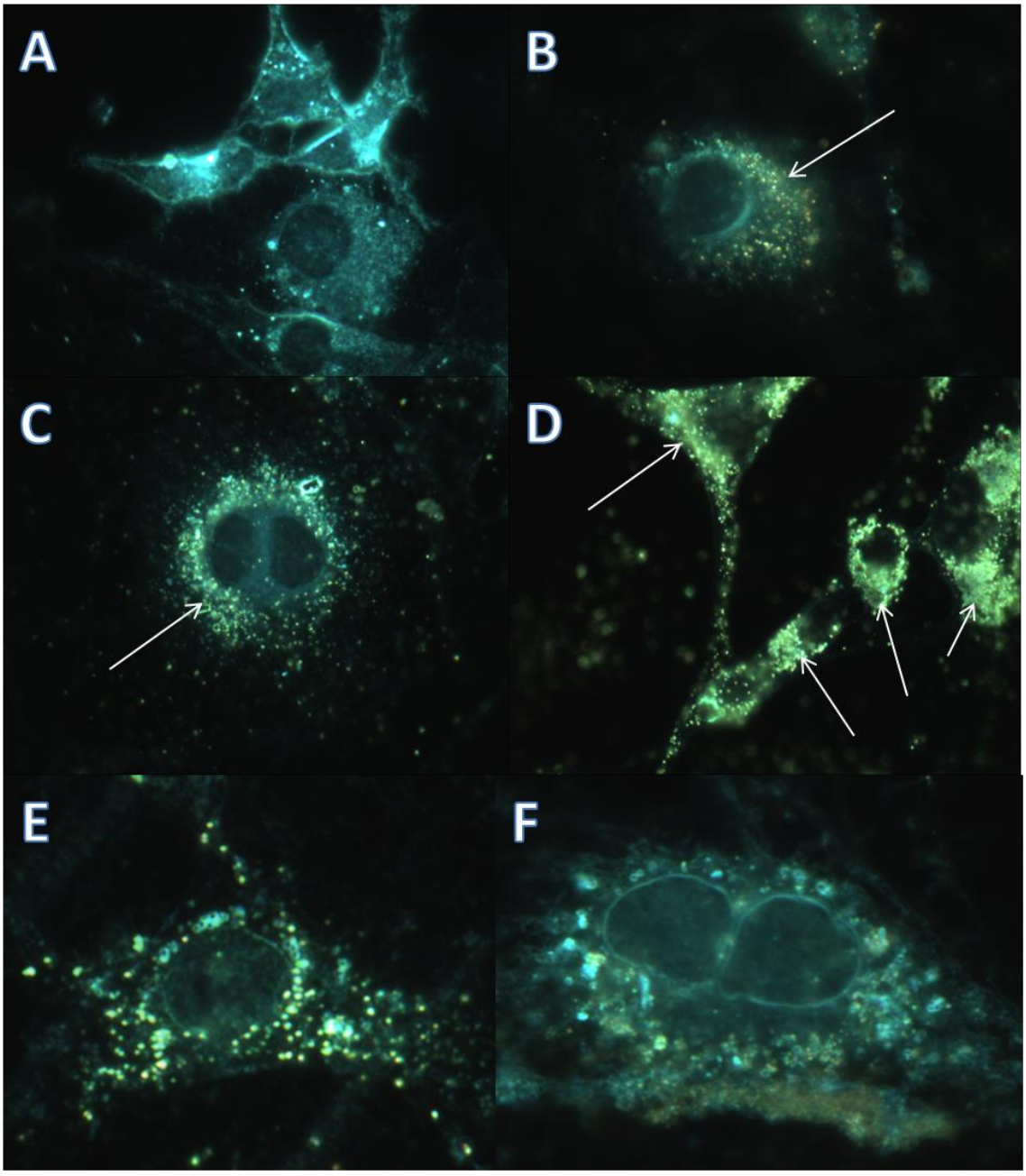

Figure 32 Dark-field microscopy images of Au NPs synthesized from HAuCl4

Dark-field microscopy images of Au NPs synthesized from 0.1 mM HAuCl4 (B), 0.5 mM HAuCl4 (C), 1 mM HAuCl4 (D) in MC3T3 cells respectively. (A) is the control group, without AuNPs. MC3T3 cell incubated with gold nanoparticles from solution II (E), and gold nanocrystals from solution III, IV (F).

conceivable that proteins, polysaccharides and other small molecules would provide a robust coating around gold nanoparticles to prevent aggregation. The dark field images demonstrated that our synthesized AuNPs using both methods could be easily taken up by the cells.

Discussion

Two methods for the synthesis gold nanoparticles using English ivy were developed. In Method One, a system was developed for the sustainable synthesis of AuNPs from the addition of aqueous HAuCl4 to actively growing English ivy shoots. The resulting AuNPs were collected from the culture medium every 24 hours, and fresh HAuCl4 solution was added to replenish the media. In Method Two, AuNPs were synthesized using four fractions of adventitious root extract separated by molecular weight using dialysis. When comparing the two methods at the same concentration of HAuCl4, 0.5 mM, both methods demonstrated the ability to form predominately spherical nanoparticles. However, the nanoparticles formed using Method Two, Solution I, showed a much smaller nanoparticle size compared to Method One at the same concentration. When Solutions II-IV were used, more diverse nanoparticle morphology was observed, with nanotriangles representing the dominant morphology. A similar trend was observed using Method One, where increasing concentrations of HAuCl4 led to the formation of nanotriangles, and fewer spherical nanoparticles. Considering that spherical nanoparticles are the most sought after morphology for biomedical applications, it would seem that the nanoparticles formed using Method One at a concentration of 0.5 mM HAuCl4, or Method Two using Solution I would be the best choices for green synthesis of spherical nanoparticles. In addition to the shape of synthesized AuNPs, the size of nanoparticles is also important in biomedical applications, and in general, the AuNPs formed from Method Two (**Figure 30 D-G**) were smaller than those formed from Method One (**Figure 30 A-**

C). While the size and shape of AuNPs necessary for a given application may dictate the choice of methods used for synthesis, other factors should be considered when comparing the two synthesis methods developed in this study. Using Method One, a significant amount of nanoparticles was synthesized over an extended period of time by simply replenishing HAuCl4 in the growth media of the ivy shoots. In this study, we were able to generate sustained nanoparticle production over a period of 30 days using the same shoots. Thus, Method One does not require a large input of raw plant materials, since a single batch of shoots can be sustained for over a month. This represents an economically favorable strategy, compared to strategies that require the destruction of the plant tissue for the formation of an extract, such as that described in Method Two. However, since the only control parameter that can be varied in Method One is the concentration of HAuCl4, it is expected that there would be less control over modifying this method for the generation of a particular AuNP size or morphology. In essence, the metabolic nature of the shoots will dictate the size and shape of the nanoparticles. Using Method Two, it is possible to more finely tune the synthesis of the AuNPs. For example, in Method Two, temperature, pH, extract concentration, and HAuCl4 concentration can be varied to more finely control the formation of specific AuNP sizes and morphology. In addition, while Method One represents a sustainable method, the AuNPs are collected every 24 hours, whereas in Method Two, the AuNPs can be collected in a matter of hours. The more rapid synthesis of AuNPs using Method Two may lead to the formation of a greater number of nanoparticles per unit time than Method One. As mentioned

earlier, since the extract formed using Method Two destroys the plant tissue in the formation of the extract, there would be an associated cost with this method over Method One. As such, the choice of green synthesis method depends on a variety of factors, with the ultimate choice being left to the user.

Another difference between the two methods is the potential biomolecules involved in the formation of the nanoparticles. The synthesis of gold nanoparticles in Method One could be achieved through two different routes. They can be synthesized directly in water, or can be formed in live shoots then released back to the water through the vascular system present in the stem. To investigate how these gold nanoparticles formed, 50 ml deionized water without HAuCl4 was placed into the GA7 box with live ivy shoots for 24 hours. The water was then removed from the box and mixed with different concentrations of HAuCl4 outside the culture system. It was observed that the AuNPs were slowly formed in solution, as evidenced by the gradual color change. The UV-Vis spectra were used to confirm the formation of gold nanoparticles (**Figure 33 A**). The broad SPB in the spectra resulted from the formation of large anisotropic particles. It was also observed from the SEM image of polydispersed AuNPs synthesized at 1 mM aqueous HAuCl4 solution (**Figure 33 B**). From these results, we hypothesized that biomolecules or small chemicals were continuously released into the culture water through ivy stems, which are responsible for reducing, stabilizing and shape-controlling agents for AuNPs synthesis.

In Method Two, the ivy rootlet extract was separated into four fractions using different MWCO dialysis bags. Most polyphenols are in the size range of 0.5-

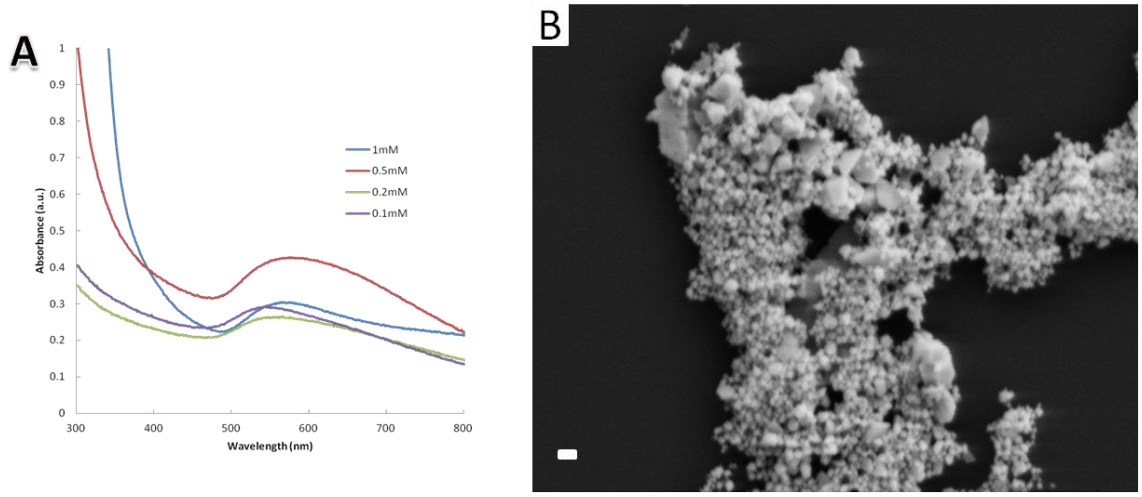

Figure 33 UV-Vis spectra of gold nanoparticles synthesized using different concentration of HAuCl4 solution

UV-Vis spectra of gold nanoparticles synthesized using different concentration of HAuCl4 solution (1mM, 0.5mM, 0.2mM, 0.1mM) with DI water derived from ivy culture system. B, SEM image of gold nanoparticles synthesized at 1mM HAuCl4 solution with DI water derived from ivy culture system. (the scale bar= 100nm)

4kD, and thus would be contained in solution I or II. Based on the size range, solution III was expected to contain the majority of biopolymers, such as polysaccharides and proteins, while solution IV may contain protein complexes and large macromolecules, such as glycoproteins or proteoglycans. The synthesis of gold nanoparticles by these four different solutions implied that molecules in different size ranges could individually and independently contribute to the synthesis of gold nanoparticles. To confirm the chemical components possibly involved in the synthesis process, the BCA protein assay, and proteoglycan assay were used to determine protein and proteoglycan concentrations. The results showed that both proteins and GAGs were available in the reaction solution of two methods. The concentration of proteins was much lower in Method One (1.45 µg/ml) than the extract solution without treatment in Method Two (1815.3 µg/ml), while the polysaccharide concentration in Method One (4.675 µg/ml) was twice that of Method Two (2.33 µg/ml). Considering that proteins secreted from the shoots of English ivy will be minimal, and that Solution I from Method Two, where most proteins will have been removed, generated the most uniform spherical nanoparticles, it is expected that other molecules are driving the formation of the AuNPs. Due to the comparably larger size of proteins, it is not surprising that the nanoparticles formed using Solutions II-IV of Method Two have increasingly larger size distributions, most likely due to the adsorption of proteins to the nanoparticle surfaces.

Conclusion

Two methods for the green synthesis of AuNPs using English ivy have been developed. Method One is a simple, sustainable synthesis system for AuNP production using actively growing English ivy shoots. This system allows continuous synthesis of gold nanoparticles in water with the addition of HAuCl4 solution. Compared to other plant-based synthesis methods for metal nanoparticles, the newly established system described in Method One does not require the preparation of plant extracts, or complicated isolation from live plants, thus representing a significant advancement in plant-based green manufacturing of metal nanoparticles. In Method Two, the facile synthesis of AuNPs from different molecular weight fractions of adventitious root extract was examined. Using different molecular weight ranges of the extract, AuNPs could be tuned to generate different shapes and sizes of AuNPs. The synthesized biocompatible AuNPs obtained from both methods could easily enter into MC3T3 cells, making them attractive candidates for bio-imaging, cancer therapy, and drug delivery.

CHAPTER V
ONE-STEP SYNTHESIS OF DENDRITIC GOLD NANOFLOWERS WITH HIGH SURFACE-ENHANCED RAMAN SCATTERING (SERS) PROPERTIES

Introduction

Gold nanostructures have drawn increasing interest due to their tunable morphology and promising optical as well as electronic properties for biomedical applications [45, 51, 184]. Especially in recent years, gold nanoparticles have demonstrated great potential in molecular imaging and sensing for disease diagnosis and therapy [185]. The majority of gold nanostructure research has focused on how the changes in size and shape of the nanostructures may influence their properties for applications in cancer therapy [186-188]. To enhance surface properties of gold nanostructures, efforts have been made into the development of nanostructures with unique morphology. Of particular interest is that gold nanopaticles have shown promise in bioimaging and biosensing [185]. Colloidal gold nanoparticles have been proposed as therapeutic nanocarriers for cancer treatment [186]. The most significant advance in increasing surface morphology of gold nanoparticles is the discovery of gold nanoflowers [189]. Gold nanoflowers are specialized gold nanoparticles with large amounts of highly branched tips that give the overall appearance of a flower. Nanomorphology of the highly branched surfaces with tips often leads to the formation of sharp peaks and valleys, which are potential “hot spots” for localized near-field enhancements [45, 50, 51]. The highly branching nanostructures can drastically increase the ratio of total surface to volume. These factors could potentially lead to the enhancement of the Raman scattering on the highly branched gold nanostructures [52, 53]. Therefore, compared with smooth surfaces, highly branched surfaces (such as dendrites, multi-pods, and nanoflowers) have a

greater potential for SERS based bioimaging and biosensing. For these reasons, studies have been conducted on the use of gold nanoflowers in bioimaging[45], biosensing[190], drug delivery and tissue engineering [191]. Despite the promise of gold nanoflowers, it remains a major challenge to repeatedly synthesize the unique nanostructures with low cost.

Currently, several synthetic methods have been proposed to synthesize branched metal nanostructures and gold nanoflowers [188, 192-194], including seed-mediated growth approaches, such as using CTAB, ascorbic acid [195], and one-pot methods using polyvinylpyrrolidone (PVP) [196], and tris base (TB)[197] . Some one-step synthesis approaches have been effective at producing thin gold nanoplates or multipods with a limited number of sharp tips, but have not been proven effective at the formation of highly branched gold nanoflowers [51, 189, 198, 199]. Seed-growth approach has been used to synthesize gold nanoflowers; however, concerns remain over repeatability of the method. For instance, size and shape of the gold nanoflowers synthesized by the two-step seed-mediated growth often depend on the facets of seed molecules, whose mechanism currently is not well understood [188, 193]. As such, it is difficult to control the formation of highly branched gold nanoflowers using most current methods. In addition, the multiple steps and the use of hazardous chemical reactants remains a major concern for biomedical applications [200]. Thus, the development of highly branched (more sharp tips) gold nanoparticles with biocompatible, low-cost, eco-friendly, and well-defined hierarchical structure is still a daunting challenge.

It is well-known that the oxidation of dopamine by AuCl4- could contribute to the formation of gold nanoparticles [201]. In this communication, a one-step approach for synthesizing gold nanoflowers (Au NFs) with multiple tips and dendritic structures is proposed by using dopamine. Briefly, Au NFs synthesized by combining HAuCl4 with *dopamine* hydrochloride in a rapid one-step reaction. The method uses dopamine, a natural neurotransmitter, as both the reducing and shape-directing agents, which is environmental friendly. Additionally, the Au NFs synthesized using this method have increased biocompatibility, due to the coating of the Au surface with an organic molecule that is normally present in mammalian cells. In order to further control the synthesis and morphology of the Au NFs, the effects of variations in reactant concentration, pH and temperature are discussed. Upon completion and tuning of the Au NF formation process, SERS activities and intracellular uptake of the Au NFs by human lung A549 cancer cells and mouse melanoma B16BL6 cells are present.

Results and Discussion

In the proposed experiment, Au NFs were synthesized by mixing 1mM HAuCl4 with 5mM *dopamine* hydrochloride with the original pH of 2.5 and vortexing for 1 min at room temperature. The color of the solution immediately changed from a light yellow to a dark orange, indicating the reduction of Au (III) to Au (0) [202]. The Au NFs were collected by centrifugation at 16,873 × g for 5 min followed by three washes using DI water. As shown in Figure 1, the synthesized flower-like particles exhibited multiple tips with dendritic structures. The Au NFs were dispersed with the average size in the range of 310-820 nm (**Figure 34 A**), and were comprised of numerous dendritic tips of 60-240 nm in length (**Figure 34 B**). The average hydrodynamic size of the nanoflowers in solution was approximately 630nm characterized by dynamic light scattering (DLS). The average zeta potential of the Au NFs was about -27.1 mV, indicating moderate stability of the Au NFs in solution. Furthermore, the crystal structure of the Au nanostructure was confirmed using X-ray diffraction (XRD). As shown in **Figure 35**, the XRD pattern of the Au NFs showed five peaks assigned to diffraction from the (111), (200), (220), (311), and (222) planes of face-centered-cubic (fcc) gold, which indicated the pure and well-crystallized gold [203].

The formation of the Au NFs over time was followed to determine how quickly they were formed, and the effect of increased reaction time on their formation. The reaction and evolution of the Au NFs were followed by time-dependent UV-vis spectroscopy and SEM. A decrease in intensity of the band at 390 nm, which is a characteristic band for dopamine-o-quinone,[204] indicated that the

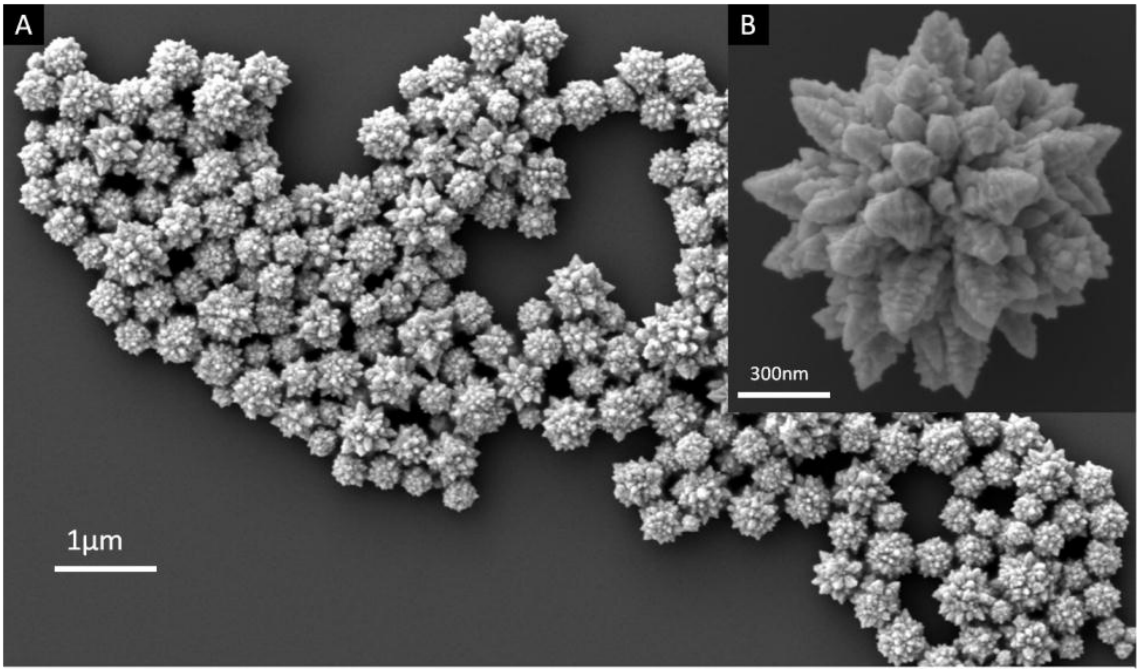

Figure 34 SEM images of the Au NFs obtained from an aqueous solution of HAuCl4 and dopamine

SEM images of the Au NFs obtained from an aqueous solution of $HAuCl_4$ (1mM) and dopamine (5mM). (A) The Au NFs had the average size ranging from 310-820 nm. Insert picture (B) is the enlarged image of the Au NFs, showing multiple tips with dendritic structures with the length of approximately 60-240 nm.

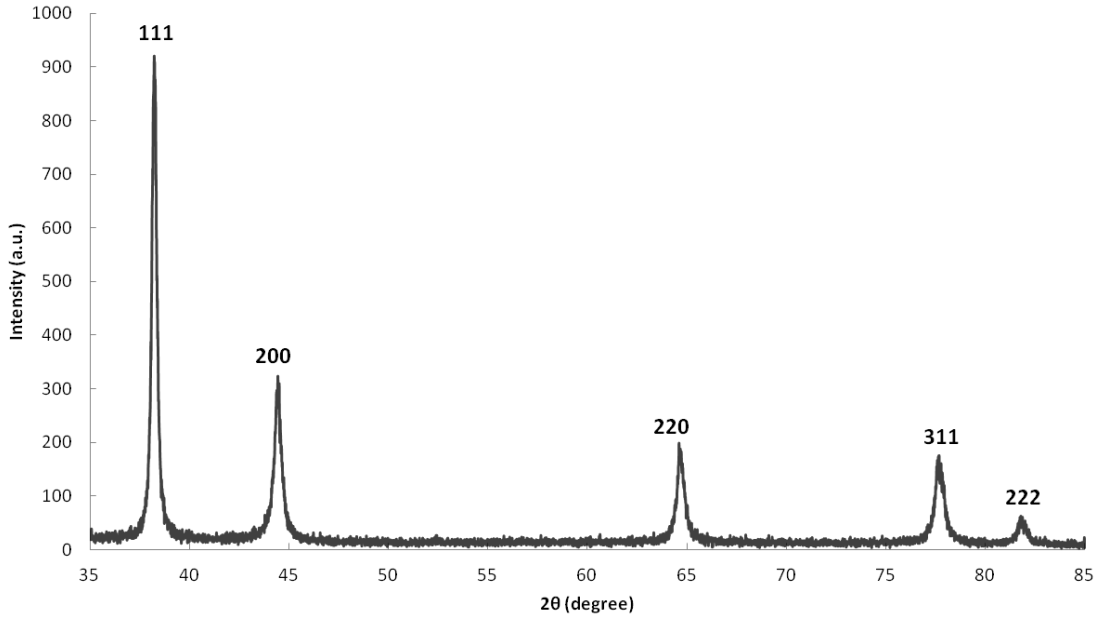

Figure 35 XRD pattern obtained from a thin film of Au NFs on a glass substrate.

The Au NF solution was on a glass substrate to obtain a smooth plane surface, and the diffraction pattern was recorded over a 2θ range of 35˚ - 85˚. The sharp reflections at 38.2˚, 44.3˚, 64.7˚, 77.6˚ and 81.8˚ correspondingly index as (111), (200), (220), (331) and (222), indicating characteristics of face-centered cubic (fcc) gold.

dopamine was reacting with the gold substrate (**Figure 36**). With the decrease of the dopamine-o-quinone peak, a shoulder began to form at ~510 nm, indicating the time dependent formation of the dendritic gold nanoparticles (**Figure 36**). Previous studies analyzing the UV-vis formation of dendritic gold nanostructures reported a similar trend, with the emergence of a broad peak from 500-600 nm, which was correlated with the gold nanostructures[205]. As shown in **Figure 37 A-D**, the possible development of reaction and the evolution of Au NFs were proposed as follows. First, the nanocrystals formed through the nucleation of gold, followed by equilibrium of gold nanocrystal growth, which is most likely via a Volmer-Weber mechanism [206]. Briefly, the stacked aggregations of small gold nanoparticles (roughly 10-50 nm) build up the tip of gold dendrites, and then $AuCl^{4-}$ ions and dopamine in solution are continuously captured by the tips via migration and diffusion [207]. The oriented attachment process could contribute to the formation of gold dendrites by the addition of new gold nanoparticles on the surface[207]. Then, several dendritic nanocrystals with different sizes were generated and their centers were randomly positioned in a spherical core. Finally, successive agglomerations of large amounts of dendritic tips around the core form flower-like nanostructures. Considering the possible growth processes of the Au NFs, we hypothesized that the concentration of the reactants ($HAuCl_4$ and dopamine) might affect the size and morphology of Au NFs. To validate this hypothesis, the concentration of dopamine was decreased from 5 mM to 1 or 0.5 mM, while keeping the concentration of gold precursor ($HAuCl_4$) constant as 1mM. As shown in **Figure 37 A-B**, irregular gold nanoparticles were formed with

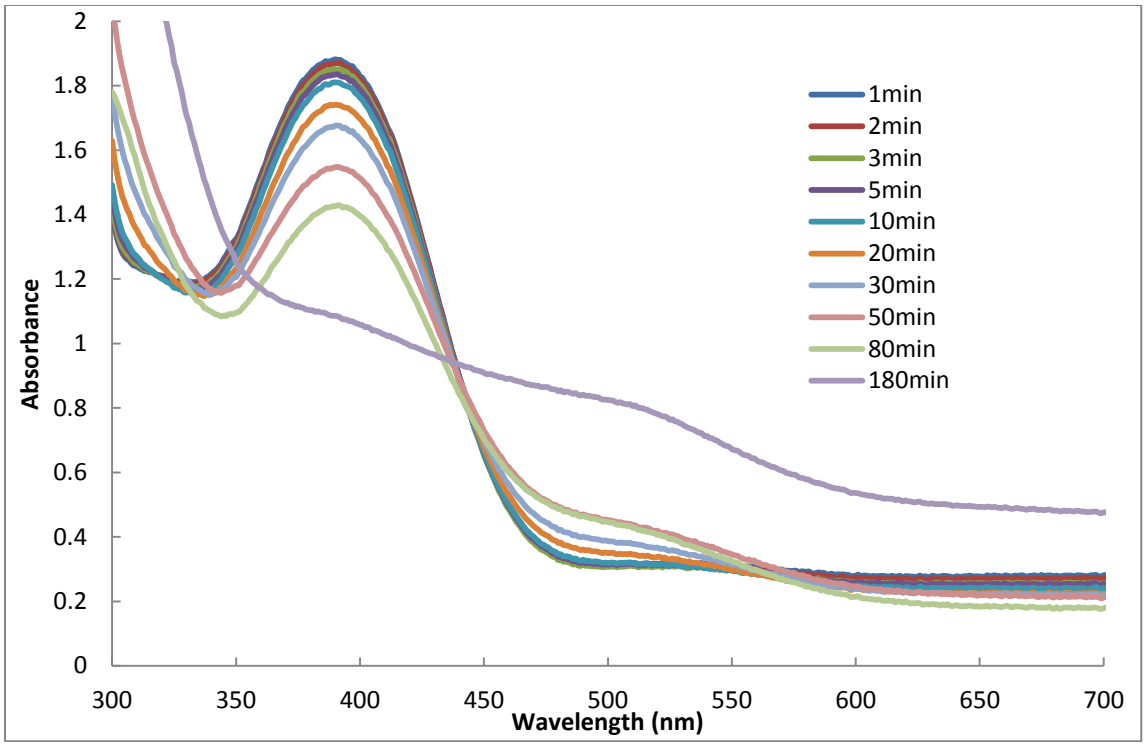

Figure 36 Time-dependent UV-vis spectra of reaction between HAuCl4 and dopamine. Time-dependent UV-vis spectra of reaction between HAuCl4 (1mM) and dopamine (5mM). The decreasing band at 390 nm is the characteristic band for dopamine-o-quinone. An increasing shoulder at ~510 nm indicates the formation of dendritic gold nanoflowers, similar to previous studies of dendritic gold nanostructures.

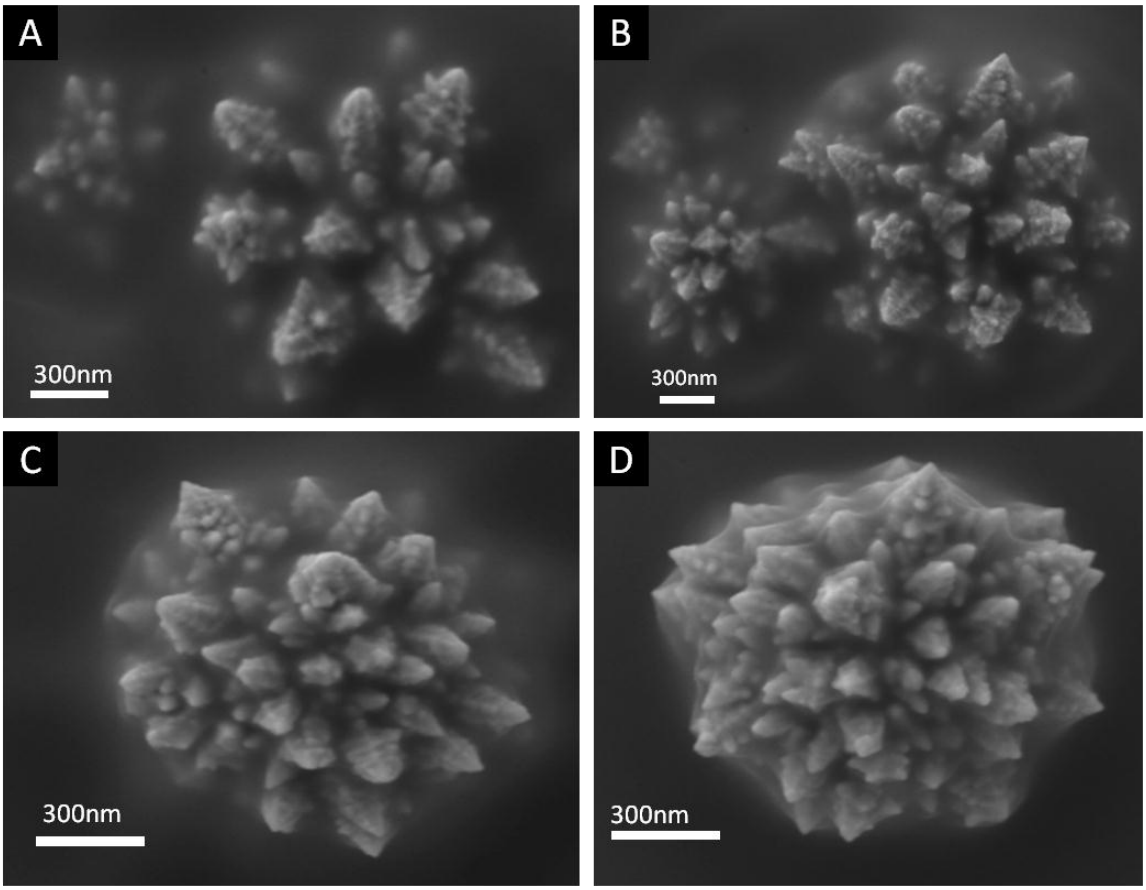

Figure 37 SEM images of the proposed mechanism for the formation of Au nanoflowers

SEM images of the proposed mechanism for the formation of Au nanoflowers (from A to D). First, several dendritic nanoparticles with different diameter were generated (A-B) and their centers were randomly positioned in a spherical space (C). After the generation of the primary structure, the inner core of the nanoflowers was formed by adding new dendritic nanoparticles around their center (D).

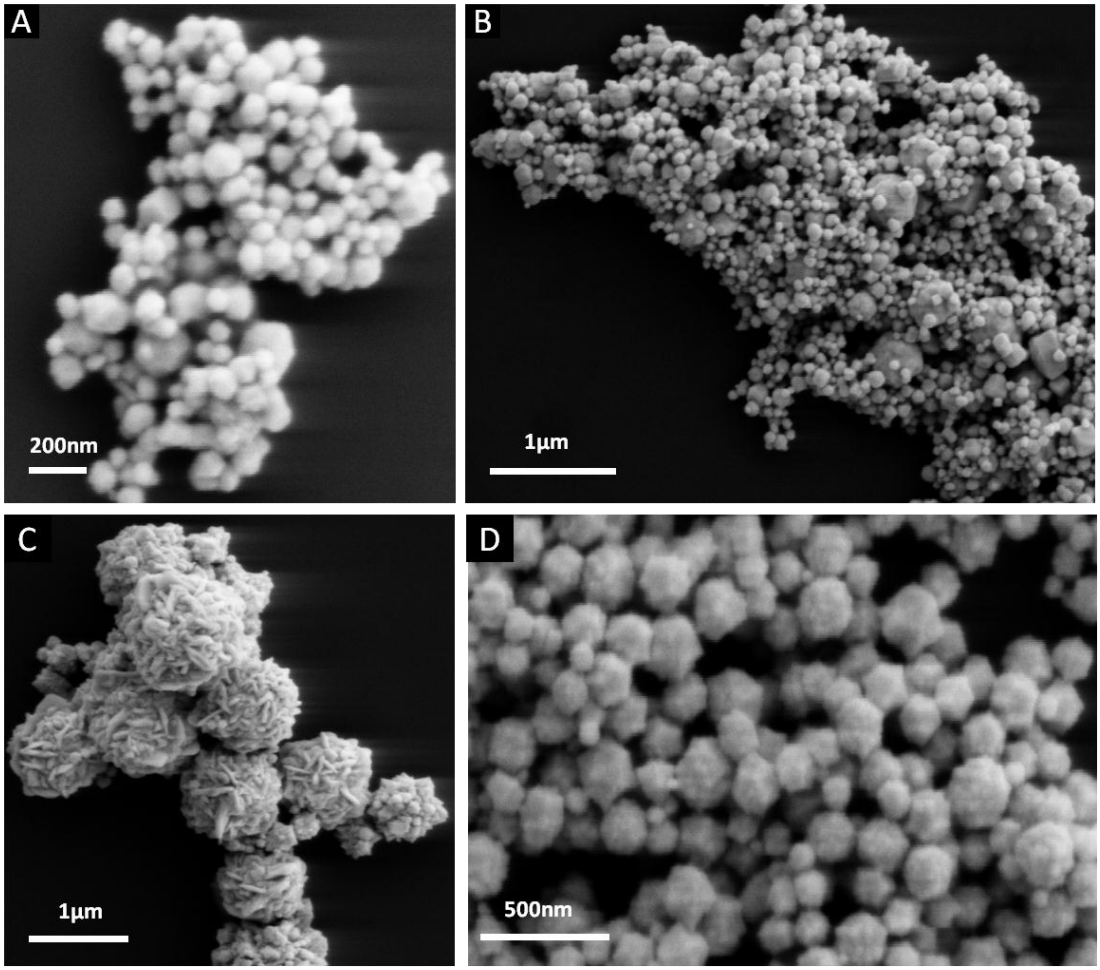

Figure 38 SEM images show the size and morphology of Au NFs affected by the concentration of the reactants (HAuCl4 and dopamine).

SEM images show the size and morphology of Au NFs affected by the concentration of the reactants ($HAuCl_4$ and dopamine). Au nanoparticles obtained from an aqueous solution of (A) $HAuCl_4$ (1mM) and dopamine (0.5mM), (B) $HAuCl_4$ (1mM) and dopamine (1mM). The images show irregular Au nanoparticles were formed with the size ranging from 50 to 300 nm. Au nanoparticles obtained from an aqueous solution of (C) $HAuCl_4$ (0.25mM) and dopamine (5mM), (D) $HAuCl_4$ (0.5mM) and dopamine (5mM). Random gold nanoparticles were observed, and few irregular flower-like nanostructures appeared with the aggregation of several small nanoparticles.

the size ranging from 50 to 300 nm. These gold nanoparticles were devoid of the sharp tips observed in the Au NFs. According to a previous study [201], gold nanoparticles also formed with the HAuCl4 concentration at 0.2 mM in the presence of lower concentrations of dopamine ranging from 2.5 µM to 0.02 mM. These findings indicate that low concentration of dopamine leads to the rough gold nanoparticles formation rather than flower-like gold nanostructures with sharp tips. However, when the dopamine concentration was increased to 5 mM, flower-like nanostructures were formed. Similar to the effect of changes in dopamine concentration, changes in the starting HAuCl4 concentration led to observable changes in size and morphology. When the HAuCl4 concentration was decreased from 1 mM to 0.5 mM and 0.25 mM, gold nanoparticles were formed along with irregular Au NFs (**Figure 38 C-D**). These Au NFs appeared with the aggregation of multiple smaller nanorods or spherical nanoparticles, while they were devoid of sharp tips and dendritic structures. In this study, dopamine likely acted as both the reducing and capping agents, attributing to the formation of Au NFs. To study the surface capping effect of dopamine, the Fourier transform infrared spectroscopy (FTIR) was used to characterize the pure dopamine and the synthesized Au NFs. As shown in **Figure 39**, some strong absorption features such as 1342 cm-1 (due to CH2 bending vibration), 1320 cm-1 (due to C-O-H asymmetry bending vibration), 1190 cm-1 (C-O symmetry vibration) in dopamine hydrochloride spectrum all disappeared in the Au NF spectrum [208]. The appearance of peaks at around 1455 and 1410 cm-1 in Au NF spectrum was due to the formation of the dopaminechrome [209]. The FTIR

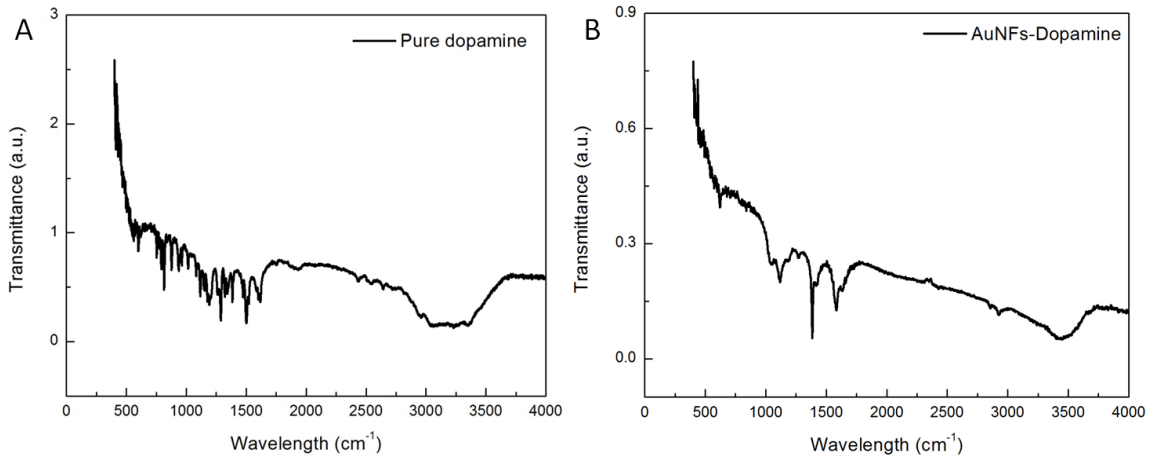

Figure 39 FTIR spectra of dopamine and synthesized Au NFs.

Some strong absorption features such as 1342 cm-1 (due to CH2 bending vibration), 1320 cm-1 (due to C-O-H asymmetry bending vibration), 1190 cm-1 (C-O symmetry vibration) in dopamine hydrochloride spectrum all disappeared in the Au NF spectrum. Instead, the appearance of peaks at around 1455 and 1410 cm-1 in Au NF spectrum was due to the formation of the dopaminechrome.

spectra provided evidence that the oxidation of dopamine might reduce Au ions to Au (0), and oxidative dopamine was absorbed on the Au NF surface.

Considering the effect of reactant concentration on Au NF synthesis, other reaction conditions, including pH, and temperature were also investigated. It was found that the tip length of the nanoflowers decreased with increasing pH values. 2N NaOH solution was used to regulate the pH value to be 3.5, 7.0, 8.5, and 9.0. When the pH increased to 3.5, smaller nanoflower-like gold nanoparticles with shorter tips in the length of around 20-80 nm were observed under SEM (**Figure 40 A**). As the pH value increased beyond 7.0, globular nano- and microparticles were formed as opposed to the flower like structures observed at pH 3.5 (**Figure 40 B**). We hypothesize that the reason for the above phenomenon is due to the increase of the oxidation rate of dopamine through increasing the pH values [201, 210], the chance for dopamine to cap and reduce the Au ions will be significantly reduced. Another parameter expected to alter the size and morphology of the Au NFs is the reaction temperature, since it affects nucleation, diffusion, and growth rates [211]. To determine the effect of reaction temperature, reactions of 1 mM HAuCl4 and 5 mM dopamine were maintained at different temperatures (20 °C; 40°C; 60 °C; 80 °C; 100 °C) with the pH value of 2.5. Interestingly, the reaction temperature did not affect the size and morphology of the Au NFs (**Figure 40 C-F**); however, with the increase of the reaction temperature, the color of the reacting solution was changed quickly, indicating the faster growth rate of the Au NFs.

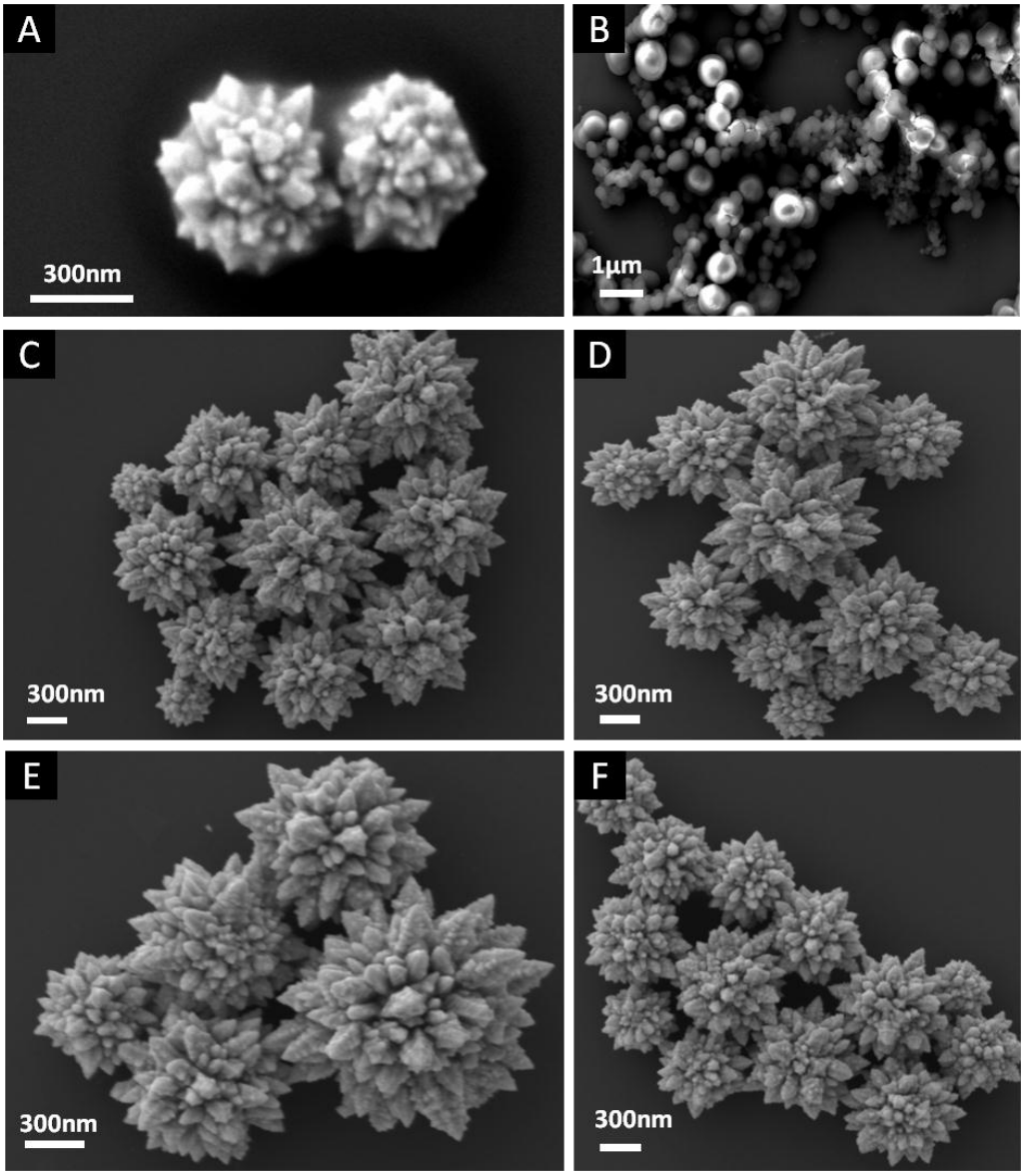

Figure 40 SEM images of Au NFs obtained from an aqueous solution of HAuCl4 and dopamine

SEM images of Au NFs obtained from an aqueous solution of HAuCl4 (1mM) and dopamine (5mM) at pH= 3.5 (A) and pH= 8.5 (B). And Au NFs obtained from an aqueous solution of HAuCl4 (1mM) and dopamine (5mM) with the original pH value of 2.5 at different temperature: 40˚C (C), 60˚C (D), 80˚C (E) and 100˚C (F). They showed at different reaction temperatures, the size and morphology of Au NFs did not have significant change.

Based on the above results, we may modify the Au NF structures through regulating concentration of the reactants, and the pH values.

SERS of gold nanoparticles and nanostructures has been regarded as a new optical spectroscopic analysis technique for sensitive detection of biomolecules in medicine [212, 213]. Since the weak spontaneous Raman scattering, colloidal gold nanoparticles has been well documented, where the increase in surface to volume ratio often leads to an enhanced SERS by 10^{14}-10^{15} folds [45]. To demonstrate the importance of the Au NFs synthesized in this study, we have analyzed the surface enhanced Raman scattering (SERS) of the Au NFs, and their potential for intracellular delivery. In previous work, the optimum size range of spherical gold nanoparticles for SERS was determined to be 20-70 nm [214]. Considering the small size of these gold nanoparticles, to further increase the SERS signals, it is necessary to alter the surface morphology to increase the surface to volume ratio. As such, studies have demonstrated that highly branched flower-like nanostructures can further enhance SERS by 10 times [45]. Furthermore, gold multipods with a limited number of tips (less than 10) or multiple tips without complex structures have been shown to create large electromagnetic field enhancements at the particle tips, with the efficiency of SERS effects related to the number of tips [45, 51, 188]. Based on this data, and the highly branching dendritic tips present on the Au NFs synthesized in this study, we hypothesize that this complex nanostructure may be used for SERS applications. To confirm this hypothesis, rhodamine 6G (Rh6G), a standard SERS probe molecule, was used to investigate the SERS capability of the Au

NFs. As a control, spherical gold nanoparticles (Au NPs) with a diameter from 10 to 100 nm were synthesized using a previously defined method [160]. Note that the control Au NPs are within the optimum size range for SERS applications. The typical SERS spectra of Au NFs and Au NPs with adsorbed Rh6G are presented in **Figure 41**. For the typical peaks (1315 cm-1, 1345 cm-1, 1450 cm-1, 1515 cm-1) in the Raman spectra, Au NFs showed much stronger enhancement of the SERS effect than gold nanoparticles. The significant enhancement might be due to the large amount of sharp tips on the surface of Au NFs that potentially act as "hot spots" [45]. Additionally, numerous tiny sharp tips or cavities on the dendritic structures may also act as "hot spots" [215], which attribute to achieve an double-enhanced SERS effect.

Due to the enhanced SERS of Au NFs, the combination of bio-imaging and delivery using the Au NFs were evaluated. Considering that biocompatibility is a major concern for biomedical applications, the cytotoxicity of the Au NFs was tested in A549 human lung tumor cells, and *B16BL6* mouse melanoma *cells. Both* cells were treated with Au NFs in different concentrations (0.128-400 μg/ml) for 48 h and then the cell viability was analyzed using the MTT assay. As shown in **Figure 42 A-B**, the cell viability in both cell lines was > 85% with the Au NF concentrations as high as 400 μg/ml. The low cytotoxicity of the Au NFs demonstrates a similar biocompatibility with gold nanoparticles often used in biomedical applications, thus validating the good biocompatibility of the Au NFs[216, 217]. Furthermore, the intracellular uptake of the nanoflowers in tumor cells was tested using dark field microscopy. As shown in **Figure 42 C-F**,

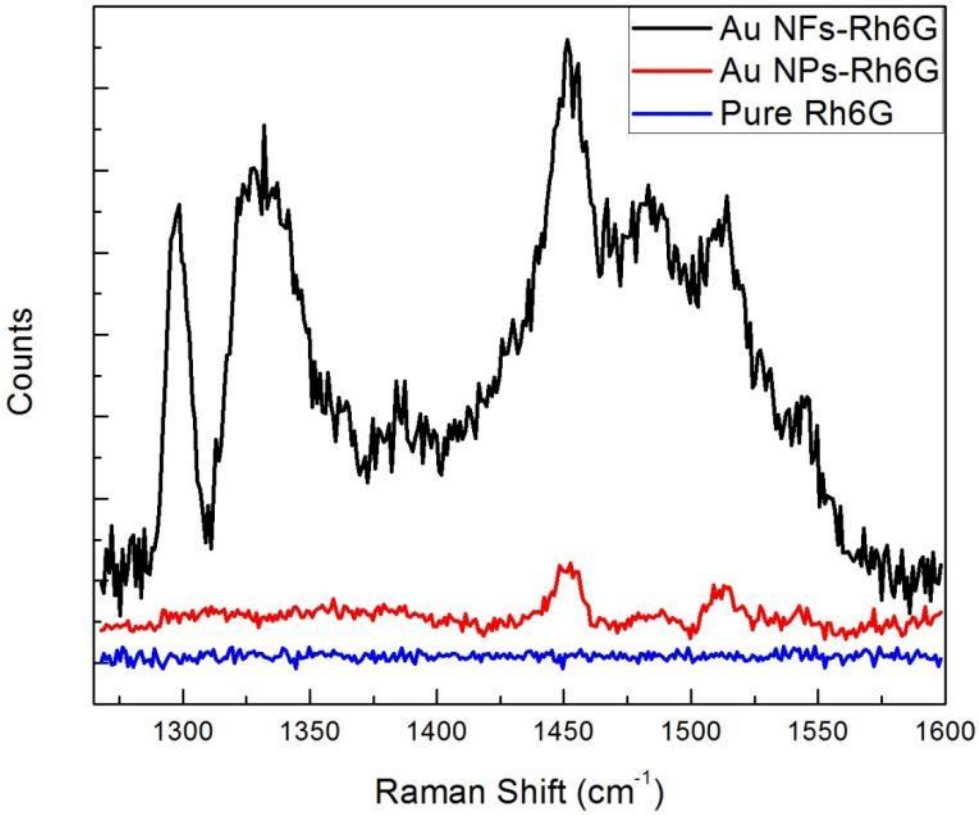

Figure 41 SERS spectra of Rh6G adsorbed on Au NFs and Au NPs, pure Rh6G as a control.

SERS spectra of Rh6G adsorbed on Au NFs (Black) and Au NPs (Red), pure Rh6G as a control (Blue). The concentrations of Rh6G in all samples were 5×10-5 M. The increased intensities of bands at 1315 cm-1, 1345 cm-1, 1450 cm-1, 1515 cm-1 on Au NFs compared with Au NPs indicated the Au NFs exhibited strong surface-enhanced Raman scattering effects.

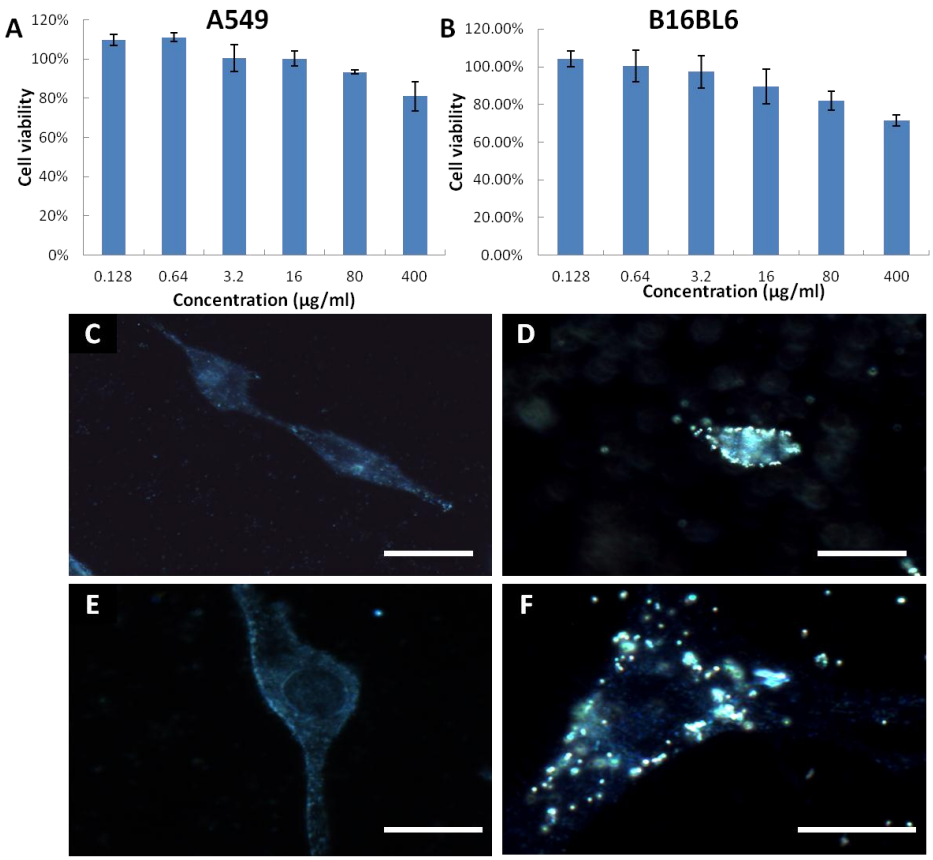

Figure 42 Survival histograms for A549 and B16BL6 cells exposed to AuNFs.

Survival histograms for A549 (A) and B16BL6 (B) cells exposed to Au NFs with various concentrations for 48 hours. Cell viability was measured by the MTT assay. Dark field images of A549 cells treated without nanoflower (C) and with Au NFs (D); B16BL6 cells treated without nanoflower (E) and with Au NFs (F). The Au NFs were incubated with cells for 4 hours at room temperature. The bright spots in B and D suggested the Au NFs were internalized in cancer cells. The scale bar indicates 10μm.

compared with the control group (without Au NF treatment) (**Figure 42 C, E**), more Au NFs entered into the cells (**Figure 42 D, F**). It is likely that the Au NFs is internalized by cancer cells through endocytosis, which is similar with other synthesized gold nanoparticles[218, 219]. These results suggest that the Au NFs could be proposed as active tags combined with specific biomolecules for *in vitro* detection.

Conclusion

In summary, a one-step approach for the synthesis of well-defined hierarchical Au NFs with low cost and eco-friendly has been developed. The highly branched Au NFs exhibited a strong SERS effect, due to the unique surface morphology with a large amount of sharp tips and dendritic structures. Furthermore, the Au NFs can be readily internalized by cancer cells along with promising biocompatibility. The above features make the Au NFs a unique candidate for bio-imaging, biosensors, and other biomedical applications.

CHAPTER VI
FUTURE PERSPECTIVES

Although nature based nanoparticles are generally biocompatible and less environmental toxicity associated with their production, there are still many aspects of their development that need to be improved. To be effective nanoparticles must maintain in vivo biostablity, circulate freely through the vascular systems of patients, and target specified cell types and organelles. Once they are produced, nature based nanoparticles must be modified and linked to small peptides, antibodies, or proteins to achieve particle stealthing, cellular targeting and organelle targeting.

Nanoparticle shields

When nanoparticles are administered systemically and circulate in the blood stream, sinusoids in the spleen filter the nanoparticles, and target them for removal via the reticuloendothelial system (RES) [220]. Nanoparticles bind to specific proteins of the RES cells [221]. Immunoglobulin and complement proteins are the major contributors to the recognition of the nanoparticles by the RES cells. The cells, which are macrophages will activate complement and induce hypersensitivity reactions [222]. The selective removal of the nanoparticles by the RES cells can be reduced by changing the characteristics of the nanoparticles' surface to render them more hydrophilic and neutralize the nanoparticle surface charge. The strategy covertly being investigated involve linkage of PEG to the surface of the nanoparticle to slow down the process of the RES cells binding to the nanoparticles [223]. Recently, Furumoto found that particles covalently bound with the albumin to their surface circulate longer

compared to the naked or PEGylated particles [224]. In another study by binding the nanoparticles to albumin, Furumoto was able to improve pharmacokinetic and pharmacodynamics properties of the doxorubicin-containing particles compared to PEGylated particles. Chemical modification of nature based nanoparticles with albumin to gain an extended circulation time and better stability.

Cellular targeting

Drug-carrying nanoparticles circulating in the blood stream need to be directed to specific target cells with minimal off-target effects. Many targeting mechanisms have been examined, utilizing both positive and negative targeting methods. Negative targeting, takes advantage of the fact that nature based nanoparticles accumulate in tumors due to enhanced permeability and retention effects, which is the result of the leaky, underdeveloped tumor vasculature that allows macromolecules to accumulate in the tumor [225]. Positive targeting of specific cells, involves the use of antibodies, aptamers, peptides and small molecules which bind to specific receptors. Most rapidly dividing cancer cells overexpress transferrin and folate receptors [226]. Unfortunately, these receptors are expressed to some degree on other non-target cells, resulting in off-target effects. The use of multi-specific antibodies to target the unique molecular marks on the cancer stem cells (CSCs), the source of the cancer, will alleviate the problems.

Cancer stem cells are a self-renewing population that express high ATP-binding cassette transporters (ABC transporters), which tend to export the chemotherapy agents, making the cells highly drug-resistant [227]. If CSCs leave their tissue barriers and circulate in the blood stream, they are able to metastasize and the cancer spreads. CSCs are characterized by their self-renewing ability and tumor regenerative ability. CSCs have distinct cell surface markers, which are different from the bulk of the tumor. In the breast cancer for example, breast cancer cells that express high levels of CD44 and low or undetectable levels of CD24 (CD44+/CD24-/low) are resistant to chemotherapy and have a significantly higher tumor generating ability compared to cells without these characteristics [228]. Therefore, by linking muti-specific antibodies, which are unique to certain CSCs, to nature based nanoparticles, an effective and highly selective method, can be developed for cancer treatment.

Organelle-specific targeting

Once the carrier nanoparticles enter a cell, the treatment efficiency is still heavily dependent on the ability of the carrier to deliver the drug to the site of action. If nanoparticle drug complex cannot successfully escape from the harsh endolysosome, it will be degraded. To enhance the endosomal escape, positively charged nanoparticles will be developed, which will mediate the rupture of the endosome following entry [229]. Subsequent to endosomal escape, the nanoparticles will be free to deliver DOX to nucleus generate DNA topoisomerase II mediated lesions in nuclear DNA, leading to apoptosis [230].

DOX has been used to treat many tumor types, but often its delivery has been problematic due to the drug-resistant cancer cells actively effluxing the drug out of their nuclear membranes [231]. Recently, a mitochondrially targeted version of mtDOX has been developed which has a peptide that targets mitochondria. It has been proven to be highly effective even in cell lines with an overexpressed efflux pump [232]. Nature based nanoparticle drug carriers; with a substitution of mtDOX in place of the original DOX therefore have the potential to provide a highly efficient drug delivery system targeting the drug-resist cancer cells.

In the development of nanoparticles that are site specific, efficient and of low toxicity, nanoparticle stealthing, cellular targeting, and organelle targeting must be considered. Nature based nanoparticles will be modified with albumin to reduce the RES effects, providing greater stability in the blood stream. Linkage of the nanoparticles to multi-specific antibodies will provide a means of targeting the CSCs to eliminate the source of the cancer. The DOX currently being used will be replaced by the mitochondrial targeting DOX to achieve better efficiency, especially in the drug-resist cancer cells. There is no single combination of nanoparticle modifications that will result in a perfect biomedical nanoparticle, but this is one more step in the right direction. It takes a lot of small steps to reach the final destination – the control and eradication of human disease.

LIST OF REFERENCES

[1] Kelkar SS, Reineke TM. Theranostics: Combining Imaging and Therapy. Bioconjug Chem. 2011;22:1879-903.
[2] Heath T, Fraley R, Papahdjopoulos D. Antibody targeting of liposomes: cell specificity obtained by conjugation of F(ab')2 to vesicle surface. Science. 1980;210:539-41.
[3] Farokhzad OC, Langer R. Impact of Nanotechnology on Drug Delivery. ACS Nano. 2009;3:16-20.
[4] Oh Y-K, Park TG. siRNA delivery systems for cancer treatment. Adv Drug Delivery Rev. 2009;61:850-62.
[5] Lee H, Park S, Kim JB, Kim J, Kim H. Entrapped doxorubicin nanoparticles for the treatment of metastatic anoikis-resistant cancer cells. Cancer Lett. 2013;332:110-9.
[6] Soppimath KS, Liu LH, Seow WY, Liu SQ, Powell R, Chan P, et al. Multifunctional Core/Shell Nanoparticles Self-Assembled from pH-Induced Thermosensitive Polymers for Targeted Intracellular Anticancer Drug Delivery. Adv Funct Mater. 2007;17:355-62.
[7] Giljohann DA, Seferos DS, Daniel WL, Massich MD, Patel PC, Mirkin CA. Gold Nanoparticles for Biology and Medicine. Angewandte Chemie International Edition. 2010;49:3280-94.
[8] Lytton-Jean AKR, Han MS, Mirkin CA. Microarray Detection of Duplex and Triplex DNA Binders with DNA-Modified Gold Nanoparticles. Anal Chem. 2007;79:6037-41.
[9] Kumar V, Yadav SK. Plant-mediated synthesis of silver and gold nanoparticles and their applications. Journal of Chemical Technology & Biotechnology. 2009;84:151-7.
[10] Mohanpuria P, Rana N, Yadav S. Biosynthesis of nanoparticles: technological concepts and future applications. J Nanopart Res. 2008;10:507-17.
[11] Shankar SS, Rai A, Ahmad A, Sastry M. Controlling the optical properties of lemongrass extract synthesized gold nanotriangles and potential application in infrared-absorbing optical coatings. Chem Mat. 2005;17:566-72.
[12] Chandran SP, Chaudhary M, Pasricha R, Ahmad A, Sastry M. Synthesis of gold nanotriangles and silver nanoparticles using Aloe vera plant extract. Biotechnology Progress. 2006;22:577-83.
[13] Shankar SS, Ahmad A, Pasricha R, Sastry M. Bioreduction of chloroaurate ions by geranium leaves and its endophytic fungus yields gold nanoparticles of different shapes. Journal of Materials Chemistry. 2003;13:1822-6.
[14] Ankamwar B, Chaudhary M, Sastry M. Gold nanotriangles biologically synthesized using tamarind leaf extract and potential application in vapor sensing. Synthesis and Reactivity in Inorganic Metal-Organic and Nano-Metal Chemistry. 2005;35:19-26.
[15] Yi S, Xia L, Lenaghan SC, Sun L, Huang Y, Burris JN, et al. Bio-Synthesis of Gold Nanoparticles Using English ivy (Hedera helix). Journal of Nanoscience and Nanotechnology. 2013;13:1649-59.

[16] Mukherjee P, Senapati S, Mandal D, Ahmad A, Khan MI, Kumar R, et al. Extracellular Synthesis of Gold Nanoparticles by the Fungus Fusarium oxysporum. ChemBioChem. 2002;3:461-3.
[17] He S, Guo Z, Zhang Y, Zhang S, Wang J, Gu N. Biosynthesis of gold nanoparticles using the bacteria Rhodopseudomonas capsulata. Materials Letters. 2007;61:3984-7.
[18] Ahmad A, Senapati S, Khan MI, Kumar R, Sastry M. Extra-/Intracellular Biosynthesis of Gold Nanoparticles by an Alkalotolerant Fungus, Trichothecium sp. J Biomed Nanotechnol. 2005;1:47-53.
[19] Strable E, Johnson JE, Finn MG. Natural Nanochemical Building Blocks: Icosahedral Virus Particles Organized by Attached Oligonucleotides. Nano Lett. 2004;4:1385-9.
[20] Zheng G, Chen J, Li H, Glickson JD. Rerouting lipoprotein nanoparticles to selected alternate receptors for the targeted delivery of cancer diagnostic and therapeutic agents. Proc Natl Acad Sci U S A. 2005;102:17757-62.
[21] Mulder WJM, Strijkers GJ, van Tilborg GAF, Cormode DP, Fayad ZA, Nicolay K. Nanoparticulate Assemblies of Amphiphiles and Diagnostically Active Materials for Multimodality Imaging. Accounts Chem Res. 2009;42:904-14.
[22] Zhang M, Liu M, Prest H, Fischer S. Nanoparticles Secreted from Ivy Rootlets for Surface Climbing. Nano Lett. 2008;8:1277-80.
[23] Xia L, Lenaghan S, Zhang M, Zhang Z, Li Q. Naturally occurring nanoparticles from English ivy: an alternative to metal-based nanoparticles for UV protection. Journal of Nanobiotechnology. 2010;8:12.
[24] Wang Y, Sun L, Yi S, Huang Y, Lenaghan SC, Zhang M. Naturally Occurring Nanoparticles from Arthrobotrys oligospora as a Potential Immunostimulatory and Antitumor Agent. Adv Funct Mater. 2012:DOI: 10.1002/adfm.201202619.
[25] Favi PM, Yi S, Lenaghan SC, Xia L, Zhang M. Inspiration from the natural world: from bio-adhesives to bio-inspired adhesives. J Adhes Sci Technol. 2012:1-30.
[26] Cormode DP, Jarzyna PA, Mulder WJM, Fayad ZA. Modified natural nanoparticles as contrast agents for medical imaging. Adv Drug Delivery Rev. 2010;62:329-38.
[27] Negishi H, Xu J-W, Ikeda K, Njelekela M, Nara Y, Yamori Y. Black and Green Tea Polyphenols Attenuate Blood Pressure Increases in Stroke-Prone Spontaneously Hypertensive Rats. J Nutr. 2004;134:38-42.
[28] Chen H, Zhang M, Qu Z, Xie B. Antioxidant activities of different fractions of polysaccharide conjugates from green tea (Camellia Sinensis). Food Chemistry. 2008;106:559-63.
[29] Fassina G, Buffa A, Benelli R, Varnier OE, Noonan DM, Albini A. Polyphenolic antioxidant (-)-epigallocatechin-3-gallate from green tea as a candidate anti-HIV agent. AIDS. 2002;16:939-41.
[30] Khan SG, Katiyar SK, Agarwal R, Mukhtar H. Enhancement of Antioxidant and Phase II Enzymes by Oral Feeding of Green Tea Polyphenols in Drinking Water to SKH-1 Hairless Mice: Possible Role in Cancer Chemoprevention. Cancer Res. 1992;52:4050-2.

[31] Chen C, Yu R, Owuor E, Tony Kong A. Activation of antioxidant-response element (ARE), mitogen-activated protein kinases (MAPKs) and caspases by major green tea polyphenol components during cell survival and death. Arch Pharm Res. 2000;23:605-12.
[32] Jankun J, Selman SH, Swiercz R, Skrzypczak-Jankun E. Why drinking green tea could prevent cancer. Nature. 1997;387:561-.
[33] Paschka AG, Butler R, Young CYF. Induction of apoptosis in prostate cancer cell lines by the green tea component, (−)-epigallocatechin-3-gallate. Cancer Lett. 1998;130:1-7.
[34] Wynder EL, Rose DP, Cohen LA. Nutrition and prostate cancer: A proposal for dietary intervention. Nutr Cancer. 1994;22:1-10.
[35] Pianetti S, Guo S, Kavanagh KT, Sonenshein GE. Green Tea Polyphenol Epigallocatechin-3 Gallate Inhibits Her-2/Neu Signaling, Proliferation, and Transformed Phenotype of Breast Cancer Cells. Cancer Res. 2002;62:652-5.
[36] Valcic S, Timmermann BN, Alberts DS, Wächter GA, Krutzsch M, Wymer J, et al. Inhibitory effect of six green tea catechins and caffeine on the growth of four selected human tumor cell lines. Anti-Cancer Drugs. 1996;7:461-8.
[37] Katiyar SK, Mukhtar H. Tea antioxidants in cancer chemoprevention. J Cell Biochem Suppl. 1997;27:59-67.
[38] Chung LY, Cheung TC, Kong SK, Fung KP, Choy YM, Chan ZY, et al. Induction of apoptosis by green tea catechins in human prostate cancer DU145 cells. Life Sci. 2001;68:1207-14.
[39] Thakur VS, Gupta K, Gupta S. Green tea polyphenols causes cell cycle arrest and apoptosis in prostate cancer cells by suppressing class I histone deacetylases. Carcinogenesis. 2012;33:377-84.
[40] Khan N, Mukhtar H. Multitargeted therapy of cancer by green tea polyphenols. Cancer Lett. 2008;269:269-80.
[41] Yang X, Zhao Y, Yang Y, Ruan Y. Isolation and Characterization of Immunostimulatory Polysaccharide from an Herb Tea, Gynostemma pentaphyllum Makino. J Agric Food Chem. 2008;56:6905-9.
[42] Chen H, Zhang M, Xie B. Quantification of Uronic Acids in Tea Polysaccharide Conjugates and Their Antioxidant Properties. J Agric Food Chem. 2004;52:3333-6.
[43] Gröning R, Breitkreutz J, Baroth V, Stephanie Müller R. Nanoparticles in plant extracts: influence of drugs on the formation of nanoparticles and precipitates in black tea infusions. Eur J Pharm Sci. 2002;15:149-55.
[44] Brigger I, Dubernet C, Couvreur P. Nanoparticles in cancer therapy and diagnosis. Adv Drug Delivery Rev. 2002;54:631-51.
[45] Xie J, Zhang Q, Lee JY, Wang DIC. The Synthesis of SERS-Active Gold Nanoflower Tags for In Vivo Applications. ACS Nano. 2008;2:2473-80.
[46] Liu X, Dai Q, Austin L, Coutts J, Knowles G, Zou J, et al. A One-Step Homogeneous Immunoassay for Cancer Biomarker Detection Using Gold Nanoparticle Probes Coupled with Dynamic Light Scattering. J Am Chem Soc. 2008;130:2780-2.

[47] Visaria RK, Griffin RJ, Williams BW, Ebbini ES, Paciotti GF, Song CW, et al. Enhancement of tumor thermal therapy using gold nanoparticle–assisted tumor necrosis factor-α delivery. Mol Cancer Ther. 2006;5:1014-20.
[48] Beattie IR, Haverkamp RG. Silver and gold nanoparticles in plants: sites for the reduction to metal. Metallomics. 2011;3:628-32.
[49] Sabo-Attwood T, Unrine JM, Stone JW, Murphy CJ, Ghoshroy S, Blom D, et al. Uptake, distribution and toxicity of gold nanoparticles in tobacco (Nicotiana xanthi) seedlings. Nanotoxicology.0:1-8.
[50] Wang H, Halas NJ. Mesoscopic Au “Meatball” Particles. Advanced Materials. 2008;20:820-5.
[51] Hao E, Bailey RC, Schatz GC, Hupp JT, Li S. Synthesis and Optical Properties of “Branched” Gold Nanocrystals. Nano Letters. 2004;4:327-30.
[52] Yuan H, Khoury CG, Hwang H, Wilson CM, Grant GA, Vo-Dinh T. Gold nanostars: surfactant-free synthesis, 3D modelling, and two-photon photoluminescence imaging. Nanotechnology. 2012;23:075102.
[53] Erathodiyil N, Ying JY. Functionalization of Inorganic Nanoparticles for Bioimaging Applications. Accounts Chem Res. 2011;44:925-35.
[54] Nie S, Xie M, Fu Z, Wan Y, Yan A. Study on the purification and chemical compositions of tea glycoprotein. Carbohydr Polym. 2008;71:626-33.
[55] Zuo Y, Chen H, Deng Y. Simultaneous determination of catechins, caffeine and gallic acids in green, Oolong, black and pu-erh teas using HPLC with a photodiode array detector. Talanta. 2002;57:307-16.
[56] Wang Y, Chen L, Ding Y, Yan W. Oxidized phospholipid based pH sensitive micelles for delivery of anthracyclines to resistant leukemia cells in vitro. International Journal of Pharmaceutics. 2012;422:409-17.
[57] Wang Y, Hao J, Li Y, Zhang Z, Sha X, Han L, et al. Poly(caprolactone)-modified Pluronic P105 micelles for reversal of paclitaxcel-resistance in SKOV-3 tumors. Biomaterials. 2012;33:4741-51.
[58] Carpenter JF, Randolph TW, Jiskoot W, Crommelin DJA, Middaugh CR, Winter G. Potential inaccurate quantitation and sizing of protein aggregates by size exclusion chromatography: Essential need to use orthogonal methods to assure the quality of therapeutic protein products. J Pharm Sci. 2010;99:2200-8.
[59] Roberts EAH. The phenolic substances of manufactured tea. X.—the creaming down of tea liquors. J Sci Food Agric. 1963;14:700-5.
[60] Horie H, Kohata K. Analysis of tea components by high-performance liquid chromatography and high-performance capillary electrophoresis. J Chromatogr A. 2000;881:425-38.
[61] Lv Y, Yang X, Zhao Y, Ruan Y, Yang Y, Wang Z. Separation and quantification of component monosaccharides of the tea polysaccharides from Gynostemma pentaphyllum by HPLC with indirect UV detection. Food Chem. 2009;112:742-6.
[62] Chen H, Wang Z, Qu Z, Fu L, Dong P, Zhang X. Physicochemical characterization and antioxidant activity of a polysaccharide isolated from oolong tea. Eur Food Res Technol. 2009;229:629-35.

[63] Schepetkin IA, Quinn MT. Botanical polysaccharides: Macrophage immunomodulation and therapeutic potential. Int Immunopharmacol. 2006;6:317-33.
[64] Paulsen BS. Plant Polysaccharides with Immunostimulatory Activities. Curr Org Chem. 2001;5:939-50.
[65] WangWang, Li, Zhao. Components and Activity of Polysaccharides from Coarse Tea. J Agric Food Chem. 2000;49:507-10.
[66] Lee J-H, Shim JS, Lee JS, Kim JK, Yang IS, Chung M-S, et al. Inhibition of Pathogenic Bacterial Adhesion by Acidic Polysaccharide from Green Tea (Camellia sinensis). J Agric Food Chem. 2006;54:8717-23.
[67] Eccles SA, Alexander P. Macrophage content of tumours in relation to metastatic spread and host immune reaction. Nature. 1974;250:667-9.
[68] Gordon S. Alternative activation of macrophages. Nat Rev Immunol. 2003;3:23-35.
[69] Schioppa T, Moore R, Thompson RG, Rosser EC, Kulbe H, Nedospasov S, et al. B regulatory cells and the tumor-promoting actions of TNF-α during squamous carcinogenesis. Proc Natl Acad Sci U S A. 2011;108:10662-7.
[70] van Horssen R, ten Hagen TLM, Eggermont AMM. TNF-α in Cancer Treatment: Molecular Insights, Antitumor Effects, and Clinical Utility. Oncologist. 2006;11:397-408.
[71] Lokshin A, Raskovalova T, Huang X, Zacharia LC, Jackson EK, Gorelik E. Adenosine-Mediated Inhibition of the Cytotoxic Activity and Cytokine Production by Activated Natural Killer Cells. Cancer Res. 2006;66:7758-65.
[72] Han EH, Choi JH, Hwang YP, Park HJ, Choi CY, Chung YC, et al. Immunostimulatory activity of aqueous extract isolated from Prunella vulgaris. Food Chem Toxicol. 2009;47:62-9.
[73] Oliveira Silva F, Neves Santos P, Melo C, Teixeira E, Sousa Cavada B, Pereira V, et al. Immunostimulatory activity of ConBr: a focus on splenocyte proliferation and proliferative cytokine secretion. Cell Tissue Res. 2011;346:237-44.
[74] Harada M, Qin Y, Takano H, Minamino T, Zou Y, Toko H, et al. G-CSF prevents cardiac remodeling after myocardial infarction by activating the Jak-Stat pathway in cardiomyocytes. Nat Med. 2005;11:305-11.
[75] Thomas J, Liu F, Link DC. Mechanisms of mobilization of hematopoietic progenitors with granulocyte colony-stimulating factor. Curr Opin Hematol. 2002;9:183-9.
[76] Metcalf D. The colony-stimulating factors and cancer. Nat Rev Cancer. 2010;10:425-34.
[77] Homey B, Müller A, Zlotnik A. Chemokines: agents for the immunotherapy of cancer? Nat Rev Immunol. 2002;2:175-84.
[78] Mulé JJ, Custer M, Averbook B, Yang JC, Weber JS, Goeddel DV, et al. RANTES secretion by gene-modified tumor cells results in loss of tumorigenicity in vivo: role of immune cell subpopulations. Hum Gene Ther. 1996;7:1545-53.

[79] BACON, B. K, PREMACK, A. B, GARDNER, P., et al. Activation of dual T cell signaling pathways by the chemokine RANTES. Washington, DC, ETATS-UNIS: American Association for the Advancement of Science; 1995.
[80] Keyser J, Schultz J, Ladell K, Elzaouk L, Heinzerling L, Pavlovic J, et al. IP-10-encoding plasmid DNA therapy exhibits anti-tumor and anti-metastatic efficiency. Exp Dermatol. 2004;13:380-90.
[81] Angiolillo AL, Sgadari C, Taub DD, Liao F, Farber JM, Maheshwari S, et al. Human interferon-inducible protein 10 is a potent inhibitor of angiogenesis in vivo. J Exp Med. 1995;182:155-62.
[82] Mantovani A, Gray PA, Van Damme J, Sozzani S. Macrophage-derived chemokine (MDC). J Leukoc Biol. 2000;68:400-4.
[83] Yang X, Kootala S, Hilborn J, Ossipov DA. Preparation of hyaluronic acid nanoparticles via hydrophobic association assisted chemical cross-linking-an orthogonal modular approach. Soft Matter. 2011;7:7517-25.
[84] Wang C, Cheng L, Liu Z. Drug delivery with upconversion nanoparticles for multi-functional targeted cancer cell imaging and therapy. Biomaterials. 2011;32:1110-20.
[85] Kim JO, Kabanov AV, Bronich TK. Polymer micelles with cross-linked polyanion core for delivery of a cationic drug doxorubicin. J Control Release. 2009;138:197-204.
[86] Ganta S, Devalapally H, Shahiwala A, Amiji M. A review of stimuli-responsive nanocarriers for drug and gene delivery. J Control Release. 2008;126:187-204.
[87] Singh R, Lillard Jr JW. Nanoparticle-based targeted drug delivery. Exp Mol Pathol. 2009;86:215-23.
[88] Meng H, Liong M, Xia T, Li Z, Ji Z, Zink JI, et al. Engineered Design of Mesoporous Silica Nanoparticles to Deliver Doxorubicin and P-Glycoprotein siRNA to Overcome Drug Resistance in a Cancer Cell Line. ACS Nano. 2010;4:4539-50.
[89] Tang Y, Lei T, Manchanda R, Nagesetti A, Fernandez-Fernandez A, Srinivasan S, et al. Simultaneous Delivery of Chemotherapeutic and Thermal-Optical Agents to Cancer Cells by a Polymeric (PLGA) Nanocarrier: An In Vitro Study. Pharm Res. 2010;27:2242-53.
[90] Wang Y, Mao F, Wei X. Characterization and antioxidant activities of polysaccharides from leaves, flowers and seeds of green tea. Carbohydr Polym. 2012;88:146-53.
[91] Zhang L, Liu W, Han B, Sun J, Wang D. Isolation and characterization of antitumor polysaccharides from the marine mollusk Ruditapes philippinarum. Eur Food Res Technol. 2008;227:103-10.
[92] http://www.who.int/mediacentre/factsheets/fs297/en/.
[93] Morgan G, Ward R, Barton M. The contribution of cytotoxic chemotherapy to 5-year survival in adult malignancies. Clin Oncol (R Coll Radiol). 2004;16:549-60.
[94] Nowak AK, Lake RA, Robinson BWS. Combined chemoimmunotherapy of solid tumours: Improving vaccines? Adv Drug Deliver Rev. 2006;58:975-90.

[95] Coley HM. Mechanisms and strategies to overcome chemotherapy resistance in metastatic breast cancer. Cancer Treat Rev. 2008;34:378-90.
[96] Holzel M, Bovier A, Tuting T. Plasticity of tumour and immune cells: a source of heterogeneity and a cause for therapy resistance? Nat Rev Cancer. 2013;13:365-U95.
[97] Nichols JW, Bae YH. Odyssey of a cancer nanoparticle: From injection site to site of action. Nano Today. 2012;7:606-18.
[98] Roy A, Chandra S, Mamilapally S, Upadhyay P, Bhaskar S. Anticancer and Immunostimulatory Activity by Conjugate of Paclitaxel and Non-toxic Derivative of LPS for Combined Chemo-immunotherapy. Pharm Res. 2012;29:2294-309.
[99] Steichen SD, Caldorera-Moore M, Peppas NA. A review of current nanoparticle and targeting moieties for the delivery of cancer therapeutics. Eur J Pharm Sci. 2013;48:416-27.
[100] Emens LA. Chemoimmunotherapy. Cancer J. 2010;16:295-303.
[101] Chen G, Emens LA. Chemoimmunotherapy: reengineering tumor immunity. Cancer Immunol Immun. 2013;62:203-16.
[102] Lee IH, An S, Yu MK, Kwon HK, Im SH, Jon S. Targeted chemoimmunotherapy using drug-loaded aptamer-dendrimer bioconjugates. J Control Release. 2011;155:435-41.
[103] Roy A, Singh MS, Upadhyay P, Bhaskar S. Combined Chemo-immunotherapy as a Prospective Strategy To Combat Cancer: A Nanoparticle Based Approach. Mol Pharm. 2010.
[104] Besch R, Poeck H, Hohenauer T, Senft D, Hacker G, Berking C, et al. Proapoptotic signaling induced by RIG-I and MDA-5 results in type I interferon-independent apoptosis in human melanoma cells. J Clin Invest. 2009;119:2399-411.
[105] Poeck H, Besch R, Maihoefer C, Renn M, Tormo D, Morskaya SS, et al. 5 '-triphosphate-siRNA: turning gene silencing and Rig-I activation against melanoma. Nat Med. 2008;14:1256-63.
[106] Karve S, Alaouie A, Zhou YP, Rotolo J, Sofou S. The use of pH-triggered leaky heterogeneities on rigid lipid bilayers to improve intracellular trafficking and therapeutic potential of targeted liposomal immunochemotherapy. Biomaterials. 2009;30:6055-64.
[107] Praetorius NP, Mandal TK. Engineered nanoparticles in cancer therapy. Recent Pat Drug Deliv Formul. 2007;1:37-51.
[108] Zitvogel L, Kroemer G. Anticancer immunochemotherapy using adjuvants with direct cytotoxic effects. J Clin Invest. 2009;119:2127-30.
[109] Xia LJ, Lenaghan SC, Zhang MJ, Wu Y, Zhao X, Burris JN, et al. Characterization of English ivy (Hedera helix) adhesion force and imaging using atomic force microscopy. J Nanopart Res. 2011;13:1029-37.
[110] Stevens MJ, Steren RE, Hlady V, Stewart RJ. Multiscale Structure of the Underwater Adhesive of Phragmatopoma Californica: a Nanostructured Latex with a Steep Microporosity Gradient. Langmuir. 2007;23:5045-9.

[111] Zhang M, Liu M, Bewick S, Suo Z. Nanoparticles to increase adhesive properties of biologically secreted materials for surface affixing. J Biomed Nanotechnol. 2009;5:294-9.
[112] Berglin M, Gatenholm P. The barnacle adhesive plaque: morphological and chemical differences as a response to substrate properties. Colloids and Surfaces B: Biointerfaces. 2003;28:107-17.
[113] Hennebert E, Viville P, Lazzaroni R, Flammang P. Micro- and nanostructure of the adhesive material secreted by the tube feet of the sea star Asterias rubens. Journal of Structural Biology. 2008;164:108-18.
[114] Wang YZ, Sun LM, Yi SJ, Huang YJ, Lenaghan SC, Zhang MJ. Naturally Occurring Nanoparticles from Arthrobotrys oligospora as a Potential Immunostimulatory and Antitumor Agent. Adv Funct Mater. 2013;23:2175-84.
[115] Yang Y, Yang E, An ZQ, Liu XZ. Evolution of nematode-trapping cells of predatory fungi of the Orbiliaceae based on evidence from rRNA-encoding DNA and multiprotein sequences. Proc Natl Acad Sci U S A. 2007;104:8379-84.
[116] Alexis F, Pridgen E, Molnar LK, Farokhzad OC. Factors Affecting the Clearance and Biodistribution of Polymeric Nanoparticles. Molecular Pharmaceutics. 2008;5:505-15.
[117] Williams A, Frasca V. Ion-Exchange Chromatography. Current Protocols in Molecular Biology: John Wiley & Sons, Inc.; 2001.
[118] Fedarko NS. Purification of proteoglycans from mineralized tissues. Methods Mol Biol. 2001;171:19-25.
[119] Tincer G, Yerlikaya S, Yagci FC, Kahraman T, Atanur OM, Erbatur O, et al. Immunostimulatory activity of polysaccharide-poly(I:C) nanoparticles. Biomaterials. 2011;32:4275-82.
[120] Liu JY, Huang W, Pang Y, Zhu XY, Zhou YF, Yan DY. The in vitro biocompatibility of self-assembled hyperbranched copolyphosphate nanocarriers. Biomaterials. 2010;31:5643-51.
[121] Pumphrey CY, Theus AM, Li S, Parrish RS, Sanderson RD. Neoglycans, Carbodiimide-modified Glycosaminoglycans: A New Class of Anticancer Agents That Inhibit Cancer Cell Proliferation and Induce Apoptosis. Cancer Res. 2002;62:3722-8.
[122] Yip GW, Smollich M, Gotte M. Therapeutic value of glycosaminoglycans in cancer. Mol Cancer Ther. 2006;5:2139-48.
[123] Roberts NJ, Zhou SB, Diaz LA, Holdhoff M. Systemic use of tumor necrosis factor alpha as an anticancer agent. Oncotarget. 2011;2:739-51.
[124] Calzascia T, Pellegrini M, Hall H, xE, kan, Sabbagh L, et al. TNF-α is critical for antitumor but not antiviral T cell immunity in mice. The Journal of Clinical Investigation. 2007;117:3833-45.
[125] Kang HS, Cho DH, Kim SS, Pyun KH, Choi I. Antitumor effects of IL-6 on murine liver tumor cells in vivo. J Biomed Sci. 1999;6:142-4.
[126] Mule JJ, Custer MC, Travis WD, Rosenberg SA. Cellular mechanisms of the antitumor activity of recombinant IL-6 in mice. J Immunol. 1992;148:2622-9.

[127] Ishiguro H, Kishimoto T, Furuya M, Nagai Y, Watanabe T, Ishikura H. Tumor-derived interleukin (IL)-6 induced anti-tumor effect in immune-compromised hosts. Cancer Immunol Immunother. 2005;54:1191-9.
[128] Voloshin T, Gingis-Velitski S, Bril R, Benayoun L, Munster M, Milsom C, et al. G-CSF supplementation with chemotherapy can promote revascularization and subsequent tumor regrowth: prevention by a CXCR4 antagonist. Blood. 2011;118:3426-35.
[129] Maeda M, Watanabe N, Tsuji N, Tsuji Y, Okamoto T, Sasaki H, et al. Enhanced antitumor effect of recombinant human tumor necrosis factor in combination with recombinant human granulocyte colony-stimulating factor in BALB/c mice. Jpn J Cancer Res. 1993;84:921-7.
[130] Veltri S, Smith JW, 2nd. Interleukin 1 Trials in Cancer Patients: A Review of the Toxicity, Antitumor and Hematopoietic Effects. Oncologist. 1996;1:190-200.
[131] Carmenate T, Pacios A, Enamorado M, Moreno E, Garcia-Martínez K, Fuente D, et al. Human IL-2 Mutein with Higher Antitumor Efficacy Than Wild Type IL-2. The Journal of Immunology. 2013;190:6230-8.
[132] Chou SH, Shetty AV, Geng YJ, Xu LP, Munirathinam G, Pipathsouk A, et al. Palmitate-derivatized human IL-2: a potential anticancer immunotherapeutic of low systemic toxicity. Cancer Immunol Immun. 2013;62:597-603.
[133] Tannenbaum CS, Hamilton TA. Immune-inflammatory mechanisms in IFNgamma-mediated anti-tumor activity. Semin Cancer Biol. 2000;10:113-23.
[134] Jarnicki AG, Lysaght J, Todryk S, Mills KHG. Suppression of antitumor immunity by IL-10 and TGF-beta-producing T cells infiltrating the growing tumor: Influence of tumor environment on the induction of CD4(+) and CD8(+) regulatory T cells. J Immunol. 2006;177:896-904.
[135] Wei C, Sirikanjanapong S, Lieberman S, Delacure M, Martiniuk F, Levis W, et al. Primary mucosal melanoma arising from the eustachian tube with CTLA-4, IL-17A, IL-17C, and IL-17E upregulation. Ent-Ear Nose Throat. 2013;92:36-40.
[136] Oshiro K, Kohama H, Umemura M, Uyttenhove C, Inagaki-Ohara K, Arakawa T, et al. Interleukin-17A is involved in enhancement of tumor progression in murine intestine. Immunobiology. 2012;217:54-60.
[137] Yu YZ, Luo XL, Liu SX, Xie Y, Cao XT. Intratumoral expression of MIP-1b induces antitumor responses in a pre-established tumor model through chemoattracting T cells and NK cells. Blood. 2004;104:402b-b.
[138] Wang LCS, Thomsen L, Sutherland R, Reddy CB, Tijono SM, Chen CJJ, et al. Neutrophil Influx and Chemokine Production during the Early Phases of the Antitumor Response to the Vascular Disrupting Agent DMXAA (ASA404). Neoplasia. 2009;11:793-803.
[139] Nakasone Y, Fujimoto M, Matsushita T, Hamaguchi Y, Huu DL, Yanaba M, et al. Host-derived MCP-1 and MIP-1alpha regulate protective anti-tumor immunity to localized and metastatic B16 melanoma. Am J Pathol. 2012;180:365-74.
[140] Lee JM, Merritt RE, Mahtabifard A, Yamada R, Kikuchi T, Crystal TG, et al. Intratumoral expression of macrophage-derived chemokine induces CD4(+) T cell-independent antitumor immunity in mice. J Immunother. 2003;26:117-29.

[141] Nakano A, Yoneyama H, Ueha S, Kitabatake M, Ishikawa S, Kawase I, et al. Intravenous administration of MIP-1α with intra-tumor injection of P. acnes shows potent anti-tumor effect. International Immunopharmacology. 2007;7:845-57.
[142] Inoue H, Iga M, Xin M, Asahi S, Nakamura T, Kurita R, et al. TARC and RANTES enhance antitumor immunity induced by the GM-CSF-transduced tumor vaccine in a mouse tumor model. Cancer Immunol Immun. 2008;57:1399-411.
[143] Ghia P, Transidico P, Veiga JP, Schaniel C, Sallusto F, Matsushima K, et al. Chemoattractants MDC and TARC are secreted by malignant B-cell precursors following CD40 ligation and support the migration of leukemia-specific T cells. Blood. 2001;98:533-40.
[144] Meenach SA, Anderson AA, Suthar M, Anderson KW, Hilt JZ. Biocompatibility analysis of magnetic hydrogel nanocomposites based on poly(N-isopropylacrylamide) and iron oxide. Journal of Biomedical Materials Research Part A. 2009;91A:903-9.
[145] Chuang JY, Tsai YY, Chen SC, Hsieh TJ, Chung JG. Induction of G0/G1 arrest and apoptosis by 3-hydroxycinnamic acid in human cervix epithelial carcinoma (HeLa) cells. In Vivo. 2005;19:683-8.
[146] Williams O. Flow cytometry-based methods for apoptosis detection in lymphoid cells. Methods Mol Biol. 2004;282:31-42.
[147] Wang Y, Ding Y, Liu Z, Liu X, Chen L, Yan W. Bioactive Lipids-Based pH Sensitive Micelles for Co-Delivery of Doxorubicin and Ceramide to Overcome Multidrug Resistance in Leukemia. Pharm Res. 2013;DOI 10.1007/s11095-013-1121-5.
[148] Wang Y, Yi S, Sun L, Huang Y, Lenaghan SC, Zhang M. Doxorubicin-loaded Cyclic Peptide Nanotube Bundles Overcome Multidrug Resistance in Breast Cancer Cells. Journal of Biomedical Nanotechnology. 2013;doi:10.1166/jbn.2013.1724.
[149] Chen D, Song P, Jiang F, Meng X, Sui W, Shu C, et al. pH-responsive mechanism of a deoxycholic acid and folate comodified chitosan micelle under cancerous environment. J Phys Chem B. 2013;117:1261-8.
[150] Iversen T-G, Skotland T, Sandvig K. Endocytosis and intracellular transport of nanoparticles: Present knowledge and need for future studies. Nano Today. 2011;6:176-85.
[151] Maier SA, Brongersma ML, Kik PG, Meltzer S, Requicha AAG, Koel BE, et al. Plasmonics - A Route to Nanoscale Optical Devices. Adv Mater. 2003;15:562-.
[152] Dick LA, McFarland AD, Haynes CL, Van Duyne RP. Metal film over nanosphere (MFON) electrodes for surface-enhanced Raman spectroscopy (SERS): Improvements in surface nanostructure stability and suppression of irreversible loss. J Phys Chem B. 2001;106:853-60.
[153] Qian X, Zhou X, Nie S. Surface-Enhanced Raman Nanoparticle Beacons Based on Bioconjugated Gold Nanocrystals and Long Range Plasmonic Coupling. J Am Chem Soc. 2008;130:14934-5.

[154] Mock J, Norton S, Chen SY, Lazarides A, Smith D. Electromagnetic Enhancement Effect Caused by Aggregation on SERS-Active Gold Nanoparticles. Plasmonics. 2011;6:113-24.
[155] El-Sayed IH, Huang X, El-Sayed MA. Surface Plasmon Resonance Scattering and Absorption of anti-EGFR Antibody Conjugated Gold Nanoparticles in Cancer Diagnostics: Applications in Oral Cancer. Nano Lett. 2005;5:829-34.
[156] Huang X, Jain PK, El-Sayed IH, El-Sayed MA. Gold nanoparticles: interesting optical properties and recent applications in cancer diagnostics and therapy. Nanomedicine. 2007;2:681-93.
[157] Lu W, Arumugam SR, Senapati D, Singh AK, Arbneshi T, Khan SA, et al. Multifunctional Oval-Shaped Gold-Nanoparticle-Based Selective Detection of Breast Cancer Cells Using Simple Colorimetric and Highly Sensitive Two-Photon Scattering Assay. ACS Nano. 2010;4:1739-49.
[158] Agasti SS, Chompoosor A, You C-C, Ghosh P, Kim CK, Rotello VM. Photoregulated release of caged anticancer dugs from gold nanoparticles. J Am Chem Soc. 2009;131:5728-9.
[159] Chen C, Daniel M-C, Quinkert ZT, De M, Stein B, Bowman VD, et al. Nanoparticle-Templated Assembly of Viral Protein Cages. Nano Lett. 2006;6:611-5.
[160] Xia L, Yi S, Lenaghan S, Zhang M. Facile synthesis of biocompatible gold nanoparticles with organosilicone-coated surface properties. J Nanopart Res. 2012;14:1-11.
[161] Liu GQ, Cai WP, Wang JJ, Duan GT. Electric Field Induced Au Nanoparticles with Controllable Morphology Under Surfactantless Condition. Nanosci Nanotechnol Lett. 2010;2:248-52.
[162] Chaughule RS, Ramanujan RV. Nanoparticles: Synthesis, Characterization and Applications. Los Angeles: American Scientific Publishers; 2011.
[163] Nalwa HS. Encyclopedia of Nanoscience and Nanotechnology. Los Angeles: American Scientific Publishers; 2004/2011.
[164] Ankamwar B, Chaudhary M, Sastry M. Gold nanotriangles biologically synthesized using Tamarind leaf extract and potential application in vapor sensing. Synth React Inorg M. 2005;35:19-26.
[165] Babu P, Sharma P, Kalita M, Bora U. Green synthesis of biocompatible gold nanoparticles using Fagopyrum esculentum leaf extract. Front Mater Sci. 2011;5:379-87.
[166] MubarakAli D, Thajuddin N, Jeganathan K, Gunasekaran M. Plant extract mediated synthesis of silver and gold nanoparticles and its antibacterial activity against clinically isolated pathogens. Colloids Surf B Biointerfaces. 2011;85:360-5.
[167] Sreelakshmi Ch, Datta KKR, Yadav JS, Reddy BVS. Honey Derivatized Au and Ag Nanoparticles and Evaluation of Its Antimicrobial Activity. Journal of Nanoscience and Nanotechnology. 2011;11:6995-7000.
[168] Mishra A, Tripathy SK, Yun S-I. Bio-Synthesis of Gold and Silver Nanoparticles from Candida guilliermondii and Their Antimicrobial Effect Against

Pathogenic Bacteria. Journal of Nanoscience and Nanotechnology. 2011;11:243-8.
[169] Panda T, Deepa K. Biosynthesis of Gold Nanoparticles. Journal of Nanoscience and Nanotechnology. 2011;11:10279-94.
[170] Sneha K, Sathishkumar M, Lee SY, Bae MA, Yun Y-S. Biosynthesis of Au Nanoparticles Using Cumin Seed Powder Extract. Journal of Nanoscience and Nanotechnology. 2011;11:1811-4.
[171] Nune SK, Chanda N, Shukla R, Katti K, Kulkarni RR, Thilakavathy S, et al. Green nanotechnology from tea: phytochemicals in tea as building blocks for production of biocompatible gold nanoparticles. J Mater Chem. 2009;19:2912-20.
[172] Chandran SP, Chaudhary M, Pasricha R, Ahmad A, Sastry M. Synthesis of Gold Nanotriangles and Silver Nanoparticles Using Aloevera Plant Extract. Biotechnol Prog. 2006;22:577-83.
[173] Ankamwar B, Damle C, Ahmad A, Sastry M. Biosynthesis of gold and silver nanoparticles using Emblica Officinalis fruit extract, their phase transfer and transmetallation in an organic solution. J Nanosci Nanotech. 2005;5:1665-71.
[174] Dubey SP, Lahtinen M, Sillanpää M. Tansy fruit mediated greener synthesis of silver and gold nanoparticles. Process Biochem. 2010;45:1065-71.
[175] Duran N, Marcato P, Alves O, De Souza G, Esposito E. Mechanistic aspects of biosynthesis of silver nanoparticles by several Fusarium oxysporum strains. J Nanobiotechnol. 2005;3:8.
[176] Shankar SS, Rai A, Ankamwar B, Singh A, Ahmad A, Sastry M. Biological synthesis of triangular gold nanoprisms. Nat Mater. 2004;3:482-8.
[177] Liu B, Xie J, Lee JY, Ting YP, Chen JP. Optimization of High-Yield Biological Synthesis of Single-Crystalline Gold Nanoplates. J Phys Chem B. 2005;109:15256-63.
[178] Song JY, Jang H-K, Kim BS. Biological synthesis of gold nanoparticles using Magnolia kobus and Diopyros kaki leaf extracts. Process Biochem. 2009;44:1133-8.
[179] French MM, Rose S, Canseco J, Athanasiou KA. Chondrogenic Differentiation of Adult Dermal Fibroblasts. Ann Biomed Eng. 2004;32:50-6.
[180] El-Brolossy TA, Abdallah T, Mohamed MB, Abdallah S, Easawi K, Negm S, et al. Shape and size dependence of the surface plasmon resonance of gold nanoparticles studied by Photoacoustic technique. Eur Phys J - Spec Top. 2008;153:361-4.
[181] Mitschele J. Beer-Lambert Law. J Chem Educ. 1996;73:A260.
[182] Huang X, El-Sayed IH, Qian W, El-Sayed MA. Cancer Cells Assemble and Align Gold Nanorods Conjugated to Antibodies to Produce Highly Enhanced, Sharp, and Polarized Surface Raman Spectra: A Potential Cancer Diagnostic Marker. Nano Lett. 2007;7:1591-7.
[183] Cheng Y, C. Samia A, Meyers JD, Panagopoulos I, Fei B, Burda C. Highly Efficient Drug Delivery with Gold Nanoparticle Vectors for in Vivo Photodynamic Therapy of Cancer. J Am Chem Soc. 2008;130:10643-7.
[184] Hao F, Nehl CL, Hafner JH, Nordlander P. Plasmon Resonances of a Gold Nanostar. Nano Letters. 2007;7:729-32.

[185] Jain PK, El-Sayed IH, El-Sayed MA. Au nanoparticles target cancer. Nano Today. 2007;2:18-29.
[186] Paciotti GF, Myer L, Weinreich D, Goia D, Pavel N, McLaughlin RE, et al. Colloidal Gold: A Novel Nanoparticle Vector for Tumor Directed Drug Delivery. Drug Delivery. 2004;11:169-83.
[187] Song Y, Steen WA, Peña D, Jiang Y-B, Medforth CJ, Huo Q, et al. Foamlike Nanostructures Created from Dendritic Platinum Sheets on Liposomes. Chemistry of Materials. 2006;18:2335-46.
[188] Nehl CL, Liao H, Hafner JH. Optical Properties of Star-Shaped Gold Nanoparticles. Nano Letters. 2006;6:683-8.
[189] Jena BK, Raj CR. Seedless, Surfactantless Room Temperature Synthesis of Single Crystalline Fluorescent Gold Nanoflowers with Pronounced SERS and Electrocatalytic Activity. Chem Mat. 2008;20:3546-8.
[190] Liu B, Tang D, Tang J, Su B, Li Q, Chen G. A graphene-based Au(111) platform for electrochemical biosensing based catalytic recycling of products on gold nanoflowers. Analyst. 2011;136:2218-20.
[191] Kumari S, Singh RP. Glycolic acid-g-chitosan-gold nanoflower nanocomposite scaffolds for drug delivery and tissue engineering. Int J Biol Macromol. 2012;50:878-83.
[192] Guerrero-Martínez A, Barbosa S, Pastoriza-Santos I, Liz-Marzán LM. Nanostars shine bright for you: Colloidal synthesis, properties and applications of branched metallic nanoparticles. Current Opinion in Colloid & Interface Science. 2011;16:118-27.
[193] Kuo C-H, Huang MH. Synthesis of Branched Gold Nanocrystals by a Seeding Growth Approach. Langmuir. 2005;21:2012-6.
[194] Xie J, Lee JY, Wang DIC. Seedless, Surfactantless, High-Yield Synthesis of Branched Gold Nanocrystals in HEPES Buffer Solution. Chemistry of Materials. 2007;19:2823-30.
[195] Jena BK, Raj CR. Synthesis of Flower-like Gold Nanoparticles and Their Electrocatalytic Activity Towards the Oxidation of Methanol and the Reduction of Oxygen. Langmuir. 2007;23:4064-70.
[196] Ren Y, Xu C, Wu M, Niu M, Fang Y. Controlled synthesis of gold nanoflowers assisted by poly(vinyl pyrrolidone)–sodium dodecyl sulfate aggregations. Colloids and Surfaces A: Physicochemical and Engineering Aspects. 2011;380:222-8.
[197] Luo Z, Fu T, Chen K, Han H, Zou M. Synthesis of multi-branched gold nanoparticles by reduction of tetrachloroauric acid with Tris base, and their application to SERS and cellular imaging. Microchim Acta. 2011;175:55-61.
[198] Chen S, Wang ZL, Ballato J, Foulger SH, Carroll DL. Monopod, Bipod, Tripod, and Tetrapod Gold Nanocrystals. Journal of the American Chemical Society. 2003;125:16186-7.
[199] Wang L, Liu C-H, Nemoto Y, Fukata N, Wu KCW, Yamauchi Y. Rapid synthesis of biocompatible gold nanoflowers with tailored surface textures with the assistance of amino acid molecules. RSC Advances. 2012;2:4608-11.

[200] Boca S, Rugina D, Pintea A, Barbu-Tudoran L, Astilean S. Flower-shaped gold nanoparticles: synthesis, characterization and their application as SERS-active tags inside living cells. Nanotechnology. 2011;22:055702.
[201] Baron R, Zayats M, Willner I. Dopamine-, l-DOPA-, Adrenaline-, and Noradrenaline-Induced Growth of Au Nanoparticles: Assays for the Detection of Neurotransmitters and of Tyrosinase Activity. Analytical Chemistry. 2005;77:1566-71.
[202] Dai X, Tan Y, Xu J. Formation of Gold Nanoparticles in the Presence of o-Anisidine and the Dependence of the Structure of Poly(o-anisidine) on Synthetic Conditions. Langmuir. 2002;18:9010-6.
[203] Leff DV, Brandt L, Heath JR. Synthesis and Characterization of Hydrophobic, Organically-Soluble Gold Nanocrystals Functionalized with Primary Amines. Langmuir. 1996;12:4723-30.
[204] Barreto WJ, Ponzoni S, Sassi P. A Raman and UV-Vis study of catecholamines oxidized with Mn(III). Spectrochimica Acta Part A: Molecular and Biomolecular Spectroscopy. 1998;55:65-72.
[205] Han X, Wang D, Huang J, Liu D, You T. Ultrafast growth of dendritic gold nanostructures and their applications in methanol electro-oxidation and surface-enhanced Raman scattering. Journal of Colloid and Interface Science. 2011;354:577-84.
[206] Aizawa M, Cooper AM, Malac M, Buriak JM. Silver Nano-Inukshuks on Germanium. Nano Lett. 2005;5:815-9.
[207] Fang J, Ma X, Cai H, Song X, Ding B. Nanoparticle-aggregated 3D monocrystalline gold dendritic nanostructures. Nanotechnology. 2006;17:5841.
[208] Yu F, Chen S, Chen Y, Li H, Yang L, Chen Y, et al. Experimental and theoretical analysis of polymerization reaction process on the polydopamine membranes and its corrosion protection properties for 304 Stainless Steel. Journal of Molecular Structure. 2010;982:152-61.
[209] Wang X, Jin B, Lin X. In-situ FTIR Spectroelectrochemical Study of Dopamine at a Glassy Carbon Electrode in a Neutral Solution. Analytical Sciences. 2002;18:931-3.
[210] Shen X-M, Dryhurst G. Oxidation Chemistry of (−)-Norepinephrine in the Presence of l-Cysteine. Journal of Medicinal Chemistry. 1996;39:2018-29.
[211] Jiang Y, Wu XJ, Li Q, Li J, Xu D. Facile synthesis of gold nanoflowers with high surface-enhanced Raman scattering activity. Nanotechnology. 2011;22:385601.
[212] Xu D, Gu J, Wang W, Yu X, Xi K, Jia X. Development of chitosan-coated gold nanoflowers as SERS-active probes. Nanotechnology. 2010;21:375101.
[213] Krpetić Ž, Guerrini L, Larmour IA, Reglinski J, Faulds K, Graham D. Importance of Nanoparticle Size in Colorimetric and SERS-Based Multimodal Trace Detection of Ni(II) Ions with Functional Gold Nanoparticles. Small. 2012;8:707-14.
[214] Jana NR, Pal T. Anisotropic Metal Nanoparticles for Use as Surface-Enhanced Raman Substrates. Advanced Materials. 2007;19:1761-5.

[215] Jasuja K, Berry V. Implantation and Growth of Dendritic Gold Nanostructures on Graphene Derivatives: Electrical Property Tailoring and Raman Enhancement. ACS Nano. 2009;3:2358-66.
[216] Connor EE, Mwamuka J, Gole A, Murphy CJ, Wyatt MD. Gold Nanoparticles Are Taken Up by Human Cells but Do Not Cause Acute Cytotoxicity. Small. 2005;1:325-7.
[217] Bhattacharya R, Mukherjee P, Xiong Z, Atala A, Soker S, Mukhopadhyay D. Gold Nanoparticles Inhibit VEGF165-Induced Proliferation of HUVEC Cells. Nano Lett. 2004;4:2479-81.
[218] Rodriguez-Lorenzo L, Krpetic Z, Barbosa S, Alvarez-Puebla RA, Liz-Marzan LM, Prior IA, et al. Intracellular mapping with SERS-encoded gold nanostars. Integr Biol. 2011;3:922-6.
[219] Oh E, Delehanty JB, Sapsford KE, Susumu K, Goswami R, Blanco-Canosa JB, et al. Cellular Uptake and Fate of PEGylated Gold Nanoparticles Is Dependent on Both Cell-Penetration Peptides and Particle Size. ACS Nano. 2011;5:6434-48.
[220] Moghimi SM, Hunter AC, Murray JC. Long-Circulating and Target-Specific Nanoparticles: Theory to Practice. Pharmacol Rev. 2001;53:283-318.
[221] Porter CJH, Moghimi SM, Illum L, Davis SS. The polyoxyethylene/polyoxypropylene block co-polymer Poloxamer-407 selectively redirects intravenously injected microspheres to sinusoidal endothelial cells of rabbit bone marrow. FEBS Lett. 1992;305:62-6.
[222] Moghimi SM, Hamad I, Andresen TL, Jørgensen K, Szebeni J. Methylation of the phosphate oxygen moiety of phospholipid-methoxy(polyethylene glycol) conjugate prevents PEGylated liposome-mediated complement activation and anaphylatoxin production. The FASEB Journal. 2006;20:2591-3.
[223] Otsuka H, Nagasaki Y, Kataoka K. PEGylated nanoparticles for biological and pharmaceutical applications. Adv Drug Delivery Rev. 2012;64, Supplement:246-55.
[224] Furumoto K, Yokoe J-I, Ogawara K-i, Amano S, Takaguchi M, Higaki K, et al. Effect of coupling of albumin onto surface of PEG liposome on its in vivo disposition. Int J Pharm. 2007;329:110-6.
[225] Maeda H, Greish K, Fang J. The EPR Effect and Polymeric Drugs: A Paradigm Shift for Cancer Chemotherapy in the 21st Century. In: Satchi-Fainaro R, Duncan R, editors. Polymer Therapeutics II: Springer Berlin Heidelberg; 2006. p. 103-21.
[226] Daniels TR, Delgado T, Rodriguez JA, Helguera G, Penichet ML. The transferrin receptor part I: Biology and targeting with cytotoxic antibodies for the treatment of cancer. Clin Immunol. 2006;121:144-58.
[227] Jordan CT, Guzman ML, Noble M. Cancer Stem Cells. New England Journal of Medicine. 2006;355:1253-61.
[228] Creighton CJ, Li X, Landis M, Dixon JM, Neumeister VM, Sjolund A, et al. Residual breast cancers after conventional therapy display mesenchymal as well as tumor-initiating features. Proceedings of the National Academy of Sciences. 2009;106:13820-5.

[229] Varkouhi AK, Scholte M, Storm G, Haisma HJ. Endosomal escape pathways for delivery of biologicals. J Control Release. 2011;151:220-8.
[230] Pommier Y, Leo E, Zhang H, Marchand C. DNA Topoisomerases and Their Poisoning by Anticancer and Antibacterial Drugs. Chem Biol. 2010;17:421-33.
[231] Szakacs G, Paterson JK, Ludwig JA, Booth-Genthe C, Gottesman MM. Targeting multidrug resistance in cancer. Nat Rev Drug Discov. 2006;5:219-34.
[232] Chamberlain GR, Tulumello DV, Kelley SO. Targeted Delivery of Doxorubicin to Mitochondria. ACS Chem Biol. 2013.

VITA

Sijia Yi comes from China. She received her bachelor's degree in Biomedical Engineering from Huazhong University of Science and Technology. In August of 2010, she entered University of Tennessee, Knoxville to pursue advanced degree in Biomedical Engineering. She received her Ph.D. degree in August of 2013.